

M⁴: Mathematical Models of Metastatic Malignancy

by

Adam Rhodes

A thesis submitted in partial fulfillment of the requirements for the degree of

Master of Science

in

Applied Mathematics

Department of Mathematical and Statistical Sciences

University of Alberta

© Adam Rhodes, 2018

Abstract

Metastasis — the spread of cancer from a primary to a distant secondary location — is implicated in over 90% of all cancer related deaths. Despite its importance in patient outcome, a full understanding of the metastatic process remains elusive, largely because of the difficulty in studying the phenomenon experimentally. In this thesis, we develop and analyze three models of metastatic cancer to shed light on the underlying mechanisms responsible for metastatic spread.

As metastasis is widely believed to be an inherently stochastic process, our first model is a spatially explicit stochastic model of cancer metastasis. The model includes the processes of primary tumor *release* of circulating tumor cells, *circulation* of these cells through the body, and metastatic *colonization* at a secondary site. We discover a *metastatic reproduction number*, R_0 , which characterizes the long-term behavior of the model, and provides an explicit condition for metastatic extinction. Parameterization of the model is done using data from experimental murine models of metastasis. Simulations of the parameterized model demonstrate the suitability of our modeling framework by accurately reproducing experimental observations.

Recent experimental observations have brought the prevailing view of metastasis as a passive sequence of random events into question, with several investigators suggesting that metastasis is an actively regulated process. In particular, immune involvement in the preparation of the *pre-metastatic niche* has inspired the *immune-mediated theory of metastasis*; a theory which posits

that the immune system — corrupted or ‘educated’ by the tumor to play pro-tumor roles — actively supports metastatic dissemination and growth.

To investigate the implications of the *immune-mediated theory of metastasis*, our second model is an ordinary differential equation model of tumor-immune dynamics at the sites of a primary and a metastatic tumor, incorporating both anti- and pro-tumor immune populations. Model simulations using literature-derived parameter estimates suggest that the *immune-mediated theory of metastasis* provides explanations for the poor performance of some immunotherapies, and for the observation of metastatic spread to sites of injury. Our results also suggest new potential avenues for therapy.

Our third model is a reduction of the second, focusing on the tumor-immune dynamics at the metastatic site. Analysis of the reduced model, using methods from geometric singular perturbation theory, provides a mathematical description of metastatic phenomena such as dormancy and blow-up. A parameter sensitivity analysis is performed, and the parameterized model is used to simulate the effects of therapeutic interventions. Necessary conditions for metastatic blow-up after primary tumor resection provide hypotheses concerning the biology of metastasis.

The tumor-immune models investigated in this thesis, both based on the *immune-mediated theory of metastasis*, provide an explanation for many experimentally and clinically observed metastatic phenomena — including dormancy, blow-up, recurrence, and metastasis to sites of injury — under a single modelling framework; something that previous models of metastasis have been unable to do. Overall, the results of this thesis provide novel insights into the metastatic process and introduce new biological questions for future research.

Preface

The material of Chapter 2 is included in a submitted manuscript:

C. Frei, T. Hillen, and A. Rhodes. A Stochastic Model for Cancer Metastasis: Branching Stochastic Process with Settlement. *Mathematical Medicine and Biology* (submitted). Preprint available on bioRxiv, DOI: 10.1101/294157.

In Chapter 2, I summarize the results of the above manuscript and highlight my own contributions.

Contributions

Study conception and design: C.F. and T.H. Analysis: C.F. and T.H. Parameter estimation and numerical simulations: A.R. Drafting of manuscript: C.F., T.H., and A.R.

Acknowledgements

I would like to take this opportunity to thank everyone that has helped me complete this work. First and foremost, I thank my supervisor, Dr. Thomas Hillen, for providing guidance, (constructive) criticism, and incredible opportunities for growth and development. Second, I thank the members of my supervisory committee — Drs. Gerda de Vries and Christoph Frei — for serving as academic advisors and for careful reading of my thesis. Third, I thank the members of the MathBio Journal Club at the University of Alberta for the useful discussions, debates, and suggestions. Fourth, I thank my office mates, friends, and family for the welcome distractions they provided. Finally, I would like to acknowledge that funding for this work has come through the University of Alberta, an NSERC CGS-M scholarship, and an Alberta Innovates Graduate Student Scholarship.

Contents

1	Introduction	1
1.1	Biological Background	1
1.1.1	Metastatic Cascade	3
1.1.2	Immune-Mediated Metastasis	14
1.2	Mathematical Background	16
1.2.1	Stochastic Approaches	17
1.2.2	Deterministic Approaches	19
1.2.3	Other Approaches	23
1.3	A <i>Successful</i> Model of Metastasis	24
1.4	Outline	25
2	A Stochastic Model for Cancer Metastasis	27
2.1	Setting and Model Derivation	28
2.2	Summary of Analytical Results	31
2.3	Application to Metastatic Cancer	38
2.3.1	Gillespie Algorithm	38
2.3.2	Application: Disease Spread	42
2.3.3	Application: Experimental Metastasis	49
2.4	Discussion	52
3	A Deterministic Model for Cancer Metastasis: Two Sites	56
3.1	The Model	56
3.2	Analytical Results	67

3.2.1	Steady States	68
3.2.2	Stability Analysis	72
3.3	Parameter Estimation	76
3.4	Numerical Results	78
3.4.1	Primary Resection	78
3.4.2	Immune Therapy	81
3.4.3	Injury at Secondary Site	85
3.5	Discussion	89
4	A Deterministic Model for Cancer Metastasis: Secondary Site	97
4.1	The Model	98
4.2	Analytical Results	101
4.2.1	Positivity and Boundedness	101
4.2.2	Steady States	105
4.2.3	Quasi-Steady State Analysis: Fast Tumor, Slow Immune	110
4.2.4	Quasi-Steady State Analysis: Slow Tumor, Fast Immune	114
4.2.5	Number of Steady States and Bifurcation Analysis . . .	122
4.3	Numerical Results	126
4.3.1	Parameter Estimation	127
4.3.2	Simulations: Primary Resection	134
4.3.3	Simulations: Immune Therapy	139
4.4	Discussion	141
5	Conclusion	150
	Bibliography	158

List of Tables

2.1	Parameters for quantities F , V , H , and Q	33
2.2	Stochastic Model Parameters	43
2.3	Injection Simulation Parameters	49
3.1	8 ODE Model Parameters	77
4.1	3 ODE Model Parameters Used for Figure 4.5	123
4.2	3 ODE Model Parameters	129

List of Figures

1.1	Cartoon model of the ‘immune-mediated’ model of metastasis	4
1.2	Immune Preparation of the Pre-metastatic Niche	7
1.3	Anderson’s Local Invasion	22
2.1	Illustration of a branching stochastic process with settlement. Taken from [50].	30
2.2	Simulation vs. theoretical: particle number	44
2.3	Spatio-temporal simulation dynamics	46
2.4	Region of metastatic influence	47
2.5	Gaussian and Laplacian Fits to Final Time Distribution	48
2.6	Comparison: Model output vs. Cameron data	50
2.7	Injection Simulations: population composition	51
3.1	Cartoon model of the 8 ODE Model of Metastasis	59
3.2	tanh Threshold Function	65
3.3	Establishment Rate as a function of time	67
3.4	DFSS Dynamics	69
3.5	MOSS Dynamics	70
3.6	FDSS Dynamics	72
3.7	Primary Resection Efficiency	79
3.8	Primary Resection Timing	80
3.9	Immune Therapy: Effects on Secondary Tumor	82
3.10	Immune Therapy and No Immune Education: Effects on Sec- ondary Tumor	83

3.11	Resection, Immune Therapy, and Tumor Education Inhibition	84
3.12	Effect of Injury Timing	86
3.13	Dynamics of Secondary Tumor Environment Upon Injury . . .	87
3.14	Injury and Establishment Rate	89
3.15	Metastatic Blow-up	94
4.1	Cartoon model of the 3 ODE Model of Metastasis	100
4.2	2D Slow Manifold	115
4.3	Null Surface	117
4.4	1D Slow Manifold	120
4.5	Steady State Possibilities	124
4.6	5 Steady States	125
4.7	Bifurcation in ϕ	127
4.8	Sensitivity Analysis — Three Timepoints.	131
4.9	Sensitivity Analysis — Full Timecourse.	133
4.10	Effects of Primary Resection: Extinction or Persistence	136
4.11	Effects of Primary Resection: Metastatic Blow-up	138
4.12	Effects of Primary Resection with Immune Response: Metastatic Dormancy	140

Abbreviations

BMDC	bone marrow-derived cell
CSC	cancer stem cell
CT	cytotoxic
CTC	circulating tumor cell/clump
DFSS	disease-free steady state
ECM	extra-cellular matrix
EGF	endothelial growth factor
EMT	endothelial-mesenchymal transition
FDSS	full-disease steady state
GFP	green fluorescent protein
IL	interleukin
MAM	metastasis-associated macrophage
MDE	matrix-degrading enzyme
MDSC	myeloid-derived suppressor cell
MOSS	metastasis-only steady state
MMP	matrix metalloproteinase
NK	natural killer
NSAID	nonsteriodal anti-inflammatory drug
ODE	ordinary differential equation
PDE	partial differential equation
PMN	pre-metastatic niche
SDF	stromal-derived factor
TAF	tumor angiogenic factor
TAM	tumor-associated macrophage
TE	tumor-educated
TGF	transforming growth factor
TNF	tumor necrosis factor
Treg	regulatory T cell
uPA	urokinase-type plasminogen activator
VEGF	vascular endothelial growth factor

Chapter 1

Introduction

In this chapter, we provide a brief review of the biology of metastasis, as well as of the theoretical approaches that have been used to gain insight into this complex phenomenon. Section 1.1 outlines the biology of metastasis, with an emphasis on the role of the immune system in preparation for Chapters 3 and 4. Section 1.2 outlines the mathematical models developed up to this point to address aspects of metastasis. Finally, the structure of this thesis is summarized in Section 1.4. The scientific literature on metastasis is significant and the references and results presented here have been chosen by their relevance to the current work and are not meant to be exhaustive.

1.1 Biological Background

Metastasis is the process by which cancer spreads to secondary sites. This spread can be relatively close to the location of the primary tumor — possibly remaining within the same organ and referred to herein as *local* metastatic spread — or it can be to distant organs, with dissemination of cancer cells from the primary site aided by the lymph and vascular systems — referred to herein simply as *metastasis*. Metastatic spread is often cited to be responsible for more than 90% of all cancer related deaths [57, 96, 133] and simple concepts such as the *seed and soil* hypothesis and the *metastatic cascade* have allowed us to gain an intuitive understanding of the metastatic process. However, many

of the details of these intuitive descriptions of metastasis are still unclear and additional research is needed in order to elucidate the underlying mechanisms responsible for clinically and experimentally observed dynamics. In this first section of Chapter 1, we review the process of metastasis as it has been, and as it is currently, understood. This review considers some of the new research bringing into question long-held beliefs — with special attention given to immune involvement, the main topic of this thesis.

For over a century, the spread of cancer from a primary site to a distant organ has puzzled researchers. In the late 1800's, Paget [110] first proposed a model for metastasis known as the 'seed and soil' hypothesis. Based on the observations of preferential metastatic spread patterns, Paget hypothesized that there were two key factors necessary for the successful establishment of a macrometastasis. First, the cells shed from the primary tumor — the *seed* — must be well suited to colonize distant and often hostile environments. And second, the distant site of potential macrometastasis formation — or *soil* — must be at least somewhat hospitable to these incoming cells. While a relatively old theory, it still has relevance today, with extensive work being done investigating both the 'seed' and the 'soil' components of Paget's theory. There is still great uncertainty as to whether all cells from the primary tumor are capable of initiating distant metastases, or whether there is a small subset of 'metastatic' cells (see Section 1.2 for relevant theoretical results). On the other hand, the idea of a *pre-metastatic niche* has been developed recently [84], and will be discussed in greater detail below (see Figure 1.2).

The preferential spread patterns upon which Paget based his hypothesis have now been well documented in a wide variety of cancer types. Theories attempting to explain the patterns of preferential spread all begin with cancer cells breaking away from the primary tumor and entering the vascular system (or, to a lesser extent, the lymphatic system) which provides the cancer cells with a method of rapid dissemination throughout the body. The theory of purely mechanical dissemination posits that blood flow patterns are sufficient to explain observed patterns of metastatic spread [18, 75] suggesting that metastases preferentially arise *downstream* of the primary tumor in the first location that the circulating tumor cells become stuck in small capillaries.

While this hypothesis provides a partial explanation for the observed patterns, it cannot fully explain them, with estimates that only approximately 66% of metastases can be explained by blood flow patterns alone [19]. Moreover, such an explanation would suggest that a source of tumor cells will eventually lead to metastatic colonization of targets downstream, but there is evidence that this is not always the case [57, 131]. Indeed, a study was performed in which patients received shunts that (inadvertently) released large numbers of cancer cells directly into their blood streams. Contrary to the purely mechanical description of metastasis, little to no evidence of increased rates of metastasis was reported [131].

Many attempts have been made to address the shortcomings of the purely mechanical explanation of metastasis, including genetically encoded tissue tropism [83], chemokine-mediated attraction of tumor cells with the appropriate chemokine-receptors inducing chemotactic movement of cancer cells towards areas of high chemokine concentration [57, 83] (the CXCR and CCR chemokine receptors have been of particular interest), and complimentary adhesive molecule pairing between the cancer cells and the homing site [57]. We remark that these hypotheses bear striking resemblance to the mechanisms of immune cell homing to sites of injury. We also note that there is a growing body of evidence that the observed tissue tropism patterns depend on factors derived from the primary tumor [84]. Indeed, Kaplan and collaborators demonstrated that the metastatic spread patterns of a specific cancer type could be altered by introducing factors derived from a different tumor type. The resulting spread patterns more closely resembled those of the tumor from which the factors were derived than the tumor being examined. Consequently, it appears that the spread patterns may be the result of complex interactions between primary tumor and secondary metastatic sites.

1.1.1 Metastatic Cascade

Few unifying theories of metastasis have been proposed beyond the conceptually straight-forward ‘seed and soil’ and ‘metastatic cascade’ descriptions. Because of the ubiquitousness of the metastatic cascade framework [57, 119, 133],

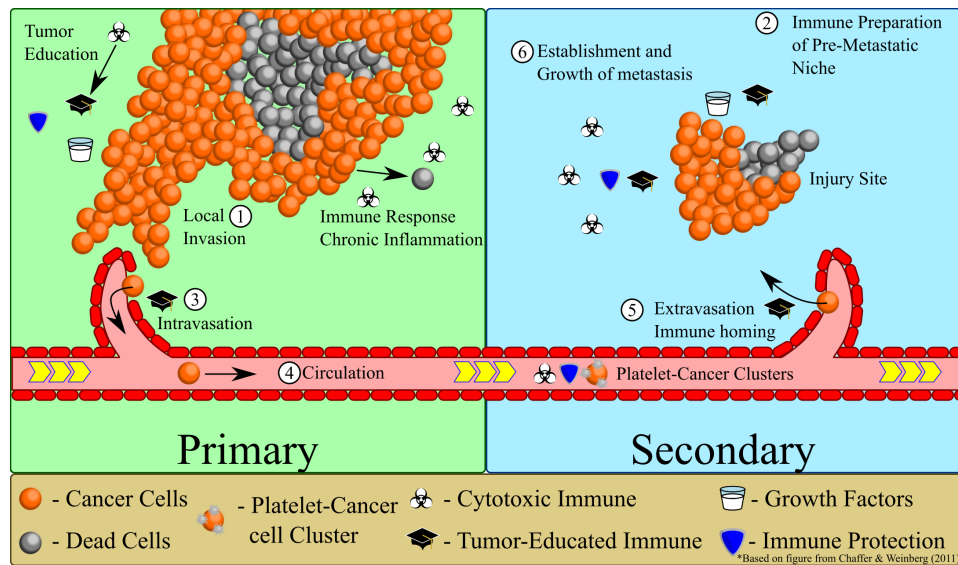


Figure 1.1: Cartoon model of the ‘immune-mediated’ model of metastasis (see Section 1.1.2). Based on figure from Chaffer and Weinberg (2011) [18].

we will organize the remainder of this section by the ordered sequence of biological events that make up the metastatic cascade. Before metastasis begins, the growth and development of a primary tumor must first occur. Growth of the primary tumor leads to local invasion of surrounding normal tissue (Figure 1.1 (1)) and can include the preparation of distant sites for later metastatic establishment (Figure 1.1 (2)). The local invasion eventually encounters a vessel of the lymphatic or circulatory system. Individual cancer cells — or small clusters of cells — can enter these vessels (intravasate) (Figure 1.1 (3)), thereby gaining access to rapid transport throughout the body. If these circulating cells (Figure 1.1 (4)) survive their journey and exit the vessel at some distant site (extravasate) (Figure 1.1 (5)), they may be able to establish a micrometastasis, especially at a prepared site. Evasion of local defenses and adjustment to the hostile foreign environment, or simply arrival at a hospitable prepared site, can see the *micrometastasis* grow into a *macrometastasis*. Further growth may eventually lead to a secondary tumor (Figure 1.1 (6)). These steps are highlighted in Figure 1.1.

The amount of research done investigating metastasis is expansive and can-

not possibly be summarized in its entirety here. Instead, in preparation for Chapters 3 and 4, we focus on one of the ‘hallmarks of cancer’ [60]: inflammation. (A recent review of metastasis and the immune system can be found in [78].)

Formation and Development of the Primary Tumor

The common view of inflammation and cancer is that the cancer cells have recruited the immunosuppressive regulatory T cells (Tregs) to protect it from any cytotoxic immune response by inhibiting T-cell function via secretion of interleukin 10 (IL-10) and transforming growth factor (TGF) β [48, 60, 96]. It has even been shown that Treg recruitment may be necessary for metastasis [87]. Moreover, it has been suggested [48, 124] that not only do Tregs prevent an effective anti-tumor immune response, but these cells may also play an active tumor promoting role. Indeed, chronic inflammation can result in the release of DNA damaging molecules (reactive oxygen and nitrogen species as examples), resulting in DNA damage and the potential for cancer initiation [117].

Contradictory anti- and pro-tumor effects are not unique to T cells, but have in fact been observed for several immune cell types (see Table 1 in [83] or the review in [27] for extensive lists with roles and references). Some researchers have gone so far as to describe these pro-tumor immune cells as *tumor-educated immune cells* [96]. Indeed, the tumor releases factors (including TGF β , IL-4, IL-3, and vascular-endothelial growth factor (VEGF)) which can actually change the phenotypes of macrophages (and neutrophils) from anti-tumor (type M1) to pro-tumor (M2) macrophages [34]. These M2 macrophages are recruited via colony-stimulating factor 1 (CSF-1) and VEGF-A among others [83]. Similar re-education programs have been observed for T helper cells, NK cells, and B cells [96]. Other cell types that have been implicated in primary tumor development, tumor initiation, or poor prognosis are myeloid-derived suppressor cells (MDSCs) which suppress anti-tumor immune responses [27].

The idea of a tumor’s necrotic core has been a key idea in cancer biology

for years, and it may be that this collection of necrotic cells plays a crucial role in the development of the tumor [60]. Indeed, necrosis causes inflammation by the release of pro-inflammatory signals into the surrounding microenvironment — which does not occur in programmed cell death (apoptosis) — causing the recruitment of inflammatory cells to the tumor microenvironment. These immune cells then produce a host of factors influencing tumor development. Growth and survival factors resulting in both increased proliferation and decreased death. Pro-angiogenic factors that aid in the development of blood vessels, providing oxygen and nutrients to the tumor mass. And extra-cellular matrix (ECM) modifying enzymes that facilitate local invasion by destroying or otherwise modifying the surrounding healthy tissue.

Remote Preparation of the Pre-Metastatic Niche

Early models of metastasis assumed a strictly mechanical distribution of cancer cells from the primary tumor. In these models cancer cells are shed from the primary tumor into the vascular system, which then transports the cells through the body until they become stuck in small blood vessels, where they extravasate and establish a micrometastasis. Therefore, metastases are always expected to occur ‘downstream’ of the primary tumor. It has been shown, however, that such a model cannot explain all observed metastatic spread patterns [19]. In order to address the short-coming of this model, a new concept has been introduced — that of the *pre-metastatic niche* (PMN). Two models of the PMN have been proposed [117]; one in which the PMN is a hospitable *location* for the adherence of circulating tumor cells and subsequent development of secondary tumors, while the other model posits that the PMN is better defined as a reservoir of monocytes (macrophage precursors) which help support the settled cancer cell develop into a secondary tumor at this distant site. In simple terms, the PMN is either the location, or the labor. In either case, we can describe the PMN as the hospitable *setting* in which secondary tumors are able to establish themselves. We can view this as a modern version of Paget’s ‘soil’.

In terms of the labor, the most well-documented workers involved are

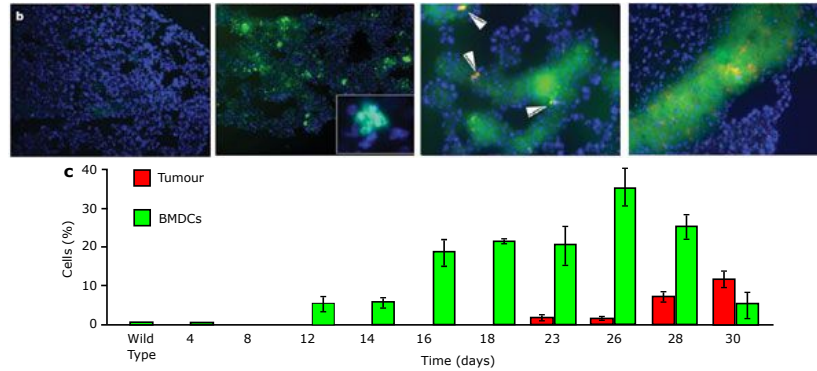


Figure 1.2: TOP: GFP⁺ bone marrow in the lungs after irradiation and before DsRed-tagged B16 cell implantation (left panel; n = 6). On day 14, GFP⁺ (green) BMDCs are seen with no DsRed⁺ (red) tumour cells (left middle panel and inset; n = 12). Beginning on day 18, a few single DsRed⁺ B16 cells adhere to GFP⁺ bone marrow clusters (right middle panel), and by day 23, DsRed⁺ tumour cells proliferate at cluster sites (right panel; n = 8). DAPI stain (blue) shows cell nuclei. BOTTOM: A graph showing flow cytometric data of bone marrow-derived GFP⁺ BMDCs and DsRed⁺ B16 cells in the lung. Figure and caption taken from Figure 1 in [84].

tumor-promoting inflammatory cells [60], including S100 proteins [83, 87, 117], bone-marrow-derived cells (BMDCs) [25, 83], myeloid-derived suppressor cells (MDSCs) [96], and platelets [83, 124] among others. Many, if not all, of these recruitments are orchestrated by the primary tumor, which has been referred to as a ‘chemokine producing factory’ [25], and which may package and send the factors/mRNA/etc. required for PMN establishment via extracellular vesicles [40]. For instance, the primary tumor may secrete factors such as VEGF-A, tumor necrosis factor (TNF) α and TGF β [139], which results in the increased expression of the immuno-attractant S100A8/9 proteins at the PMN. These proteins act as chemoattractants for BMDCs [83, 87], and some authors have even suggested that they can act as chemoattractants for cancer cells themselves [75]. These ideas have also been used to develop novel ‘metastasis traps’ [1]. Once localized to the PMN, these BMDCs help with adherence, invasion through secretion of ECM degrading matrix metalloproteinases (MMPs), and growth of the secondary tumor [87]. It has been observed [84] that these BMDCs are capable of homing to a future site of metastasis well before any

cancer cells have arrived anywhere within the vicinity.

Hypoxic cells have also been implicated in this process [25] through their secretion of lysyl oxidase (LOX) — an ECM protein — which increases invasion, metastasis, and recruitment of BMDCs to the PMN by altering the surrounding ECM. A feedback loop involving MDSCs and T helper cells has also been described [96]. MDSCs accumulate in the PMN, where they secrete factors (IL5, IL23, TGF β) which act to recruit T helper cells. The T helper cells in turn secrete IL17, which recruits tumor-promoting MDSCs.

Another hypothesis concerning the homing of circulating cancer cells to the PMN involves platelets acting as transport vessels [124]. In this case, the PMN may be nothing more than an injury site, which is naturally populated with growth factors present as part of a wound-healing response. However, if, as is hypothesized, cancer cells are transported from the primary tumor site to this injury site by activated platelets, then the wound healing site would provide an ideal locale for establishment of a secondary metastasis [17]. This hypothesis was also based on observations that metastatic tumors have been observed to occur at sites of injury, including after dental surgery as an example ([89] and references therein). The implication of platelets in metastasis has been made before (see [26] for example), but often in a protective role in the circulation phase which will be discussed in greater detail below. Platelets also secrete several factors, including growth and pro-angiogenic factors [27], and specifically stromal-derived factor 1 (SDF1), which aids in recruitment of BMDCs to PMN and has been implicated in the migration of some cancer cell types [83].

Local Invasion

If the dynamics of PMN formation is one of the least investigated steps in the metastatic cascade, primary tumor invasion is one of the most investigated. Here again, there appears to be an important role played by inflammatory immune cells. As mentioned earlier, inflammatory cells are attracted to the necrotic cells of the primary tumor. These recruited inflammatory cells aggregate near the boundary of the tumor, where they produce ECM degrading

enzymes as well as factors that induce the epithelial to mesenchymal transition (EMT) — in which non-motile epithelial cells undergo a transition to the more motile mesenchymal cell type — which is widely believed to be a crucial step in invasion and metastasis [60]. Because of the aggregation near the invasive front of the tumor, the idea of an invasive niche — composed of cancer cells, macrophages and epithelial cells — has also been proposed [83]. This idea is similar to that of an invasive cancer stem cell (CSC) niche along the boundary of the primary tumor [25]. In fact, if CSCs are the best candidates for distant seeding — because of their tumorigenic capabilities — then having a collection of them near the boundary, where they are more prone to separate themselves from the primary tumor and begin the migration to a distant site, is a potential strategy to increase rates of metastasis. The idea of a CSC niche near the boundary has also been investigated theoretically in models concerned exclusively with CSC dynamics [114, 129].

In order to separate themselves from the primary tumor — a first step to entering the vascular system — a path must be cleared in the surrounding ECM. While there is evidence that tumor cells are able to produce ECM degrading factors on their own, it has been hypothesized that the tumor cells recruit inflammatory cells, BMDCs and macrophages in particular, to the boundary to exploit the ECM degrading factors they produce [60, 83]. Some cancer types use acid to destroy the surrounding ECM and allow for easier local invasion, and has even been shown to play a role in EMT [2, 3, 52].

The ECM structure itself can play an important role for local invasion and migration [117]. Indeed, within the ECM there are structural fibres, known as fibrillary collagen 1, which are anchored to the surrounding blood vessels. Cancer cells can use these structural fibres as ‘zip-lines’ allowing them rapid access — movement along these fibres is up to $10\times$ faster than by other means [24] — to the vascular system and consequently anatomically distant sites.

Moreover, there appears to be an endothelial growth factor (EGF) - CSF1 feedback loop between a breast cancer cell line and tumor-associated macrophages (TAMs) [83, 117]. In this loop, the TAMs produce endothelial growth factor (EGF) which increases the tumor’s invasiveness. The cancer cells, in turn, produce CSF1, which is a powerful chemoattractant for TAMs, thereby pro-

ducing a self-regulating loop resulting in increased aggressiveness and local invasiveness. The regulation of this aggressive macrophage phenotype is accomplished by T cell secretion of IL4 [117]. The effect of this feedback loop has also been investigated theoretically (see Section 1.2.3).

Intravasation

Dissemination of cancer cells from a primary tumor site to distant sites is accomplished largely through the blood system [83]. While cancer cells can be found in lymph nodes, it is not believed that they travel large distances through the lymphatic system [19]. In addition to influencing local invasiveness as we saw in the previous section, the EGF-CSF1 loop appears to be critical to successful entrance into the blood stream (intravasation) as well [87]. Indeed, blocking the expression of CSF1 effectively inhibits metastasis but has little to no effect on the growth of the primary tumor. This phenomenon is a recurring one for several factors tested and demonstrates that metastasis is, in a certain sense, a separate process from primary tumor development.

Additionally, there is a connection to factors associated with CSCs in this step [25]. In particular, the transcription factor ‘TWIST’ has been implicated in migration in embryonic development as well as in regulation of EMT in cancer progression. Suppression of TWIST reduces metastasis but does not effect the primary tumor. As in local invasion, matrix degrading enzymes play a role in intravasation, the details of which are left out for brevity.

By and large, the main players in cancer cell intravasation are TAMs. In fact, specific studies (see references in [83] and [96]) noted that intravasation was only observed where perivascular TAMs were located. Moreover, TAMs — along with MDSCs and Tregs — produce cytokines (ex: $TGF\beta$) that induce EMT [96].

Circulation

Once a group of one or more cancer cells has entered the blood stream, the traditional view is that the transportation is done passively via the current of the vascular system. As a consequence, the only thing that the cells have to do

is survive this inhospitable medium. Indeed, upon entrance into the vessel, the cells move from a relatively static environment to one that is rapidly moving, and shear forces become a problem, often causing the rapid disintegration of the cells. Beyond this physical barrier, the cell types populating the blood vessels are also hostile to invading cancer cells such as natural killer (NK) cells of the innate immune system.

It is natural, then, that most of the research in this area has focused on the survival of circulating cancer cells in the vasculature. In a specific model of experimental breast cancer, Tregs have been shown to be necessary for metastasis [87, 96]. It is hypothesized that these cells protect the circulating cancer cells when they reach their destination. There has also been work implicating macrophages in this process [87, 96], but the vast majority of the work has focused on the protective role of platelets during circulation [83, 87]. Platelets may act as shields from NK cells and the shear forces present in circulation, and help protect the cancer cells at their final destination. This shielding effect is largely mediated through the formation of cancer cell-platelet clumps. Increased platelet counts have been associated with decreased survival in several cancer types including breast, colorectal, and lung among others, and anti-coagulant treatments and non-steroidal anti-inflammatory drugs (NSAIDs) have also been shown to decrease rates of metastasis [83, 98].

While this all seems reasonable, some recent evidence brings into question this assumed protective role of platelets during circulation [26]. Indeed, Coupland and collaborators demonstrated that platelets aid in metastasis even when NK cells are not involved, suggesting that protection may not be the only function of platelets. Moreover, even when NK cells were involved, Coupland et al. showed that their action occurred *after* that of the platelets. That is, while the platelet-cancer clumps were active, the NK cells were not and vice versa. As a result, the role of platelets in metastasis remains unclear. One new hypothesis is that activated platelets actively transport cancer cells from a primary tumor to a secondary site of inflammation [124].

Extravasation

It is estimated that tens of thousands of cells are shed from the primary tumor each day, but less than 0.01% of these cells will survive circulation and successfully extravasate and eventually develop into a macrometastasis [83]. It is believed that extravasation and secondary establishment are the least efficient steps in the cascade [117]. Experimental metastasis assays suggest that nearly 20% of the cells that leave the primary tumor perish before arrival at a secondary site [15, 97]. Naive approaches understand extravasation as the opposite process to intravasation, but this may be a little too simple.

The first question that extravasation seems to invite is: *why here?* Traditionally there have been two answers offered for this question [83]. The first is genetic; specific tissue tropisms are simply coded for in the cancer cells' DNA. The second is chemical [35, 75, 83, 87]; chemicals or secreted factors present at the secondary site act as chemoattractants for only those cancer cells with appropriate receptors (the most common example is CXCR4 [105]). While both of these offer possible answers, neither is particularly well developed. However, the recent hypothesis in [124] addresses these shortcomings — at least in the case of inflammatory tumors. Shahriyari hypothesizes that metastases develop at sites of injury or inflammation as a result of being transported there directly by activated platelets attracted to this site of injury.

The second question is : *how?* This has been investigated more than the previous question, but much remains unknown. However, general consensus in this regard is that, once again, immune cells have a major role to play. Much like the TAMs described in previous sections, the idea of metastasis associated macrophages (MAMs) has been developed [87, 96, 117]. These MAMs provide short-range growth and survival signals, protecting the cancer cells from hostile environment of the blood vessel and surrounding microenvironment. Moreover, they also appear to help in the process of moving through the blood vessel wall through direct contact with the cancer cells. Platelets have also been implicated [87]. The proposed platelet aided extravasation occurs as follows: platelet-cancer cell clumps are easily caught in the thin capillaries, platelets provide survival signals at this location and recruit inflammatory monocytes,

which then differentiate into MAMs, which in turn promote extravasation through direct contact. Some factors possibly implicated here are TGF β , CCL2, and VEGF-A. It is important to note however, that extravasation can occur independently of platelets [26].

Development of Macrometastases

Once the cancer cells have escaped the blood vessel, they must once again travel through the ECM to a location suitable for growth. The cells may once again follow the structural fibres, but these are not necessarily attached to the desired endpoint as was the case in local invasion/intravasation. Another idea — the so-called ‘pioneer’ hypothesis, wherein early arrivals ‘pave a path’ through the ECM, depositing adhesion molecules as they go, thereby leaving a trail for future arrivals [25]. In order to help visualize this phenomenon, we can view this as a person walking through a corn field, leaving a clear path through to their destination.

No matter *how* they make it to their terminal secondary site, once there, in order to successfully establish a secondary tumor, need to survive and proliferate. Indeed, this new location is likely incredibly different from that of the primary tumor, and so this cancer cell would still be ‘fish out of water’. Luzzi, Cameron, and colleagues [15, 97] found that the transition from quiescence to proliferation upon arrival at a secondary site was the rate limiting factor in metastasis — see also our discussion in Section 2.3.3. Often, these micrometastases do not develop into full blown secondary tumors, but may remain dormant for long periods of time [60]. These dormant micrometastases are often revealed after resection of the primary tumor, at which time ‘explosive’ metastatic growth may be observed. Several hypotheses have been proposed to explain this dormancy, including active suppression of secondary growth by the primary tumor (anti-angiogenic factors for example) [56, 64], time required to adapt to the new environment [19], active growth suppression by the host ECM [19], lack of nutrients [19] or even an immune response [45].

As we have seen before, the immune system appears to play contradictory roles. Indeed, inflammatory cells and BMDCs at the secondary site may

‘awaken’ dormant cells by providing survival and proliferation signals [60, 83]; recruitment of MAMs is essential for dissemination and growth at secondary sites [87]. Also, direct contact between platelets and cancer cells at this secondary location, along with platelet-derived $TGF\beta$ increases the survival of these cancer cells [87]. Inflammatory stromal cells and the primary tumor also supply the secondary site with $TNF\alpha$, which promotes adhesion and protection from NK cells [83]. In Chapter 4 we explore the role of contradictory immune effects on metastatic dormancy.

Because of the presence of the primary tumor, which is a ‘chemokine factory’, it is likely that development of the secondary tumor is similar, but not identical to the initial development of the primary tumor.

1.1.2 Immune-Mediated Metastasis

As we have seen in the previous section, there is a significant amount of research linking the immune system — with inflammation in particular — to cancer [136, 7]. A link between the immune system and cancer has been noted for a long time, with tumors even being described as ‘wounds that do not heal’ in the 80s [41, 42], and postulated to be the result of an uncontrolled healing process [101]. But it is only recently that an *explanatory* link to metastasis has been proposed [124].

Shahriyari [124] has recently proposed a theory of ‘immune-mediated metastasis’. In this hypothesis, the immune system plays a crucial role in the dissemination, establishment, and growth of metastases. Shahriyari also notes that chronic inflammation can, in itself, lead to the *formation* of a primary tumor (through release of reactive oxygen species for example), but for the context of this thesis, we will assume that a primary tumor has already developed, and will consider the influence of the immune system on metastatic spread from this pre-existing primary tumor.

In a region of chronic inflammation, Shahriyari suggests that local immune cells can become ‘adapted’ to the inflammatory environment. This ‘adaptation’ could take the form of increased release of growth-promoting and pro-angiogenic factors in order to compensate for what may seem to be an unre-

sponsive wound (for example) and, when combined with possible ‘T cell exhaustion’ [80] — a phenomenon in which cytotoxic T cells lose their potency — could lead to an environment conducive to rapid, uncontrolled growth. Similar changes in immune response as a result of tumor interactions have been reported elsewhere, including the observation of spontaneous transition between cytotoxic T cells to immunosuppressive Tregs as a result of factors within the tumor microenvironment [107]. For this reason, Liu used the term ‘tumor-education’ (which we borrow in Chapters 3 and 4) to describe the change in immune phenotype observed within the tumor microenvironment [96].

We have established how chronic inflammation can influence the immune environment at the site of a primary tumor, now we look to make the connection to metastatic spread. First, we note that chronic inflammation can act as a stabilizing force for a hybrid epithelial/mesenchymal phenotype which has been shown to highly efficient at seeding metastases [81]. Second, in a highly inflammatory environment, the rate of cancer-platelet cluster formation may be large. The formation of these clusters will render the dissemination process much more efficient in terms of the protection and help platelets provide with the different steps in the metastatic cascade (see Section 1.1.1). Third, immune trafficking between sites of injury may provide these cancer-platelet clusters with rapid access to distant hospitable locations. To see this, let us assume that an injury occurs at some site distant from the primary tumor. A directed immune response will be activated. The wound-healing site — full of growth-promoting, pro-angiogenic, and immunosuppressive factors — becomes a welcoming PMN. Cancer cells find their way to this PMN by virtue of being clustered with activated platelets, which home to sites of injury. Finally, tumor-educated immune cells from the primary tumor site may also arrive and maintain the inflammatory wound-healing environment after the injury has been repaired. This allows the cancer cells to not only successfully establish a micrometastasis, but to develop into macrometastases as well. This general process is highlighted in Figure 1.1.

While this theory of immune-mediated metastasis sounds intriguing and is supported by several experimental results, its feasibility as a unifying theory

of metastatic spread remains untested. Though experimental studies of this hypothesis may be difficult, theoretical investigations need not be. Indeed, the implications and validity of this hypothesis are the motivation for the models and work presented in Chapters 3 and 4.

1.2 Mathematical Background

Because of the difficulty in performing experimental research into the dynamics of metastasis, the process is a prime candidate for mathematical/theoretical exploration. While there have been attempts to model this process dating to the 1970s, there has been no coordinated effort to develop a systematic, theoretical description of metastasis, and more mathematical investigations of metastasis are needed [53]. Much like the work on the experimental side, theoretical investigations have tended to focus on a specific step of the metastatic cascade. And, as in experimental case, the bulk of this work has been done for local invasion or the development of the ‘metastatic phenotype’. In fact, many of the models described below simply *assume* that distant metastatic spread has occurred when cells from the primary tumor migrate ‘far enough’ from the primary tumor [30, 122]. The methods used range from stochastic models, to discrete cell-based models, to continuous ODE/PDE models, and the approaches can be broken into the largely theoretical and the data driven. Unfortunately, the data available is far too coarse/general to gain truly meaningful insights, and therefore the bulk of the data driven modeling has proven limited in its power. In what follows, we outline the different approaches and methods used to investigate metastasis. While the works discussed here certainly do not make up an exhaustive list of all the work that has been done on this problem, it does provide a sufficient overview of the current state of affairs. A (relatively) recent review of the models of metastasis is presented in [123].

1.2.1 Stochastic Approaches

Based on the understanding of metastasis as an inherently random process, a number of investigators have developed stochastic models of metastasis. In particular, there have been a few groups focused on the development, analysis, and application of such models. The Liotta group [94, 95], the Michor group [39, 58, 59, 103, 104], and the Hanin group [10, 61, 62, 63, 64] have been particularly active in this area.

The earliest results are courtesy Liotta and collaborators. In [95], the authors considered a two-dimensional Markov process model which describes the development of metastases from circulating clumps of tumor cells. Intravasation and death rates for the cancer cell clumps were considered, as well as a rate of metastatic establishment. Upon calibration of the model to experimental data, it was used to simulate the effect of treatments that prevent the formation of large cancer cell clumps or that increases the cancer cell clump death rate within the circulation. In a subsequent paper [94], the same group developed an expression for the probability of being metastasis-free — in the sense that no metastases have yet developed and not in the sense discussed in Chapter 2 — as a function of time which they were then able to compare to experimental data. Included in this expression are the rate at which CTCs become lodged in a target-organ’s vasculature and the probabilities that an arrested cell will either die or develop a metastatic focus. Liotta and collaborators also investigated metastasis with the help of deterministic ODE models as well [93, 121], which we will discuss further in Section 1.2.2.

A couple of decades after the pioneering work mentioned above, Michor and collaborators [39, 58, 59, 103, 104] developed and refined a stochastic model to investigate the emergence and role of the ‘metastatic phenotype’ among the tumor cells within the primary tumor. In [104], the authors considered a tumor population with a fixed number of cells split into two subpopulations of cells: one that cannot metastasize, and another that can. At each cell division (time step) a mutation conferring the mutant cell the ability to metastasize can occur with some fixed probability. Cells with metastatic potential can be ‘exported’ from the primary tumor to seed a distant metastasis at a fixed

rate. Consequently the number of established metastases in this model will be proportional to the number of mutated (i.e. of ‘metastatic’ phenotype) cells in the primary tumor. The authors concluded that if the ‘metastatic mutation’ confers an advantage at the primary site, then most, if not all, cells within the primary tumor will (eventually) have the potential to seed metastases. On the other hand, if the ‘metastatic mutation’ proves deleterious at the primary site, only a small fraction of the primary tumor will have the capability to metastasize. Similar results were presented in [103], but with two mutations required to acquire the ‘metastatic phenotype’. Generalizations to a growing primary tumor are analyzed in [39] (single mutation) and [58, 59] (two mutations).

More recent stochastic modeling has been done by Hanin and collaborators [10, 61, 62, 63, 64]. In these works, the authors developed a general stochastic framework for the metastatic process that, when applied to research or clinical data, can estimate the *natural history* of that specific cancer. Factors included in this natural history are the time of first metastasis formation, the number of metastatic foci, rate of shedding from primary tumor and effect of primary tumor resection. These works suggest that metastasis can occur relatively early in the progression of the primary tumor (contrary to the prevailing belief that metastasis is the final step in malignant progression), that shedding is likely homogeneous in time and that the explosive metastatic growth after primary tumor resection may be the result of the flipping of an angiogenic switch with the removal of primary tumor. In their most recent work [62], the authors demonstrated that increasing the growth rate at metastatic sites *post* primary resection *always* provides a higher likelihood when fitting their model to *any* data set. They used this to argue that metastatic development is highly influenced by the primary tumor, and that both metastatic dormancy (when primary is present) and blowup (upon primary resection) are basic properties of metastasis.

1.2.2 Deterministic Approaches

Whereas stochastic models may provide a certain level of *realism* to the model — especially when small numbers of cells are being considered — there have also been several deterministic models formulated in order to interrogate the metastatic process because of their relative ease of analysis. Below we outline the approaches taken by several investigators. We will note that only a small fraction of the literature explicitly models metastasis, with most of it focusing instead on a single component of the metastatic cascade, with local invasion being particularly well studied.

One of the earliest attempts at developing a theoretical framework for metastasis was done by Saidel and colleagues in 1976 [121]. The authors developed a 5 compartment ODE model meant to model the different stages in the metastatic cascade. Compartments included in the model are primary tumor size, vasculature of primary tumor, invading cells within blood vessel walls, cancer cells arrested in end organ tissue and number of metastatic foci. Each compartment is modeled relatively simply with birth-death processes with rates of varying complexity. This model was then fit to mouse data that was obtained concurrently. The calibrated model was then used to predict dynamics following tumor trauma, amputation and a number of other scenarios. Elements of this model were adapted and included in a stochastic model that attempted to predict number of metastatic foci and probability of no metastases existing after tumor initiation [95, 94] (see Section 1.2.1).

Another well investigated model is the Iwata PDE model describing the colony size distribution of metastases [77]. The model itself is a simple transport equation — for which the authors provide an explicit solution — incorporating primary tumor growth and shedding in a density-dependent manner. Growth was assumed Gompertzian, and vascularisation of the tumor was also included. This model was then fit to clinical data (metastatic colony numbers as a function of colony size and time) and used to estimate the natural history of cancer. Similar estimation of cancer history was done in [68] using the same model. Many researchers have based their investigations on the model developed in [77], including mathematical analysis in [11, 36], compu-

tational/numerical analysis in [9, 66], and in application to data from mice in [67].

More recently, the validity of the Iwata model has been brought into question by Baratchart et al. [8] with work that suggests that metastatic foci do not grow independently of the primary tumor and nearby metastatic foci. The authors gathered metastatic burden data via MRI imaging and fit the Iwata model to this data. If they reduced their collected data to be of the same form as in previous investigations, Baratchart et al. were able to fit the model — much as previous researchers have. However, once they took advantage of their more detailed data, they discovered that the model was actually a poor predictor of both number of metastatic foci and overall metastatic burden, which led them to investigate the influence of several micrometastases developing in close proximity to one another by developing a spatially explicit model that included tumor cells, healthy cells and a pressure field. This ‘post-establishment’ model of metastasis provided an explanation for the poor fit of the previous model to their data: there are non-trivial interactions between metastatic foci and possibly between metastases and the primary tumor.

Using a spatially explicit PDE model, Orlando et al. in [109] investigated the role of the primary tumor environment on the development of the ‘metastatic phenotype’. The model includes both cancer cells (with continuously varying phenotypes) and surrounding healthy cells, along with oxygen concentration. The authors considered two variants of the model - one in which the tumor destroyed its surrounding environment, and one in which no such destruction occurs. It was found that environmental destruction selected for a more invasive phenotype, and that the spatial distribution of phenotypes mirrored phenotypic distributions observed in ecological settings, with invasive cells near the tumor boundary and more ‘permanent’ cells in the interior of the tumor.

Eikenberry et al. [45] developed a detailed PDE model of local invasion in skin cancer which includes tumor cells, healthy cells, tumor angiogenic factor (TAF), blood vessels, necrotic cells, oxygen, basement membrane density, cytotoxic immune cells and immuno-attractant factors. In order to model the effect of the primary tumor on secondary metastases, the authors simulated

the model for a fixed time, allowing for the development of a primary tumor. Secondary metastases were then manually added to the simulation domain assuming that metastases are more likely to develop closer to the primary tumor boundary. After manual seeding, the simulation was restarted, and the effect of the primary on the metastases was then observed. One scenario tested was the effect of primary tumor resection. In this case, the model predicted explosive metastatic growth or, if the immune response was sufficiently strong, small but persistent metastases. The effects of primary tumor resection on metastatic growth was also investigated in [38] using an ODE model. Similar results were obtained there, with the effects of primary tumor resection ranging from nothing, to explosive metastatic growth, to extinction of all metastases, depending on the parameters used.

Modeling of local invasion by way of healthy tissue destruction has been done by several authors, including Gatenby [52], Anderson [5], and Chaplain and Lolas [20, 21]. Gatenby [52] investigated the role of acid-mediated destruction of healthy tissue on primary tumor invasion dynamics with a reaction-diffusion model including equations for healthy tissue, cancerous tissue, and excess hydrogen ions (acidity). The model predicted a gap between the tumor front and the healthy tissue which had not been appreciated previously, and was subsequently confirmed experimentally. Anderson [5] proposed a similar three component model, including ‘matrix degrading enzymes’ instead of the hydrogen ions considered in [52]. Under certain parameter regimes, Anderson’s model predicts that a small cluster of cancer cells will break away from the main tumor mass, traveling independently ahead of the main tumor (see Figure 1.3) which the authors suggest will result in metastatic spread. The models of Chaplain and Lolas [20, 21] are similar, but focus specifically on the effects of the proteolytic enzyme urokinase-type plasminogen activator (uPA). The authors performed numerical simulations of the model using parameters estimated from the literature. These final uPA models have been analyzed further in [74], where it was shown that, under certain conditions, the model converges to a chemotaxis model.

Some of the most recent work — and most relevant to metastasis — comes from the Enderling lab in a series of papers refining a model for investigat-

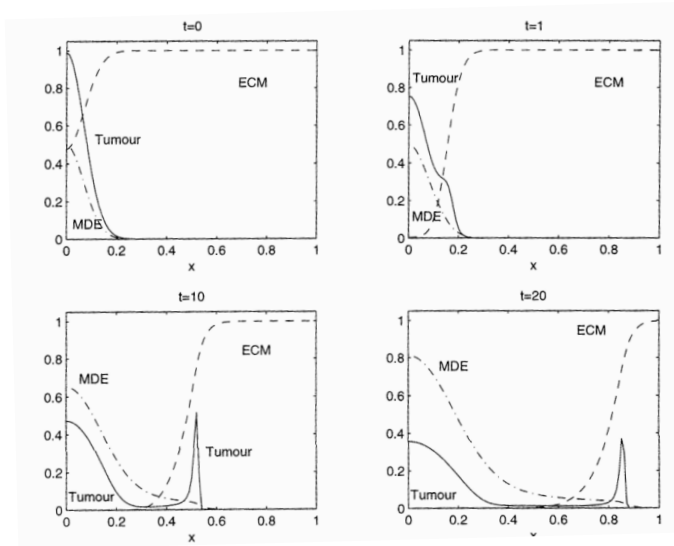


Figure 1.3: One-dimensional simulations of the model of Anderson et al. [5] showing spatial profiles of tumor density, extra-cellular matrix (ECM) density, and density of a matrix-degrading enzyme (MDE) at 4 different time points. Figure taken from Figure 2 in [5].

ing the role of T-cell trafficking on the so-called ‘*abscopal effect*’ in radiation therapy [115, 116, 135, 134]. The ‘*abscopal effect*’ describes the phenomenon in which therapy applied locally to one tumor affects a distant tumor, which was not directly targeted by the therapy. These works model tumor-immune dynamics at N distinct anatomical sites. The dynamics at each site are governed by a modified version of Kuznetsov’s tumor-immune model [91], which includes equations for a tumor population and an effector (cytotoxic) immune population. The effector immune cells can travel between metastatic sites by way of an anatomically informed network, but tumor cells from site i remain at site i . Because of this, their model provides little in the way of meaningful information concerning metastatic spread, but is an effective model of the *abscopal effect* in a system of multiple pre-established tumors. In [115], after parameterizing the model, the authors showed, by way of numerical simulation of their model using up to $N = 3$ sites, that the strength of the *abscopal effect* depends on which site receives the local radiation. Further work on this model has included discussion of clinical trial design based on the model [135],

and further simulations of what the authors call ‘metastatic seeding’ and local therapies leading to abscopal effects [134].

1.2.3 Other Approaches

There have also been models proposed that do not necessarily fit nicely into one of the categories outlined above. This includes computational models [88, 127], agent-based models [22, 120, 132], and hybrid models [4].

Chen et al. [22] developed an agent-based model to investigate the environmental selection of the ‘metastatic phenotype’ at the primary tumor site. The model includes tumor cells, blood vessels, nutrient/oxygen diffusion and metabolism, and looked at role of resource heterogeneity on development of invasive phenotype. Metastatic cells were found to be at a disadvantage within the primary tumor because these cells are spending extra resources maintaining this phenotype that does not help them survive within the primary tumor. Moreover, resource heterogeneity was shown to select for invasion — which the authors suggested may lead to metastatic spread. This effect mirrors a similar effect in ecology, where organisms will travel larger distances if the resources are spread out over a large area [14, 102]. Another agent-based model with similar scope was developed and analyzed in [120], in which the acid mediated theory of invasion [52] was also included.

The role of adhesion in primary tumor morphology and spread has also been an active area of research, with many investigators making links to metastatic spread. In [4], Anderson looked at the role of adhesion in local invasion using a hybrid continuous-discrete simulation model. Additional models for cellular adhesion include: a continuous integro-PDE model developed and analyzed in [6, 111], an agent-based model in [132], and a computational model in [127]. The computational model [127] investigated the role of adhesion in primary tumor morphology and found that decreased adhesion strength (both cell-cell and cell-ECM) can result in highly fragmented tumors, which the authors argue could lead to metastasis. Morphological results were obtained in [111] using a PDE model of local invasion including cell-cell and cell-ECM adhesion, and in [4] using a hybrid model.

Among all the models reviewed here, there are very few that also include any form of immune cells. We previously mentioned the work of Eikenberry and the Enderling Lab, and here we describe two more. First, Knutsdottir and colleagues [88] investigated the role of macrophages in primary invasion. They developed a computational model to simulate dynamics of individual cells within the tumor microenvironment and the effect of CSF1-EGF signaling on tumor cell/macrophage motility. The model incorporates tumor cells and macrophages together with the chemical signaling molecules CSF1 and EGF (see Primary Invasion in Section 1.1). CSF1-EGF signaling proved to be sufficient to replicate observed experimental results of increased motility of both cell types. Second, Uppal et al. [132] investigated the role of platelets and adhesion in the metastatic cascade using an agent-based model. Instead of looking at the role of adhesion in primary tumor invasion and morphology, the authors considered the role of adhesion in distribution and establishment of micrometastases at distant sites and found that inhibiting platelet adhesion reduced tumor cell adhesion at secondary sites, which was interpreted as a decreased rate of metastatic colonization.

1.3 A *Successful* Model of Metastasis

Before we get started, we gather the results discussed above into a list of properties that are desirable in a *successful* model of metastatic cancer. Although our list may not be exhaustive, it is meant to serve as a set of motivating principles to be kept in mind throughout the thesis and in the final chapter we will summarize our results in part by comparing them to this list.

What *should* a successful model of metastatic cancer look like? Based on our discussion above we suggest the following properties are desirable in a *successful* model of metastatic cancer.

Can the model (re)produce:

1. establishment and development of a secondary tumor at a site distant from the primary tumor?
2. immune-mediated help in metastatic establishment? [84, 124]

3. metastatic dormancy? [62, 138]
4. metastatic blowup upon primary resection? [56, 62]
5. abscopal effects? (these are the effects felt by the secondary tumor in response to treatment of the primary tumor) [37, 112, 134]
6. metastasis to sites of injury? [124]
7. prescriptions for more effective therapies?
8. testable biological predictions?
9. local recurrence?
10. tumor specific patterns of spread?

1.4 Outline

The remainder of this thesis is organized as follows:

- Chapter 2 discusses a stochastic model for cancer metastasis. The model includes stationary particles (established tumors) and mobile particles (CTCs). Stationary particles can give birth to mobile particles, which move according to a stochastic process until they perish or settle at a secondary location, thereby establishing a new stationary particle at a distant location. We show that the stochastic model can be described in terms of a new type of integro-differential equation whose long term dynamics are governed by a single number we term the *metastatic reproduction number*. The model is parameterized using murine data from experimental metastasis assays, and numerical simulations are performed demonstrating the applicability of the model framework to metastatic cancer.
- Chapter 3 includes the development of an ODE model for cancer growth at two different anatomical sites. An 8-dimensional ODE model is presented, modeling the dynamics of tumor cells, necrotic cells, anti-tumor

immune cells, and pro-tumor ‘tumor-educated’ immune cells at both a primary and a secondary site. Criteria for disease extinction are obtained, and the parameterized model is simulated numerically. We find that our model provides theoretical support for the theory of immune-mediated metastasis with simulations reproducing experimentally and clinically observed dynamics including rapid metastatic growth at the sites of injuries.

- Chapter 4 begins with a simplification of the 8-dimensional ODE model from Chapter 3 to a 3-dimensional ODE model of tumor-immune dynamics, including both anti- and pro-tumor immune populations, at a metastatic site. Under the assumption that tumor dynamics and immune dynamics occur on different time scales, we perform quasi-steady state analysis of the model using techniques from geometric singular perturbation theory. Our analysis provides insight into the phenomena of metastatic dormancy, metastatic ‘blow-up’, and abscopal effects, thereby providing theoretical support for the theory of immune-mediated metastasis as well as a number of biological predictions.
- A summary of our results and concluding remarks are presented in Chapter 5.

Chapter 2

A Stochastic Model for Cancer Metastasis

The material of this chapter is included in a submitted manuscript:

C. Frei, T. Hillen, and A. Rhodes. A Stochastic Model for Cancer Metastasis: Branching Stochastic Process with Settlement. *Mathematical Medicine and Biology* (submitted). Preprint available on bioRxiv, DOI: 10.1101/294157.

Here, in Chapter 2, I summarize the results of the above manuscript and highlight my own contributions.

In this section, we derive, analyze, and apply a stochastic model of particle dissemination — which we term a *branching stochastic process with settlement* — to the problem of cancer metastasis. Section 2.1 introduces the general setting and provides the derivation of the stochastic model. We provide a summary of analytical results in Section 2.2. (Proofs of these results have been left out here for brevity, but can be found in the paper [50].) There are two sets of main results. The first set deals with the characterization of the following key quantities in our stochastic model: the expected location F of metastases, their locational variance V , the distribution H of the furthest invading metastasis, the metastatic extinction probability Q , and the ratio of moving versus stationary cancer cell groups. Each of the first four quantities — F , V , H , and Q — satisfies a non-local integro-differential equation with

distributed delay. These non-local differential equations are of the same type for all cases and are non-linear in some cases. The second set of main results provides a simple classification of the asymptotic behavior. Despite the model complexity and stochasticity, we are able to find a *metastatic reproduction number* R_0 , which is explicitly given in terms of the rates of metastatic shedding, settlement, and death. The magnitude of R_0 governs the asymptotic behavior of the model dynamics. A discussion of the numerical methods used to simulate the stochastic model is presented in Section 2.3.1 and application of the model in the context of metastatic cancer is done in Section 2.3. The model is parameterized using data from murine models of experimental metastasis and simulations of metastatic spread and of experimental metastasis assays are presented. Discussion of the results, their implications, and their limitations is done in Section 2.4

2.1 Setting and Model Derivation

Even though it is implicated in the vast majority of cancer-related deaths, the inherently stochastic nature of metastasis makes experimental studies difficult, meaning that a thorough understanding of the process is lacking. While some of the steps in the *metastatic cascade* are well understood — for example, growth and invasion of primary tumors are well studied both experimentally and theoretically (see the reviews in [119, 123] or in Section 1.1) — understanding of others remains elusive. Travel *to*, and establishment *at* secondary sites are particularly poorly understood, with many theoretical investigations ignoring these aspects altogether (see Section 1.2). Though recent results [84] have led to novel theories that metastasis may be more intricately orchestrated than previously thought [124], the process is still believed to be at least partly stochastic.

Based on these observations, we introduce a new stochastic framework for metastatic spread in the form of a *branching stochastic process with settlement*. This model captures simultaneously temporal and locational dynamics. Stationary tumors emit, or shed, small clusters of cells into the vasculature

at random times. These shed clusters can then move randomly through the body, modeled by a stochastic process. While the detailed movement through the body is complicated, we will use Brownian motion as a first example (see also the discussion in Section 2.4). The moving clusters — also known as circulating tumor cells/clusters (CTCs) — can settle randomly according to a given rate. If the CTCs successfully settle, they may establish a secondary tumor, which itself may shed new CTCs into the blood stream. Both moving and stationary groups of cancer cells die, each at their own rate.

In contrast to existing stochastic metastasis models (see Section 1.2.1), our framework accounts for both travel between primary and secondary sites and establishment at the secondary sites. [65] propose a stochastic model with secondary metastatic emission as a cascade of Poisson point processes and link it to the deterministic model introduced by [77]. Differently from us, [65] model only the size development over time and not the location.

We define the *branching stochastic process with settlement* as follows: We start with one tumor that is located at locational position 0. We assume that the tumor sheds individual cells and small groups of cells into the circulatory system. It is believed that such CTCs are most responsible for metastasis formation [51]. Hence, in this model, we focus on the shedding of cell clusters. At a random time ν , the primary tumor emits a cell cluster, which starts moving randomly. We model the movement of this cell cluster by a stochastic process $(B(t))_{t \geq 0}$ with cumulative distribution function $G(t, x) = P[B(t) \leq x]$ for $x \in \mathbb{R}$ and $t \geq 0$. We assume that for every fixed t , $G(t, \cdot)$ is absolutely continuous so that there is a density function $g(t, \cdot)$ with $G(t, x) = \int_{-\infty}^x g(t, y) dy$ for all $x \in \mathbb{R}$. The prime example for $(B(t))_{t \geq 0}$ is Brownian motion, in which case g is the heat kernel $g(t, y) = \frac{1}{\sqrt{2\pi t}} e^{-y^2/(2t)}$, but our model allows for general stochastic processes $(B(t))_{t \geq 0}$. The primary tumor stays at the same location until it dies. We assume that the shedding time ν is exponentially distributed, $\nu \sim \text{Exp}(\mu)$ for some parameter $\mu \geq 0$, using the convention that $\nu = \infty$ if $\nu \sim \text{Exp}(0)$.

After an additional random time τ (namely, at time $\nu + \tau$), the cell cluster settles down. We assume that τ is exponentially distributed, $\tau \sim \text{Exp}(\lambda)$ for some parameter $\lambda \geq 0$. When the cell cluster has settled down, it will take

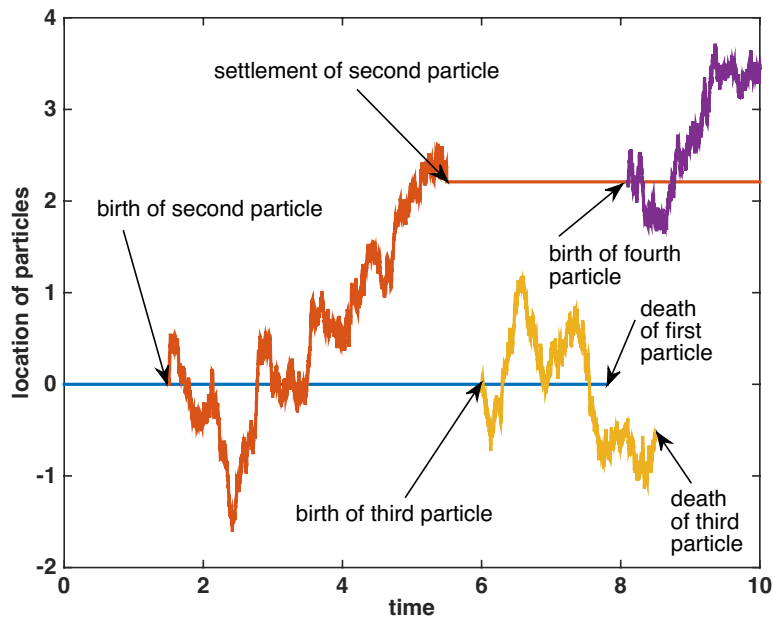


Figure 2.1: Illustration of a branching stochastic process with settlement. Taken from [50].

again a time which is exponentially distributed with parameter $\mu \geq 0$ until it emits another cell cluster. Also the first cell cluster will continue to emit further cell clusters after a time which is exponentially distributed with the same parameter $\mu \geq 0$, independently of the other random variables and processes. Cell clusters that are moving are destroyed at a rate $\delta_1 \geq 0$ while stationary clusters die at a rate $\delta_2 \geq 0$, again independently of the other clusters, the movement and the growth. The process is repeated ad infinitum. Figure 2.1 illustrates our model.

We now extend the notion from cell clusters to more general ‘particles’ since the branching stochastic process with settlement is also relevant to other applications such as seed dispersal, epidemic spread, and forest fire spread. In those cases, particles would refer to plant seeds, infectious agents, and burning branches, respectively. In this paper, our focus is on CTCs and metastatic dissemination.

We denote by $N(t)$ the number of particles born before time t . Their

positions at time t are $X_i(t)$ for $1 \leq i \leq N(t)$ where we enumerate the particles by their birthdates. For fixed t and i , $N(t)$ and $X_i(t)$ are random variables with values in \mathbb{N} and \mathbb{R} , respectively. We denote by $M(t)$ the number of particles alive at time t . We are interested in the following quantities:

- expected location $F(t, x) = E[\sum_{i=1}^{N(t)} \mathbb{1}_{X_i(t) \leq x}]$: the expected number of particles located in $(-\infty, x]$ at time t ,
- locational variance $V(t, x) = \text{Var}[\sum_{i=1}^{N(t)} \mathbb{1}_{X_i(t) \leq x}]$: the variation in the number of particles located in $(-\infty, x]$ at time t due to randomness,
- furthest particle distribution $H(t, x) = P[\max_{i=1, \dots, N(t)} X_i(t) \leq x]$: the probability that all particles are located in $(-\infty, x]$ at time t ,
- survival probability $Q(t) = P[M(t) > 0]$: the probability that there is at least one particle alive at time t ,

where we use the convention that $\mathbb{1}_{X_i(t) \leq x}$ is zero for all x and times t after the death time of particle i . We set $H(t, x) = 0$ for all x if no more particle exists at time t .

2.2 Summary of Analytical Results

First, we use the above branching stochastic process with settlement to find a common type of equation for the expected location F , the variance V , the distribution of the furthest particle H and the survival probability Q .

Theorem 1. *Consider the branching stochastic process with settlement defined*

above. The quantities F, V, H, Q satisfy

$$\begin{aligned} F_t(t, x) &= -\delta_2 F(t, x) + \mu e^{-(\lambda+\delta_1)t} G(t, x) \\ &\quad + \lambda \mu \int_0^t \int_{-\infty}^{\infty} F(t-u, x-z) g(u, z) e^{-(\lambda+\delta_1)u} dz du, \end{aligned} \quad (2.1)$$

$$\begin{aligned} V_t(t, x) &= -\delta_2 V(t, x) + \mu e^{-(\lambda+\delta_1)t} h(t, x) \\ &\quad + \lambda \mu \int_0^t \int_{-\infty}^{\infty} V(t-u, x-z) g(u, z) e^{-(\lambda+\delta_1)u} dz du, \end{aligned} \quad (2.2)$$

with

$$\begin{aligned} h(t, x) &= G(t, x) + e^{(\lambda+\delta_1)t} \frac{\delta_2}{\mu} F^2(t, x) \\ &\quad + \lambda \int_0^t \int_{-\infty}^{\infty} F^2(t-u, x-z) g(u, z) e^{(\lambda+\delta_1)(t-u)} dz du, \end{aligned}$$

$$\begin{aligned} H_t(t, x) &= [\mu e^{-\lambda t} (1 - e^{-\delta_1 t} (1 - G(t, x))) - (\mu + \delta_1)] H(t, x) \\ &\quad + \lambda \mu H(t, x) \int_0^t \int_{-\infty}^{\infty} H(t-u, x-z) g(u, z) e^{-\lambda u} dz du, \end{aligned} \quad (2.3)$$

$$\begin{aligned} Q'(t) &= -(\delta_2 + \mu e^{-(\lambda+\delta_1)t}) Q(t) + \mu e^{-(\lambda+\delta_1)t} \\ &\quad + \lambda \mu (1 - Q(t)) \int_0^t Q(t-s) e^{-(\lambda+\delta_1)s} ds. \end{aligned} \quad (2.4)$$

The proof of Theorem 1, and all subsequent results presented in this section, can be found in [50]. To better appreciate that the above equations (2.1)–(2.4) are all of the same form, we will introduce some notation. We encounter integral kernels that depend on one variable and on two variables. We use the same convolution symbol for both cases; given two kernels $k_1(t, x)$ and $k_2(t)$ and two test functions $f(t, x)$ and $g(t)$, we denote

$$\begin{aligned} k_1 * f(t, x) &:= \int_0^t \int_{-\infty}^{\infty} f(t-u, x-z) k(u, z) dz du \\ k_2 * g(t) &:= \int_0^t g(t-u) k(u) du. \end{aligned}$$

Case	r_1	r_2	$q(t, x)$	$p(t, x)$	$k(u, z)$
F	1	0	δ_2	$\mu e^{-(\lambda+\delta_1)t} G(t, x)$	$\lambda \mu e^{-(\lambda+\delta_1)u} g(u, z)$
V	1	0	δ_2	$\mu e^{-(\lambda+\delta_1)t} h(t, x)$	$\lambda \mu e^{-(\lambda+\delta_1)u} g(u, z)$
H	0	1	$q_H(t, x)$	0	$\lambda \mu e^{-\lambda u} g(u, z)$
Q	1	-1	$\delta_2 + \mu e^{-(\lambda+\delta_1)t}$	$\mu e^{-(\lambda+\delta_1)t}$	$\lambda e^{-(\lambda+\delta_1)u}$

Table 2.1: Parameter values for the different cases of expected location F , locational variance V , distribution of the furthest particle H and survival probability Q , using the abbreviation $q_H(t, x) = \mu + \delta_1 - \mu e^{-\lambda t} (1 - e^{-\delta_1 t} (1 - G(t, x)))$.

Then we combine equations (2.1)–(2.4) in the compact form

$$f_t = -qf + p + (r_1 + r_2 f) k * f, \quad (2.5)$$

where we identify parameters and functions as shown in Table 2.1.

For results concerning the general equation of the form 2.5, we require the following assumptions.

Assumptions (A1):

- We assume $r_1 \geq 0, r_2 \in \mathbb{R}$,
- $q(t, x) \geq \delta > 0$ is uniformly bounded and Lipschitz continuous in t and x .
- For each $T > 0$ $p(t, x) \geq 0$ is uniformly bounded on $[0, T]$ by P , absolute continuous in x and continuous in t .
- For the cases F, H, V : $k(u, z) \geq 0$ is continuous in x and satisfies for some constant $K > 0$ that

$$\int_0^t \int_{-\infty}^{\infty} k(u, z) dz du < K.$$

- For the case Q : $k(u) \geq 0$ satisfies for some constant $K > 0$ that

$$\int_0^t k(u) \, du < K.$$

- The initial condition $f_0(x) = f(0, x) \geq 0$ is bounded in $L^\infty(\mathbb{R})$.

To prove existence and uniqueness, we consider $T > 0$ and use as phase space

$$\mathcal{X} = L^\infty(0, T; \mathbb{R})$$

with the essential supremum norm $\|\cdot\|_\infty$. To find a mild formulation of (2.5), we define an integrating factor

$$W(t, s, x) = \exp\left(-\int_s^t q(u, x) \, du\right) \quad (2.6)$$

where the x -dependence arises only in the case of $f = H$. Since q is Lipschitz continuous and $q > 0$ we have that $W(t, s, x)$ is a non-negative evolution family with $0 < W(t, s, x) \leq 1$ for all $0 \leq s \leq t \leq T$. We use the variation of constant formula to formally solve (2.5) as

$$f(t, x) = f_0(x)W(t, 0, x) + \int_0^t W(t, s, x) \left[p(s, x) + (r_1 + r_2 f) k * f(s, x) \right] ds, \quad (2.7)$$

with $f(0, x) = f_0(x)$, which is our mild formulation.

Lemma 1. *Assume (A1) and let $f \in \mathcal{X}$ be a mild solution of (2.5).*

1. *Then $f(t, x) \geq 0$ as long as the solution exists.*
2. *If $f(t_0, x_0) = 0$ for a point (t_0, x_0) , then this implies that*

$$f_0(x_0) = 0 \quad \text{and} \quad p(t, x_0) = 0 \quad \text{for all} \quad 0 \leq t \leq t_0. \quad (2.8)$$

3. *If in addition $p(t, x) > 0$ for all $(t, x) \in (0, T) \times \mathbb{R}$ then $f(t, x) > 0$ for all $(t, x) \in (0, T) \times \mathbb{R}$.*

Proposition 1. *Assume (A1). Then there exists a time $T > 0$ and a unique mild solution $f \in \mathcal{X}$ which satisfies (2.7).*

Theorem 2. *The unique mild solutions from Proposition 1 exist for all times. The probabilities H and Q are globally bounded by 1 (as solutions of their corresponding integro-differential equation).*

Now we move on to the second set of results, those concerning the asymptotic model dynamics and the metastatic reproduction number. To introduce the metastatic reproduction number, R_0 , we reduce the above model by looking at the expected numbers of moving and stationary particles. We denote by $a(t)$ and $b(t)$ the expected numbers of moving and stationary particles, respectively. Moving particles die at rate δ_1 and become stationary at rate λ while new moving particles are born at rate μ from the stationary particles. This reasoning leads to

$$a'(t) = -(\delta_1 + \lambda)a(t) + \mu b(t). \quad (2.9)$$

Similarly, stationary particles die at rate δ_2 and moving particles become stationary at rate λ , leading to

$$b'(t) = -\delta_2 b(t) + \lambda a(t). \quad (2.10)$$

The differential equations for a and b form a linear system with coordinate matrix

$$A_1 = \begin{pmatrix} -(\delta_1 + \lambda) & \mu \\ \lambda & -\delta_2 \end{pmatrix}.$$

The matrix A_1 has trace and determinant as

$$\text{tr}A_1 = -(\delta_1 + \delta_2 + \lambda), \quad \det A_1 = \delta_2(\delta_1 + \lambda) - \lambda\mu.$$

The trace is negative, hence the origin is asymptotically stable for $\det A_1 > 0$ and unstable for $\det A_1 < 0$. Now, if we define

$$R_0 = \frac{\lambda}{\delta_1 + \lambda} \frac{\mu}{\delta_2},$$

we find the following result:

Lemma 2. *Consider (2.9), (2.10).*

- *If $R_0 < 1$ then $(0, 0)$ is globally asymptotically stable.*
- *If $R_0 > 1$ then $(0, 0)$ is unstable (it is a saddle).*
- *If $R_0 = 1$ then $(0, 0)$ is non-hyperbolic and we have a continuum of steady states in direction $(\delta_2, \lambda)^T$.*

It should be noted that $a(t) + b(t) = E[M(t)]$, where $E[M(t)]$ is the expected total number of particles.

Using specific initial conditions $(a(0), b(0)) = (0, 1)$ we can explicitly solve equations (2.9), (2.10) and we find the asymptotic ratio of moving versus stationary particles

$$\lim_{t \rightarrow \infty} \frac{a(t)}{b(t)} = \frac{\delta_2 - \delta_1 - \lambda + \sqrt{(\delta_2 - \delta_1 - \lambda)^2 + 4\lambda\mu}}{2\lambda}.$$

The importance of R_0 can also be seen in the dynamics of the survival probability, Q , which is a special case of (2.5), where there is no spatial variable. In this case, (2.5) becomes

$$Q'(t) = - \underbrace{\delta_2 Q(t)}_A + \underbrace{(1 - Q(t))\mu e^{-(\delta_1 + \lambda)t} \left(1 + \int_0^t Q(s)\lambda e^{(\delta_1 + \lambda)s} ds \right)}_B. \quad (2.11)$$

where

A: death rate of original particle times the survival probability at time t . Note that this is the only term if $\mu = 0$ (no births), in which case, the survival probability equals $Q(t) = \exp(-\delta_2 t)$.

B: correction term because the birth of particles leads to a higher survival probability than in the case $\mu = 0$. If the original particle has offsprings, all of the original particle, the offsprings of the original particle and further offsprings must die to extinct all particles, which is reflected in the term B.

Based on (2.11), we can derive a second-order ODE for Q , namely,

$$\begin{aligned} Q''(t) &= ((\delta_1 + \lambda)(Q(t) - 1) - Q'(t))\mu e^{-(\delta_1 + \lambda)t} \left(1 + \int_0^t Q(s)\lambda e^{(\delta_1 + \lambda)s} ds \right) \\ &\quad - \delta_2 Q'(t) + \mu\lambda Q(t)(1 - Q(t)) \\ &= \left(\frac{Q'(t)}{Q(t) - 1} - \delta_1 - \lambda \right) (Q'(t) + \delta_2 Q(t)) - \delta_2 Q'(t) + \mu\lambda Q(t)(1 - Q(t)) \end{aligned}$$

This equation can be transformed into a system of first-order ODEs as

$$\begin{aligned} Q' &= P, \\ P' &= \left(\frac{P}{Q - 1} - \delta_1 - \lambda \right) (P + \delta_2 Q) - \delta_2 P + \mu\lambda Q(1 - Q). \end{aligned} \tag{2.12}$$

We show the following result:

Lemma 3. *Consider system (2.12).*

- *If $R_0 < 1$ then $(0, 0)$ is locally asymptotically stable.*
- *If $R_0 > 1$ then $(0, 0)$ is locally unstable (it is a saddle).*

We can also obtain results for the asymptotic behavior of both the mean number of particles and the survival probability.

Theorem 3. *For $\mu \neq 0$, and $\lambda \neq 0$ or $\delta_1 \neq \delta_2$, the average number of particles alive at time t is given by*

$$E[M(t)] = \frac{\mu - \delta_2 - \alpha_-}{\alpha_+ - \alpha_-} e^{\alpha_+ t} + \frac{-\mu + \delta_2 + \alpha_+}{\alpha_+ - \alpha_-} e^{\alpha_- t},$$

where

$$\alpha_{\pm} = \frac{-\delta_2 - \delta_1 - \lambda \pm \sqrt{(\delta_2 + \delta_1 + \lambda)^2 + 4(R_0 - 1)\delta_2(\lambda + \delta_1)}}{2}. \tag{2.13}$$

For $\mu = 0$ or both $\lambda = 0$ and $\delta_1 = \delta_2$, the average number of particles at time t equals $E[M(t)] = (1 + \mu t)e^{-\delta_1 t}$.

Corollary 1. $E[M(t)]$ has the following asymptotic behavior: it ...

$$\left\{ \begin{array}{ll} \text{equals } (1 + \mu t)e^{-\delta_1 t} & \text{if } \mu = 0 \text{ or both } \lambda = 0 \text{ and } \delta_1 = \delta_2, \\ \text{grows exponentially at rate } \alpha_+ & \text{if } R_0 > 1 \text{ and not case 1,} \\ \text{converges to } \frac{1 + \lambda/\delta_2}{\delta_2/\mu + \lambda/\delta_2} & \text{if } R_0 = 1 \text{ and not case 1,} \\ \text{shrinks exponentially to 0 at rate } \alpha_+ & \text{if } R_0 < 1 \text{ and not case 1.} \end{array} \right.$$

Lemma 4. The asymptotic survival probability is

$$\lim_{t \rightarrow \infty} Q(t) = \begin{cases} \max\{1 - \frac{1}{R_0}, 0\} & \text{if } \mu > 0 \text{ and } \lambda > 0, \\ 1 & \text{if } \{\mu = 0 \text{ or } \lambda = 0\} \text{ and } \delta_2 = 0, \\ \frac{\mu}{\mu + \delta_2} & \text{if } \lambda = 0 \text{ and } \delta_1 = 0 \text{ and } \delta_2 > 0, \\ 0 & \text{otherwise.} \end{cases}$$

2.3 Application to Metastatic Cancer

In this section, we focus on my own contribution to [50]: application of the modeling framework developed above in the context of metastatic cancer. First, in Section 2.3.1, we provide a note on the numerical implementation of the Gillespie algorithm used to simulate the stochastic model. Following this, we present the results of our simulations for two separate scenarios. In Section 2.3.2 we apply the numerical framework to the case of metastatic spread *in-vivo*. In contrast, Section 2.3.3 sees the numerical framework applied to the case of experimental metastasis. Both Sections 2.3.2 and 2.3.3 include parameter fitting and the simulation results.

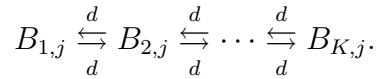
2.3.1 Gillespie Algorithm

In this section, we will provide a brief description of how the Gillespie algorithm was implemented to produce the simulations we report in the following sections. Full details of the general algorithm — including derivations and proofs — can be found in [54, 55]. Originally developed in the context of well-mixed chemical reactions, the Gillespie algorithm has been adapted

to spatially-dependent processes on finite spatial domains, such as reaction-diffusion equations [47]. The Gillespie algorithm is an exact stochastic simulation algorithm which uses adaptive timestepping as opposed to an equally spaced mesh grid. Therefore, at each timestep, two questions must be answered: first, how long until the *next* reaction occurs? And second, *which* reaction occurs? Below we provide our implementation, but the justification is found in the original Gillespie papers [54, 55].

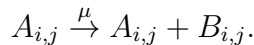
For our implementation, we must first gather some preliminaries. We consider a finite spatial domain centred around the origin, $[-L, L]$, which we divide into K equally spaced ‘bins’ of size h . Our model includes two ‘reactive species’: stationary particles and mobile particles. We denote by $A_{i,j}$ (and $B_{i,j}$) the number of stationary (and mobile) particles in spatial bin i at timestep j . At each timestep, j , any of five different types of reactions could occur:

1. A mobile particle could move between spatial bins at rate $d = D/h^2$, where D is the diffusion coefficient,



Note that there are a total of $2K - 2$ reactions described here.

2. A stationary particle in bin i could shed a mobile particle at rate μ ,



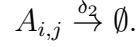
Note that there are a total of K such reactions.

3. A mobile particle could settle in bin i , creating a stationary particle at rate λ ,



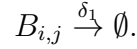
Note that there are a total of K such reactions.

4. A stationary particle in bin i could die at rate δ_2 ,



Note that there are a total of K such reactions.

5. A mobile particle in bin i could die at rate δ_1 ,



Note that there are a total of K such reactions.

Note that there are a total of $6K - 2$ possible reactions at each timestep. We will index all of the possible reactions with $\alpha = 1, 2, \dots, 6K - 2$. For each reaction, R_α , we define the *propensity* of R_α by the quantity

$$p_\alpha = h_\alpha c_\alpha,$$

where h_α is the number of reactants available for reaction R_α and c_α is the rate of reaction R_α . With this definition, we can now describe the algorithm beginning at timestep j :

1. Generate two random numbers, r_1 and r_2 , from the uniform distribution on the unit interval, $U(0, 1)$.
2. Determine the propensity of each reaction occurring at this time step.
 - Movement from bin i to $i + 1$ (or i to $i - 1$): $B_{i,j}d$
 - Shedding from bin i : $A_{i,j}\mu$
 - Establishment at bin i : $B_{i,j}\lambda$
 - Mobile death in bin i : $B_{i,j}\delta_2$
 - Stationary death in bin i : $A_{i,j}\delta_1$
3. Sum all these propensities to give the quantity

$$\alpha_0 = \sum_{\alpha=1}^{6K-2} p_\alpha.$$

4. Compute the time of the next reaction, $t + \tau$, via

$$\tau = \frac{1}{\alpha_0} \ln \left(\frac{1}{r_1} \right)$$

5. Determine *which* reaction occurs by finding the first index, $1 \leq \hat{\alpha} \leq 6K - 2$, such that

$$\frac{1}{\alpha_0} \sum_{\alpha=1}^{\hat{\alpha}-1} p_{\alpha} < r_2 \leq \frac{1}{\alpha_0} \sum_{\alpha=1}^{\hat{\alpha}} p_{\alpha}$$

6. Adjust the corresponding particle numbers,

- movement: $B_{i,j+1} = B_{i,j} - 1$ and $B_{i+1,j+1} = B_{i+1,j} + 1$ (similarly with $i - 1$)
- shedding: $B_{i,j+1} = B_{i,j} + 1$
- establishment: $B_{i,j+1} = B_{i,j} - 1$ and $A_{i,j+1} = A_{i,j} + 1$
- mobile death: $B_{i,j+1} = B_{i,j} - 1$
- stationary death: $A_{i,j+1} = A_{i,j} - 1$

7. Repeat for timestep $j + 1$.

We note that in our setup, with only a single stationary cell at the origin, the initial value of α_0 will be relatively small, resulting in a comparatively large timestep τ . However, as the simulation progresses, the number of particles in the system increases, and correspondingly, the value of α_0 will also increase, resulting in progressively smaller timesteps. Compared to ‘standard’ stochastic simulations — using an equally spaced grid for the entire simulation and first determining at each timestep *if* a reaction will even occur — this adaptive approach allows for accuracy over the course of the entire simulation without excessive precision at early times.

2.3.2 Application: Disease Spread

Because of the scarcity of quantitative data for metastatic cancer in humans, the majority of the values discussed below have come from experimental models of metastasis in mice. Many of the studies mentioned below follow a similar procedure (those in [15, 49, 97, 126] for example), and we provide a brief outline of their methods. Tumor-free mice are injected with radio-labeled cancer cells (B16 melanoma [49], M19 Fibrosarcoma [126], B16F1(0) melanoma [15, 97]), and observed and/or sacrificed at various time points ranging from 1 minute to 14 day post-injection. Organs of interest (multiple organs [49], lungs [15, 126], and liver [97]) are removed and analyzed for the number and location of cancer cells, cancer cell clusters, and metastases. In addition to the radio-labeled cancer cells, the Chambers group [15, 97] injected inert microspheres that become lodged within the microvasculature of the target organ in order to accurately determine the change in cell numbers over time. Details of specific experimental models can be found in the cited references.

In order to apply our model to the metastatic dissemination of cancer, we must first carefully define what is meant by ‘stationary’ and ‘mobile’ particles in this context. ‘Stationary’ particles will play the role of established tumors capable of shedding mobile particles without exhausting themselves. ‘Mobile particles’, therefore, will represent small clusters of individual cancer cells that are actively circulating through the vasculature. This interpretation necessitates different scales for the two classes of particles, with established tumors consisting of at least 10^8 cells—corresponding to a tumor volume of approximately 1cm^3 [29]—and CTCs consisting of anything between a single cell to several dozen [51]. Such a distinction requires careful attention when parameterizing the model. Below we discuss our approach to address this concern.

First we consider the shedding rate, μ . Assuming that an established tumor consists of 10^8 cells [29] and that the number of CTCs shed per day range between 0.0001% – 0.01% of the cells available within the established tumor [137], we may choose $\mu \in [100, 10000]$ cells per day. For the simulations presented herein, we chose $\mu = 346$ cells/day. This choice was made in order to

have an average of 10 established tumors by the end of 14 days [126] (determined using the asymptotic expected ratio of moving to stationary particles from the comment after Lemma 2).

Parameter	Description	Value	Units	References
μ	Shedding rate	346	cells/day	[29]; [137]
λ	Establishment rate	0.0035	tumors/day	[97]
δ_1	Mobile death rate	7	cells/day	[19]; [49]; [93]
δ_2	Stationary death rate	3.46×10^{-8}	tumors/day	[79]

Table 2.2: Model Parameters and the values used in presented simulations. The units can also be interpreted as simply ‘particles/day’, where it is understood that the meaning of ‘particles’ can be either an established tumor or a CTC. See text for further details.

Second, we estimate the stationary particle death rate, δ_2 . With the interpretation of a stationary particle as an established tumor, δ_2 corresponds to the rate of spontaneous tumor remission. We use Jessy’s estimate of $p = 10^{-5}$ [79] for the probability of spontaneous remission and assume that $p = \delta_2/\lambda$ to obtain the value of δ_2 reported in Table 2.2.

Third, we consider the rate of mobile particle settlement, λ . Experimental murine models of metastasis suggest that nearly 80% of the CTCs shed from the primary tumor into the vasculature will survive through the circulation and successfully extravasate at a secondary site [15, 97]. For the purposes of our model however, successful extravasation alone does not represent ‘settlement’. Indeed, because of the property that ‘settled’ particles are immediately capable of shedding mobile particles at the same rate as the original stationary particle, ‘settlement’ in our model includes not only successful extravasation at a secondary site, but survival and growth to a palpable secondary tumor as well. For this reason, we use the more suggestive terminology ‘establishment’ instead of ‘settlement’. Moreover, we assume that the establishment rate, λ , is related to the shedding rate, μ , via $\lambda = \mu q$ where q denotes the probability (per cell) of establishment. The probability q has been estimated by several investigators to range between 0.0001 and 0.00001 [19, 49, 97, 126]. In the results presented below, we have used the lower estimate of $q = 0.00001$ [97].

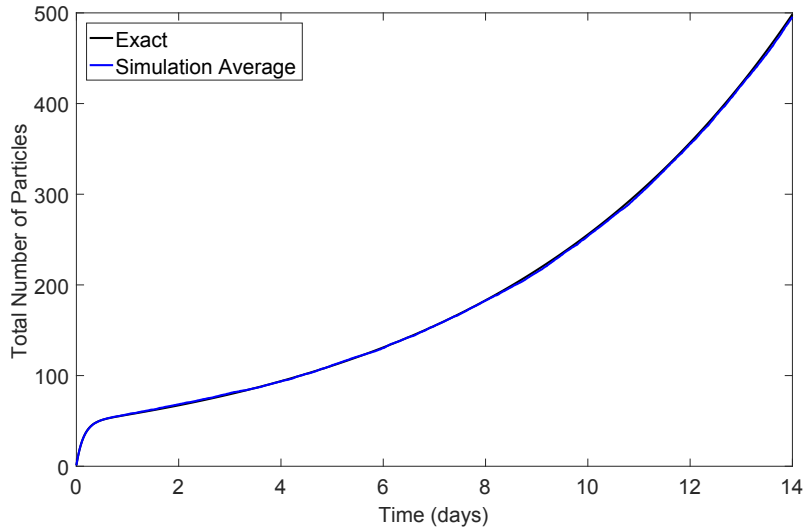


Figure 2.2: Total number of particles (stationary and mobile) as a function of time. Comparison of the theoretical expected value from Theorem 3 (black) and the average of 2250 realizations of the stochastic model (blue). Parameters as in Table 2.2. Taken from [50].

Finally, we require an estimate for the mobile particle death rate, δ_1 . While approximately 80% of cancer cells released into circulation will survive in the vasculature and successfully extravasate at a secondary location [15, 97], the fraction of these extravasated cells that will grow and form a metastasis is very small [15]. Consequently, our estimate for the mobile particle death rate must also include the death rate of successfully extravasated cells that do not become metastases, and will be much larger than if we included only deaths during transit. Additionally, the time that circulating cancer cells spend traveling through the circulation has been estimated to be between 1 and 3 hours [97, 126]. Therefore, assuming that ‘mobile particle’ means ‘CTC’, we expect these particles to be short-lived. Combining these observations, and based on previous results [19, 49, 93], we chose to have 99.9% of all the cells that are shed over the course of a day perish that day. Under this assumption, the mobile death rate becomes $\delta_1 = 7$ cells/day.

The implemented algorithm assumes a finite spatial domain, whereas the theoretical work presented in the previous sections does not. In order to simulate an infinite domain, we have chosen the finite domain to be sufficiently large so that there are no collisions between our mobile particles and the do-

main boundaries within the time of interest. For the simulations presented here (using diffusion coefficient of $D = 19\text{cm}^2/\text{day}$; see [126]), it was sufficient to consider the spatial domain $[-75\text{cm}, 75\text{cm}]$ divided into $K = 1500$ bins each of width 0.1cm . In Figures 2.2–2.4, we present the average results of 2250 distinct realizations of the stochastic model simulated over a period of 14 days. None of these realizations had particle-boundary collisions or complete disease extinction.

Theorem 3 provides an exact description of the expected number of particles as a function of time. We have therefore used this description to verify the accuracy of our numerical implementation of the model. Figure 2.2 shows a comparison between the exact dynamics from Theorem 3 (black curve) and the average dynamics over 2250 individual realizations of the stochastic model (blue curve). The average percent error over the 14 days simulated is 0.62%, with a maximum value of 1.86%.

While the simulations all begin with a single stationary particle, the expected number of particles increases to approximately 50 within the first day. This rapid increase is due to the relatively high shedding rate, resulting in the rapid creation of mobile particles. The slow-down upon reaching 50 particles reflects the expected asymptotic ratio of moving to stationary particles (comment after Lemma 2) which is approximately 48 with the parameters from Table 2.2. With the metastatic reproduction number $R_0 \approx 5.0 \times 10^6 \gg 1$, we expect the total particle number to grow exponentially at rate $\alpha_+ \approx 0.167$ (Corollary 1). After an initial period of transience, we do see exponential growth, both in the exact and simulated results.

Figure 2.3 illustrates the average spatio-temporal dynamics of the stochastic model. The left column presents the full spatio-temporal dynamics of the stationary (top) and mobile (bottom) particles, while the right column shows the spatial distribution of the stationary (top) and mobile (bottom) particles at time $t = 14$ days. In no individual simulation did we see the original established tumor perish. This result is not unexpected given the probability of a tumor perishing over the 14 days considered in our simulations is $1 - \exp(-14\delta_2) = 4.48 \times 10^{-7}$. Consequently, we always have at least one stationary particle located at position $x = 0$. This explains both the horizontal

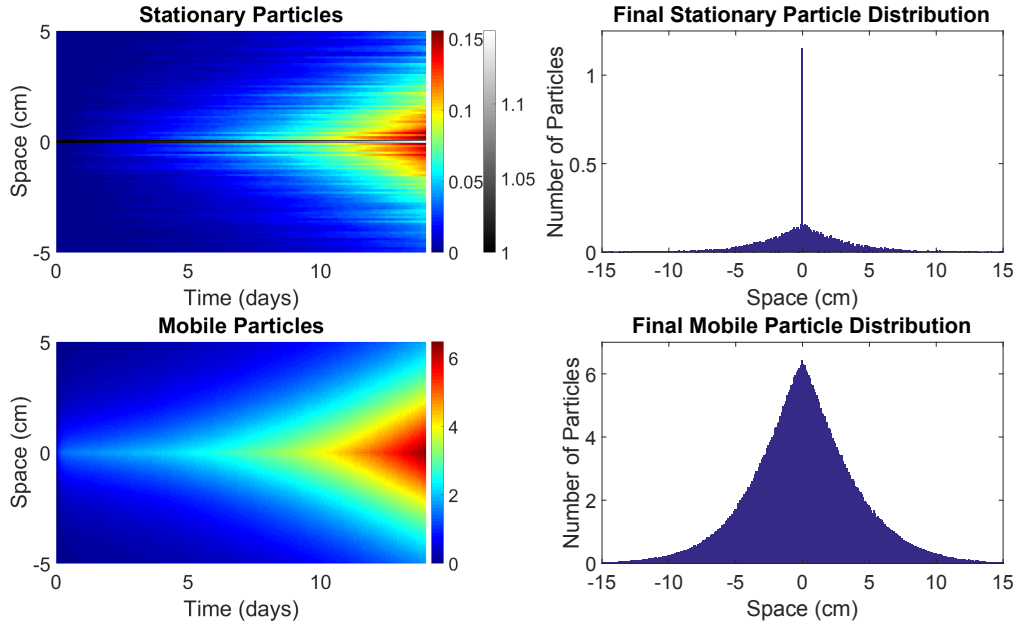


Figure 2.3: Average results of 2250 individual realizations of the stochastic model. Left column: spatio-temporal dynamics of the stationary (top) and mobile (bottom) particles. The horizontal axis is time (in days) while the vertical axis denotes space (in cm from location of primary tumor). Number of particles indicated by the coloring. Note the different scales in the top plot. Right column: average spatial distribution of the stationary (top) and mobile (bottom) particles at the end of the 14 day simulations. Note the difference in scales from top to bottom. Parameters used as in Table 2.2. Taken from [50].

line in the top left plot (note the difference in scales), as well as the tall bar at the origin in the top right plot. The histograms on the right side of Figure 2.3 show relatively symmetric distributions of both stationary and mobile particles centered around the origin. While the individual location of each particle is given by a normal distribution as a result of the Brownian dynamics, the distribution of the aggregate particles (both stationary and mobile) is not normal (see Figure 2.5). The reason is that shedding, settlement and death cause additional randomness. Even when $\lambda = 0$ (no settlement) and $\delta_1 = \delta_2 = 0$ (no deaths) so that only one stationary particle sheds moving particles, the distribution of the aggregate moving particles will not be normal. This can be seen from (2.1), which becomes $F_t = \mu G$, hence the density of the aggregate moving particles in this case is an integral of normal densities and not a normal

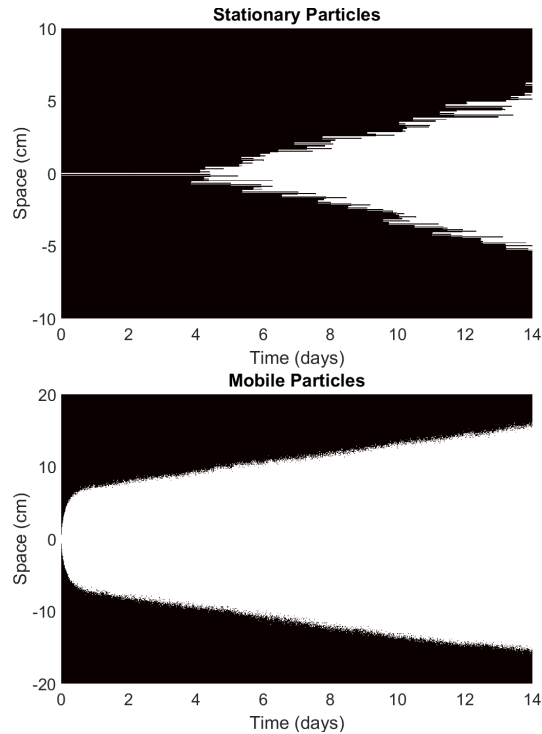


Figure 2.4: Manipulation of the plots from the left column of Figure 2.3 showing the areas that may be significantly affected by the primary tumor and its metastatic spread. More specifically, areas that have, on average, at least 0.025 particles over all 2250 simulations are colored white. Areas in which this is not the case are colored black. The top shows results for stationary particles, and the bottom for mobile particles. Taken from [50].

density itself.

In order to more clearly see the interface between empty space and invading cancer cells, we have taken the data in the left column of Figure 2.3, and simplified them to be either 1 if there was, on average, at least 0.025 particles in that location across all 2250 simulations, or 0 otherwise. The results of this simplification are presented in Figure 2.4. We can see that for stationary particles, it takes close to four days before we see any significant establishment events. This result closely mirrors the observations made by [15] and the results in [95, 93] that no metastases established in the first four days post-injection.

Following a rapid initial jump, the mobile particle boundary appears to invade at a more or less constant speed. These mobile ‘boundary’ dynamics

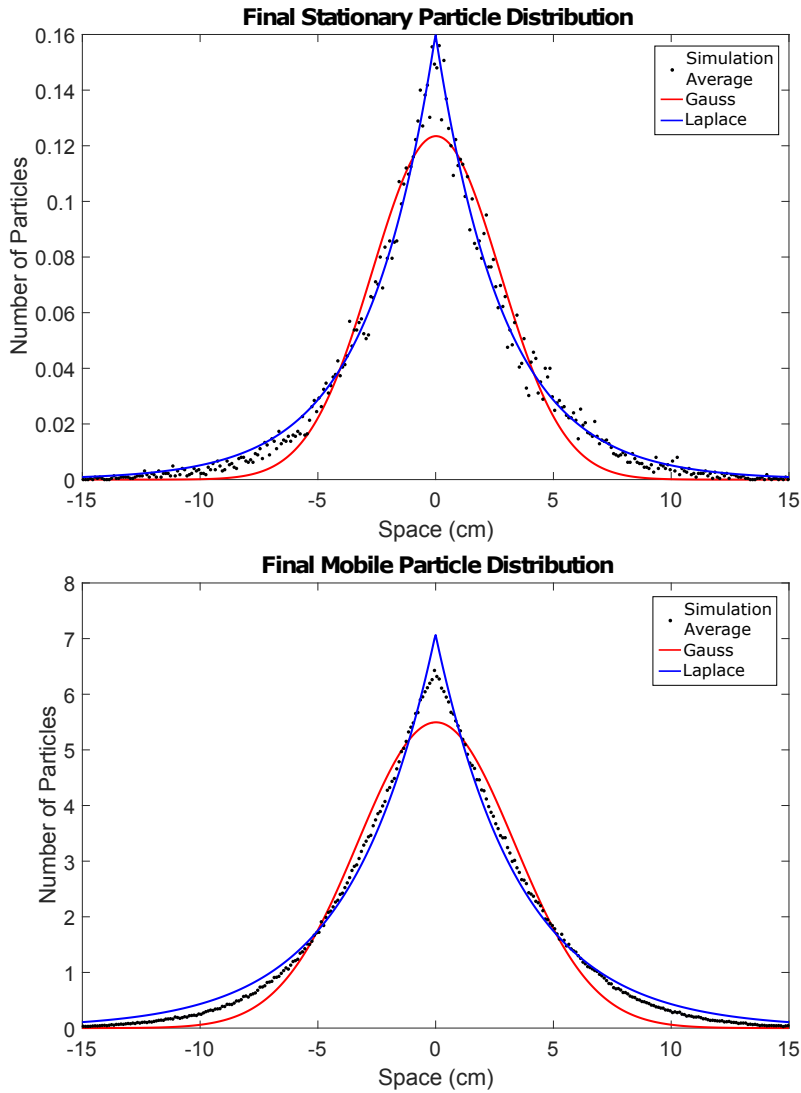


Figure 2.5: Gaussian and Laplacian fits to final time distributions of stationary particles (top) and mobile particles (bottom). We have subtracted 1 from the centre bin in the case of stationary particles for clarity of presentation.

(Figure 2.4) are in stark contrast with the ‘interior’ dynamics (bottom left in Figure 2.3, in particular, the blue-teal interface) where the level sets form triangular regions with edges whose slopes are increasing as we advance through time.

2.3.3 Application: Experimental Metastasis

The computational framework developed above can be readily modified to simulate the ‘experimental metastasis assays’ outlined in the previous section. Here we present new material which is not in [50] in which we compare our model simulation output to the data from Cameron et al. [15]. In what follows, we will describe the data used for our results, explain the modifications required from our previous description in order to accurately model the data, describe the process of parameter estimation, and present the simulation results.

In [15, 97], Chambers and collaborators develop a model of experimental metastasis designed to interrogate the efficiency of metastatic dissemination and establishment. We describe the work in [15] as it is what we use as comparison for our model, but similar techniques were performed in [97]. Mice were injected with a suspension of 2.5×10^5 fluorescently labeled cancer cells (B16F10 melanoma) and 5×10^4 *microspheres* (cells:microspheres = 5:1), and metastases were counted in the lungs. The microspheres were used in order to obtain an accurate count of the surviving cancer cells after the mouse was sacrificed. Because of their size and material the microspheres travel through the vasculature and become lodged permanently within the lung microvasculature. The known ratio cells:microspheres at the time of injection allows for accurate calculation of the percentage of injected cells that remain at later times. We compare our model to these particular results.

Parameter	Description	Value	Units	References
μ	Shedding rate	0	cells/day	
λ	Settlement rate	3.7	cells/day	[15, 97]
δ_1	Mobile death rate	0.9	cells/day	[15, 97]
δ_2	Stationary death rate	0.136	cells/day	[15, 97]

Table 2.3: Model Parameters and the values used in presented simulations.

It is clear from the experimental set up that we require a slightly different interpretation of the stochastic model components compared to the previous section. First, we assumed that a ‘stationary particle’ is a fully developed tu-

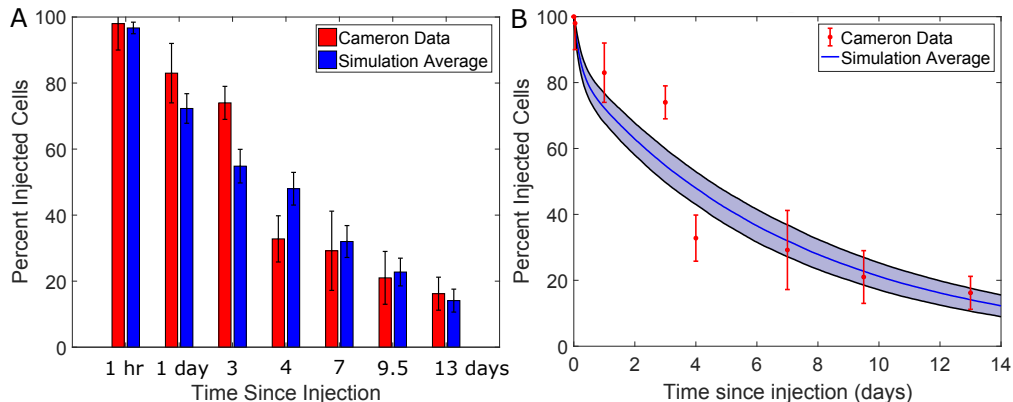


Figure 2.6: Comparison of Cameron data [15] (red) to model predictions averaged over 1000 simulations (blue). A: Percent injected cells remaining at discrete time points, chosen to compare with Figure 2 in [15]. Means and standard deviations presented. B: Continuous time predictions of the model compared to Cameron data. Blue line and shaded region denote mean and standard deviation respectively.

mor, capable of shedding individual/small clusters of cells without exhausting itself. In order to compare our model to the data from [15] we must change what we mean by ‘stationary particle’ to ‘individual cancer cells that have extravasated from the bloodstream’ instead. This forces different interpretations of the model parameters: λ is now a ‘settlement’ or ‘extravasation’ rate, and δ_2 is no longer a rate of spontaneous tumor remission, but the rate individual extravasated tumor cells perish. Further, with ‘stationary particles’ being nothing more than individual cells, a shedding event results in both an increase in mobile cells and a corresponding decrease in stationary cells. While this is certainly a possibility, we will assume that such events are sufficiently rare to be neglected (i.e. that $\mu = 0$). Second, instead of beginning with a single stationary cell — representing a primary tumor — we begin with a large number of mobile particles — representing the injection of cancer cells into the vascular system. This difference is easily accounted for in the simulation, but it does affect some of the arguments used to obtain the analytical results summarized in Section 2.2. Consequently, we only consider the output of the simulations against the Cameron data, and not against any ‘exact’ solutions.

Because of these new interpretations, we require new parameter estimates compared to the previous values given in Table 2.2. In [97], the authors re-

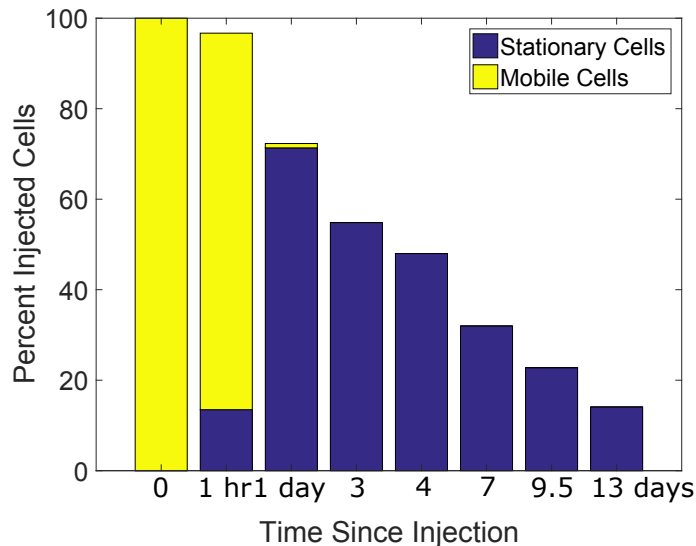


Figure 2.7: Mean percentage of remaining cells, averaged over 1000 simulations. Bars split into two cell populations: mobile cells (yellow) and stationary cells (blue).

port that the majority of injected cells remained in the vasculature at the 90 minute mark post-injection, but by 3 days post-injection the opposite was true. Similarly, Sindelar et al. [126] reported that the mean time spent circulating through the vasculature was around 3 hours. Based on these findings, we assume that 99% of the injected cells will have left the vasculature — via death within the bloodstream or extravasation into surrounding tissues — 1 day post-injection. Cameron’s data suggest that approximately 80% of the injected cells will successfully extravasate, while the remaining 20% died within the vasculature during transit. Combining these assumptions, we arrive at the estimates $\lambda = 3.7$ cells/day and $\delta_1 = 0.9$ cells/day. In order to estimate the death rate of ‘stationary’ cells, we determine the average loss rate between days 1 and 13 in the Cameron data [15], which gives us $\delta_2 = 0.136$ cells/day. These estimates are summarized in Table 2.3.

The plots in Figures 2.6 and 2.7 are the results of 1000 individual realizations of the stochastic model using the parameters reported in Table 2.3. Figure 2.6 A is a direct comparison to Figure 2 in [15], with the experimental data in red and the numerical data in blue. Means and standard deviations are presented for both data sets. We see reasonable agreement between the

biological and numerical experiments for most of the data points except for those reported on days 3 and 4. This discrepancy is better seen in Figure 2.6 B, which shows the continuous simulation results (mean \pm standard deviation) together with Cameron’s discrete data.

The results from the simulation can be split into two phases, characterized by the composition of the total population of cells (Figure 2.7). Initially, all the cells are mobile cells, which perish at a much higher rate than stationary cells (Table 2.3) resulting in an early, rapid decrease in cell number. However, within 1 day the vast majority of injected cells have extravasated from the blood stream (Figure 2.7). With this change in population composition, we see a corresponding decrease in the magnitude of the slope occurring around day 1 in Figure 2.6 B. Because our calibrated model is able to track the relative proportions of moving and stationary cells, we are able to confirm that our model can reproduce the dynamics observed between these two populations and allows us to conclude that an additional process not included in our model must be responsible for the drop observed in Figure 2.6.

2.4 Discussion

In this chapter we introduced a *branching stochastic process with settlement*, summarized a number of analytical results, and applied the model to metastatic cancer growth. From a probabilistic viewpoint, our model generalizes branching Brownian motion to arbitrary dynamics and the inclusion of settlement and death of particles. Branching Brownian motion has been analyzed for more than fifty years, starting with seminal work [76, 99] on the fundamental link between branching Brownian motion and the Fisher-Kolmogorov-Petrovsky-Piscounov equation. Since then branching Brownian motion has been intensively studied in its own right. In statistical mechanics, branching Brownian motion is used for models of spin glasses [13]. Recently, branching processes have been found useful in simulating semi-linear partial differential equations [70, 71]. To the best of our knowledge, these are the first results concerning branching processes with settlement and their applications in the context of

cancer metastasis.

The fact that the expected number F of particles, the variance V , the distribution H of the furthest particle and the extinction probability Q satisfy the same type of integro-differential equation with distributed delay (2.5) reveals the recursive structure of this process. Methods from differential equations theory become available to analyze the qualitative behavior of this stochastic process. A recurring quantity was identified to play the role of a basic reproductive number, similar to epidemic models [72], which we call the *metastatic reproductive number*

$$R_0 = \frac{\lambda}{\delta_1 + \lambda} \frac{\mu}{\delta_2}.$$

For the mouse data that we analyzed as an example, we found $R_0 \sim 10^6$, which, of course, is huge. This is expected, as cell lines for metastasis studies are chosen specifically to generate metastases efficiently and reliably.

The value of R_0 for a typical human cancer will be quite different, and we leave a detailed estimate of R_0 for human cancers for further studies. Still, we can already see the impact of various possible treatment strategies. To shrink R_0 , we like to reduce the shedding rate μ and the settlement rate λ while increasing the death rates δ_1 and δ_2 for moving and stationary particles, respectively. For example, the death rate δ_1 for CTCs could be increased through platelet inhibitors. Platelets are known to shield cancer cells from the immune surveillance, and less platelets can make cancer cells more exposed and more vulnerable [26, 119, 124]. The settlement rate λ might be reduced through decreasing the availability of metastatic niches [119]. This can be achieved through very simple means such as reduced pH-levels of tissue [125] to very advanced means such as novel immunotherapies designed to disrupt the preparation of the pre-metastatic niche [84]. However, removing 90% of cancer sites would not change the final outcome since the reproductive number is unchanged. A partial removal would significantly delay cancer spread, but metastasis would recur over time. Overall, the index R_0 has the potential to become a useful quantity in treatment planning.

While the population compositions from the simulations in Section 2.3.3

reasonably match those reported in the literature [15, 97, 126], the discrepancy observed in Figure 2.6 B may suggest there are additional factors contributing to the dynamics observed by Cameron than are accounted for in our model. Cameron suggests that this rapid drop in cell count between days 3 and 4 are a result of quiescent cells becoming active. The authors demonstrate that newly extravasated cells are quiescent — and therefore relatively *resistant* to cell death — and they appear to become active — and therefore relatively *sensitive* to cell death — around the time this large drop was observed. As we’ve noted before, the lack of growth dynamics in our model prevents us from confirming or denying this explanation, but we are able to note that *without* including the difference between quiescent and proliferating cells we were unable to accurately reproduce this sudden drop in cell numbers, suggesting that there is something else required in the model to capture these dynamics.

We see various extensions and limitations of the model as we discuss now.

1. In Sections 2.2 and 2.3.2 we started with a stationary individual, but in Section 2.3.3 we started with mobile particles. While this was easy to simulate, the analysis of the system beginning with mobile particles would be more difficult. Furthermore, if we know the function F of our model, we can find the corresponding function \tilde{F} in a model with randomly moving first particle by

$$\begin{aligned}
\tilde{F}(t, x) &= E \left[\sum_{i=1}^{N(t-\min\{\tau, t\})} \mathbb{1}_{X_i(t-\min\{\tau, t\})+B(\min\{\tau, t\}) \leq x} \right] \\
&= \int_0^t E \left[\sum_{i=1}^{N(t-s)} \mathbb{1}_{X_i(t-s)+B(s) \leq x} \right] \lambda e^{-\lambda s} e^{-\delta_1 s} ds + \int_t^\infty P[B(t) \leq x] \lambda e^{-\lambda s} e^{-\delta_1 t} ds \\
&= \int_0^t \int_{-\infty}^\infty F(t-s, x-y) g(s, y) \lambda e^{-(\lambda+\delta_1)s} dy ds + G(t, x) e^{-(\lambda+\delta_1)t},
\end{aligned}$$

where $B(\min\{\tau, \cdot\})$ is a random process describing the movement of the first particle up to time τ , and the factor $e^{-\delta_1 s}$ is the survival probability of the first particle at time s .

2. In order to circumvent the issues with ‘scale’ discussed in Section 2.3.2,

and the poor fit to the data from days 3 and 4 in Section 2.3.3, additional elements may need to be incorporated into the model. In particular, the inclusion of growth dynamics of stationary cells would be of particular value. Indeed, accounting for the growth of settled cells would allow us to avoid the need for distinguishing between particles as ‘cells’ and as ‘tumors’. Additionally, including ‘proliferating’ and ‘quiescent’ cells may be sufficient to capture the precipitous drop in cell count observed in Figure 2.6. This addition is left as future research.

3. The spatial transport and settlement of a real cancer in a human body is much more complicated than assumed in our example. Here, as an example, we considered Brownian motion as spatial process and a homogeneous settlement rate, λ . However, our framework is based on a general spatial process, $(B(t))_{t \geq 0}$, whose distribution could reflect more realistic body-wide properties. Such a specification is a complex issue and left for future research.
4. It is well known that certain tumors tend to metastasize to certain organs, for example prostate cancer preferentially metastasizes to the bone, and breast tumors often spread to the brain, bone, liver, and lungs [19]. In this case, the settlement rate, λ , is no longer homogenous, rather it depends on the location x . Moreover, this spatial dependency encodes the locations of pre-metastatic niches [84]. However, the branching stochastic process with settlement would then lose its recursive nature, which was crucial in the proofs of our results. Consequently, additional work must be completed before this intricacy can be included into future iterations of the model.

Chapter 3

A Deterministic Model for Cancer Metastasis: Two Sites

In this chapter we investigate the implications of the *immune-mediated* theory of metastasis (see Section 1.1.2) using an ODE model of cancer-immune dynamics at two anatomically distant sites. In Section 3.1 a brief summary of tumor-immune modeling is provided before developing our model. The steady states of the model and conditions necessary for disease extinction are determined in Section 3.2. We discuss the process of parameterizing the model in Section 3.3 with numerical results presented in Section 3.4, including simulations of treatments. Model simulations suggest that the presence of a pro-tumor immune population can not only limit the effectiveness of immunotherapies, but potentially render such therapies harmful. It is also shown that an injury at a distant site can inhibit or promote the growth of a metastatic tumor at that site, depending on timing of the injury relative to disease progression. We conclude this chapter with a discussion of the results and their implications in Section 3.5.

3.1 The Model

In order to provide context for our model, this section begins by highlighting a number of models from the literature used to investigate the interplay between

tumor and immune cells. We then develop our model in addition to introducing the functional coefficients chosen for the numerical simulations presented in Section 3.4.

A review of the current questions, models, and methods being used to investigate the dynamics of tumor-immune interactions are presented in [43, 44]. In what follows we describe only those approaches that are directly relevant to our model, with interested readers referred to the reviews [43, 44] for further discussion. A key model of tumor-immune dynamics is the model of Kuznetsov [91]. In 1994, Kuznetsov proposed an ODE model of tumor-immune reactions including tumor cells and effector immune cells, which was analyzed and effectively applied to experimental data [91]. It was found that this simple model could accurately describe observed dynamics including oscillations in tumor size, reminiscent of spontaneous remission and relapse in leukemia cell lines, and tumor escape from immune surveillance after growing sufficiently large. A subsequent paper [90] saw the addition of a second tumor cell type whose dynamics were not influenced by the effector immune cells. Due to its simplicity and its success in accurately describing observed tumor-immune dynamics, Kuznetsov's model has been adapted and included in several other models of tumor-immune interactions, including the work of the Enderling group [115, 116, 135, 134] and the current thesis.

While there are models developed that include both anti- and pro-tumor immune effects ([34] and [138] for example), such approaches are relatively new, with the vast majority of the research considering only the cytotoxic effect of immune cells. For instance, de Pillis [28] has been actively researching tumor-immune dynamics mathematically for years, with a particular focus on the development of effective therapies through the use of optimal control theory. In de Pillis [28], a 4 compartment ODE model — including equations for tumor cells, effector immune cells, circulating lymphocytes, and a chemotherapeutic agent — is considered. The purpose of including a circulating lymphocyte population is to provide some realistic restraints on the optimal control problem, viewing this population as an indicator of patient health. Without the chemotherapeutic agent, the basic Kuznetsov model is recovered. Similarly, the 5 compartment ODE model for cancer immuno-therapy presented in

[16] is an extension of the original Kuznetsov model, with only cytotoxic CD8 T cells playing any direct role on the tumor population. In both [28] and [16], the contradictory effects of the immune response to cancer (as highlighted in Section 1.1.2) are neglected.

Our goal with this chapter is to develop a model of tumor-immune interactions that accounts for the contradictory roles of the immune system not only on the development of a primary tumor, but on the dynamics of metastatic dissemination as well. To begin, we assume that there are two sites of interest: a *primary site*, where the initial tumor is located, and a *secondary site*, where a metastasis will develop. In our model, we include only a single secondary ‘site’, but this could also be interpreted as total metastatic burden assuming homogeneity between the sites and choosing an appropriate growth function. In the current work, however, we assume simply that the secondary site is a single location where a single metastatic tumor establishes. While we consider only two sites, our framework could easily be extended to multiple sites with careful modeling of the flow between the sites, using an approach similar to the Enderling group [115] using network modeling as in [85].

At both the primary site and the secondary site ($i = 1$ and 2 , respectively), we model the behavior of 4 different quantities: the number of tumor cells, $u_i(t)$, the number of necrotic cells, $v_i(t)$, the number of cytotoxic (CT) immune cells, $x_i(t)$, and the number of *tumor-educated* (TE) immune cells, $y_i(t)$. A cartoon version of the model is presented in Figure 3.1. Because we are interested in modeling metastatic spread, we assume that the ‘tumor cells’ described by u_i are tumorigenic and therefore capable of establishing a secondary tumor in ideal conditions. Another way of describing the population of cells in u_i could be as CSCs or as cells with the ‘metastatic phenotype’. While the identity of the cells capable of metastasizing is still an active area of research (see Section 1.2.1 for example), herein we assume that a fraction of the cells within the tumor can metastasize. We now detail the specific assumptions for each of the quantities described above.

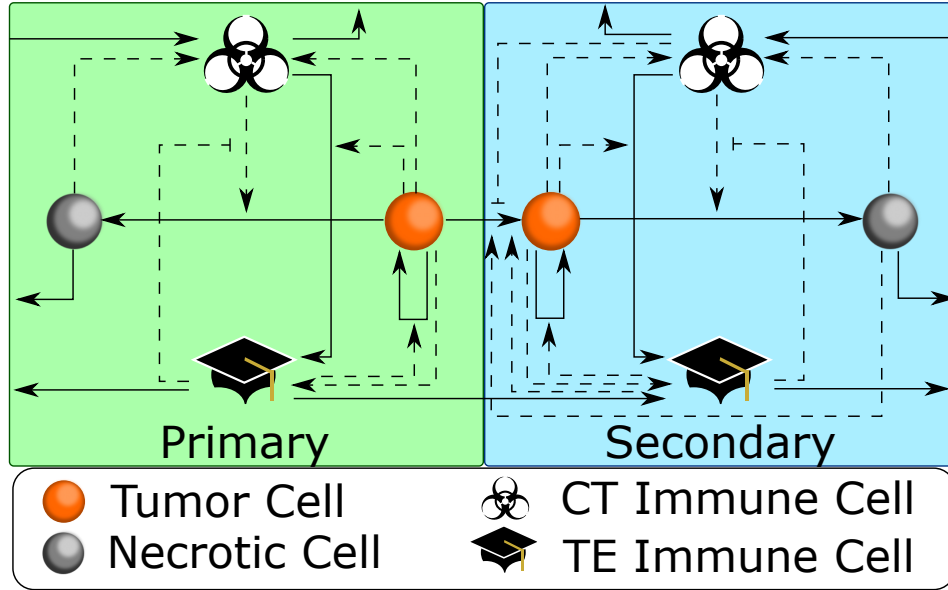


Figure 3.1: Cartoon model of the 8 ODE model of metastasis (3.6). Arrows indicate *positive* effects, and flat ends indicate *inhibitory* effects. Solid lines represent *direct* effects and dashed lines denote *indirect* influence. See text for details.

Tumor Cells

At both the primary and secondary sites we include immune-influenced birth-death dynamics, together with shedding from the primary site and establishment of shed cells at the secondary site. Both sites include an intrinsic growth function, $g_{1,2}$, which is a decreasing function of the tumor population, $u_{1,2}$. Tumor growth can be supported by the activity of TE immune cells which can supply the local microenvironment with growth and pro-angiogenic factors (Section 1.1.1). We model the TE immune cell enhancement of tumor growth with ‘*enhancement*’ functions, $\gamma_{1,2}(y_{1,2})$, which we assume are increasing functions in $y_{1,2}$. Under the assumption that tumors grow at their intrinsic growth rates without any growth *enhancement* in the absence of TE immune cells (i.e. $y_{1,2} = 0$), we fix $\gamma_{1,2}(0) = 1$. We assume further that the functions $\gamma_{1,2}(y_{1,2})$ are bounded in their arguments, corresponding to the assumption that the *enhancement* effect of TE immune cells on tumor growth rate saturates.

Also included is immune-influenced tumor cell death at both sites. Tu-

mor cell death *increases* as a function of the CT immune cell population and *decreases* as a result of the protective effects of TE immune cells (which can act as immunosuppressive Tregs, for example). Therefore, we assume that the tumor cell death rates, $\sigma_{1,2}(x_{1,2}, y_{1,2})$, are *increasing* in CT immune cells, $x_{1,2}$, and *decreasing* in TE immune cells, $y_{1,2}$. As in the case of tumor growth rates, we assume that the death rates are bounded both above and below for non-negative arguments.

Finally, terms are included for shedding of circulating tumor cells (CTCs) by the primary tumor and arrival of CTCs to the secondary site. We first note that the effects of metastatic ‘re-seeding’ are not included. That is, we assume that the secondary tumor does not shed cells that could travel to the primary site. Inclusion of such effects in models of metastasis have been done before [67] with little effect on the model outcomes, thereby justifying our modeling choice to neglect the effects of ‘re-seeding’. In line with other models of metastasis [62], we assume that shedding of CTCs is proportional to the primary tumor size and occurs at a constant rate, $s_1 > 0$. Combining the above assumptions we arrive at the equation governing the primary tumor dynamics,

$$\frac{du_1}{dt} = \underbrace{\gamma_1(y_1)g_1(u_1)u_1}_{\text{growth}} - \underbrace{\sigma_1(x_1, y_1)u_1}_{\text{death}} - \underbrace{s_1u_1}_{\text{shedding}} . \quad (3.1)$$

To complete the description of tumor dynamics at the secondary site, we must model the establishment of CTCs at that location. In order to investigate the implications of the theory of immune-mediated metastasis [124], it is assumed that secondary establishment depends on CT and TE immune cells and the number of necrotic cells present at the secondary location. Denote by $est(v_2, x_2, y_2)$ the establishment rate at the secondary site. Much like in the case of the tumor cell death rates discussed above, we assume that $est(v_2, x_2, y_2)$ is *decreasing* in the CT immune population at the secondary site, x_2 , and *increasing* in the TE immune population at the secondary site, y_2 . Shahriyari hypothesizes that the presence of an injury or wound at a distant site can act as a supportive PMN for CTCs [124]. Therefore, we assume that $est(v_2, x_2, y_2)$ is an *increasing* function of the necrotic cells at the sec-

ondary site, v_2 . In the absence of necrotic cells, we assume a small, positive establishment rate to reflect the fact that not all metastases occur as a result of the process outlined by the immune-mediated theory of metastasis. It is also assumed that the effect of necrotic cells on the establishment rate saturates. Implicitly included in this formulation is the proportion of shed cells, $s_1 u_1$, that successfully extravasate at the secondary site and begin to proliferate, so we require $0 \leq est(v_2, x_2, y_2) \leq 1$. Combining all of the above observations and assumptions leads us to the following equation for the tumor cell dynamics at the secondary site:

$$\frac{du_2}{dt} = \underbrace{\gamma_2(y_2)g_2(u_2)u_2}_{\text{growth}} - \underbrace{\sigma_2(x_2, y_2)u_2}_{\text{death}} + \underbrace{est(v_2, y_2, x_2)s_1 u_1}_{\text{establishment}}. \quad (3.2)$$

Necrotic Cells

Necrotic cells arise at site $i = 1, 2$ as a result of tumor cells perishing at the rate $\sigma_i(x_i, y_i)$, and are cleared away by cell lysis at the rate μ_i . As mentioned previously, we assume that the population of tumor cells included in the quantities u_i consists of the fraction of the total tumor population that is tumorigenic, and thus capable of successfully seeding secondary metastases. However, all cells within the total tumor population — tumorigenic or not — are capable of perishing and contributing to the population of necrotic cells. Therefore, we include a scaling constant, $\theta_{1,2} \geq 1$, to account for this modeling assumption. The equations governing the dynamics of the necrotic cell population are given by

$$\frac{dv_i}{dt} = \underbrace{\theta_i \sigma_i(x_i, y_i) u_i}_{\text{dying cells}} - \underbrace{\mu_i v_i}_{\text{lysis}}, \quad (3.3)$$

with $i = 1, 2$.

CT Immune Cells

The skeleton of the equations for the CT immune cell populations (dynamics are assumed the same at both sites) is borrowed from Kuznetsov [90, 91] with a few key additions. As in the Kuznetsov model, we include a natural influx rate,

α_i , a decay term where decay occurs at rate ω_i , and a loss term corresponding to fatal interactions with the tumor cells, occurring at rate ρ_i . Kuznetsov's model included a term to account for tumor-mediated expansion of the CT immune population, but we modify this term to also include immune recruitment due to necrotic cells. We assume that CT immune recruitment occurs at rate $\lambda_i(u_i, v_i)$, where λ_i is an increasing function in each of its arguments, and is bounded above and below for non-negative arguments. Finally, we assume that a tumor can 'educate' a CT immune cell, causing a phenotypic change and resulting in an immunosuppressive TE immune cell [107, 124]. While the exact mechanism responsible for this phenotypic plasticity is unknown, it will be assumed that the 'education' rate of CT immune cells by tumor cells is an increasing function of the tumor size, $ed_i(u_i)$, with the property that $ed_i(0) = 0$. Summarizing the above, we arrive at the following equations governing the CT immune cell populations at sites $i = 1, 2$:

$$\frac{dx_i}{dt} = \underbrace{\alpha_i}_{\text{natural influx}} + \underbrace{\lambda_i(u_i, v_i)x_i}_{\text{growth}} - \underbrace{\rho_i u_i x_i}_{\text{interaction with tumor}} - \underbrace{\omega_i x_i}_{\text{natural death rate}} - \underbrace{ed_i(u_i)x_i}_{\text{tumor education}} . \quad (3.4)$$

TE Immune Cells

Finally, the dynamics of the TE immune cells are considered. We first describe the TE immune dynamics at the primary site. In the absence of a primary tumor, no tumor *education* can occur therefore there will be no TE immune cells. Once a tumor establishes at the primary site, however, *education* of CT immune cells can occur. With the first 'graduating class' and the development of a positive TE immune cell population at the primary site, the TE immune population can grow further under the influence of the primary tumor at rate $f_1(u_1)$ — which we take to be a bounded, increasing function of primary tumor size u_1 . The TE immune population can also shrink due to natural death, at rate τ_1 , and shedding from the primary site into the surrounding vasculature, at rate \tilde{s}_1 . A fraction, p , of these disseminated TE immune cells will arrive at the secondary site, allowing for the development of a TE immune population at the secondary site, even in the absence of a secondary tumor. Once

a secondary tumor has established, we assume dynamics similar to the primary site, including tumor education, tumor-mediated expansion, and natural death. The TE immune cell dynamics are captured in the equations

$$\begin{aligned}
\frac{dy_1}{dt} &= \underbrace{ed_1(u_1)x_1}_{\text{tumor education}} - \underbrace{\tau_1 y_1}_{\text{death}} - \underbrace{\tilde{s}_1 y_1}_{\text{shedding}} + \underbrace{f_1(u_1)y_1}_{\text{tumor mediated expansion}}, \\
\frac{dy_2}{dt} &= \underbrace{ed_2(u_2)x_2}_{\text{tumor education}} - \underbrace{\tau_2 y_2}_{\text{death}} + \underbrace{p\tilde{s}_1 y_1}_{\text{arrival}} + \underbrace{f_2(u_2)y_2}_{\text{tumor mediated expansion}}.
\end{aligned} \tag{3.5}$$

The Full Model

For clarity of presentation we now summarize the previous discussions by displaying the full two-site, 8 equation model for immune-mediated metastasis. Notational details and model assumptions can be found in the text above. Functional coefficients used for numerical simulations presented in the following sections are discussed below.

$$\begin{aligned}
\frac{du_1}{dt} &= \gamma_1(y_1)g_1(u_1)u_1 - \sigma_1(x_1, y_1)u_1 - s_1 u_1 \\
\frac{dv_1}{dt} &= \theta_1 \sigma_1(x_1, y_1)u_1 - \mu_1 v_1 \\
\frac{dx_1}{dt} &= \alpha_1 + \lambda_1(u_1, v_1)x_1 - \rho_1 u_1 x_1 - \omega_1 x_1 - ed_1(u_1)x_1 \\
\frac{dy_1}{dt} &= ed_1(u_1)x_1 - \tau_1 y_1 - \tilde{s}_1 y_1 + f_1(u_1)y_1 \\
\frac{du_2}{dt} &= \gamma_2(y_2)g_2(u_2)u_2 - \sigma_2(x_2, y_2)u_2 + est(v_2, y_2, x_2)s_1 u_1 \\
\frac{dv_2}{dt} &= \theta_2 \sigma_2(x_2, y_2)u_2 - \mu_2 v_2 \\
\frac{dx_2}{dt} &= \alpha_2 + \lambda_2(u_2, v_2)x_2 - \rho_2 u_2 x_2 - \omega_2 x_2 - ed_2(u_2)x_2 \\
\frac{dy_2}{dt} &= ed_2(u_2)x_2 - \tau_2 y_2 + p\tilde{s}_1 y_1 + f_2(u_2)y_2
\end{aligned} \tag{3.6}$$

Functional Coefficients

While the framework we developed above is highly general and assumes very little on the functional coefficients used, specific choices must be made in

order to perform numerical simulations. Here we highlight the choices made to obtain the plots presented below. For simplicity, the same functional forms are used at both the primary and secondary sites, even if this may not be the most accurate choice [67].

Tumor growth is assumed logistic,

$$g_i(u_i) = r_i \left(1 - \frac{u_i}{K_i} \right),$$

with intrinsic growth rate r_i and carrying capacity K_i , $i = 1, 2$. This assumption has been made by several other investigators [91, 115] because of its simplicity and relative success at capturing observed dynamics. It has been shown to be a reasonable model for the growth of a *primary* tumor, but it does not perform as well as a model of *secondary* tumor growth [67].

Tumor-mediated expansion of the immune cell populations is modeled using Michaelis-Menten type equations with exponent 1 [91, 115]. For completeness, we list the functions used below:

$$\begin{aligned} \lambda_i(u_i, v_i) &= \left(\frac{a_{1i}u_i}{b_{1i} + u_i} \right) + \left(\frac{a_{2i}v_i}{b_{2i} + v_i} \right) \\ f_i(u_i) &= \frac{ht_i u_i}{hb_i + u_i}. \end{aligned} \tag{3.7}$$

We note that for the λ_i expression, even if one of either the tumor cell or necrotic cell population has gone extinct, there is still CT immune recruitment to the tumor environment given one of the populations is non zero.

Following the work of den Breems and Eftimie [34], we assume the *education* of CT immune cells by tumor cells follows the law of mass action at both tumor sites,

$$ed_i(u_i) = \chi_i u_i.$$

While the process of immune *education* is most likely much more intricate than a simple mass action interaction term, the dynamics of this sub-process are not the focus of this work and without any strong evidence supporting another functional form, we have chosen the simplicity of mass action.

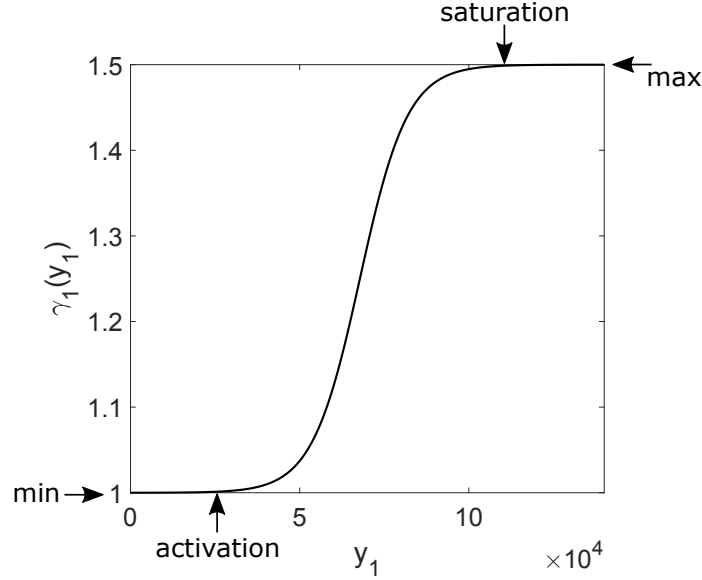


Figure 3.2: tanh threshold function. With parameters from Table 3.1.

For many of the other *saturating* functions, we borrow the *tanh* switch-like functions used in [108] because of their simple interpretation. The functions include 4 parameters — a lower bound (m), an upper bound ($m+M$), an *activation* threshold (A), and a *saturation* threshold (S). The role of each of these parameters is outlined in Figure 3.2. We include two variants of the function: one *increasing* in its argument (x),

$$\nu(x; m, M, A, S) = \frac{M}{2} \left[\tanh \left(\frac{6}{S-A} \left(x - \frac{S+A}{2} \right) \right) - \tanh \left(\frac{-3(S+A)}{S-A} \right) \right] + m \quad (3.8)$$

which increases from m when $x = 0$ to $m + M$ as $x \rightarrow \infty$, and one *decreasing* in its argument,

$$\xi(x; m, M, A, S) = \frac{M \left(1 - \tanh \left(\frac{6}{S-A} \left(x - \frac{S+A}{2} \right) \right) \right) + m \left(\tanh \left(\frac{6}{S-A} \left(x - \frac{S+A}{2} \right) \right) - \tanh \left(\frac{-3(S+A)}{S-A} \right) \right)}{1 - \tanh \left(\frac{-3(S+A)}{S-A} \right)} \quad (3.9)$$

which decreases from M when $x = 0$ to m as $x \rightarrow \infty$.

The tumor cell death rate functions, $\sigma_{1,2}$, are increasing in CT immune cell population, $x_{1,2}$, and decreasing in the TE immune cell population, $y_{1,2}$. In the presented simulations, we have used

$$\sigma_i(x_i, y_i) = \xi(y_i; 0, 1, upD_i, lowD_i)\nu(x_i; minC_i, maxC_i, upC_i, lowC_i)$$

for $i = 1, 2$.

For the TE immune cell enhancement of tumor growth, $\gamma_{1,2}(u_{1,2})$, similar threshold dynamics are assumed: little to no enhancement for TE immune populations *below* a certain threshold, rapid increase to saturation at levels *above* another threshold, as above. Following the assumptions made on γ_i in the previous sections, we choose

$$\gamma_i(u_i) = \nu(u_i; 1, max_i, low_i, up_i). \quad (3.10)$$

Finally, we must determine a functional expression for the establishment rate of CTCs at the secondary site, $est(v_2, x_2, y_2)$. Again, we will assume threshold dynamics, this time in all three of the arguments. We also note that the incidence of spontaneous malignancy in immune-deficient settings is 100–1000 times the incidence in immune-competent settings [56]. Therefore, a constant, MER , is included to account for these observations. The functional form used for the establishment rate in the simulations presented below is

$$\begin{aligned} est(v_2, x_2, y_2) = & \nu(v_2; minV, maxV, lowV, upV) \\ & \times \xi(x_2; 0, MER, lowDest, upDest) \\ & \times \nu(y_2; minEst, maxEst, lowEst, upEst). \end{aligned} \quad (3.11)$$

The time-dynamics of this establishment function for the parameters in Table 3.1 are presented in Figure 3.3. In region 1, the high level of CT immune cells at the secondary site provides a strong defence against metastatic establishment. However, as the CT immune population decreases, being replaced with TE immune cells, the rate of metastatic establishment jumps significantly. This is in line with the data from [56] mentioned above. As the number of

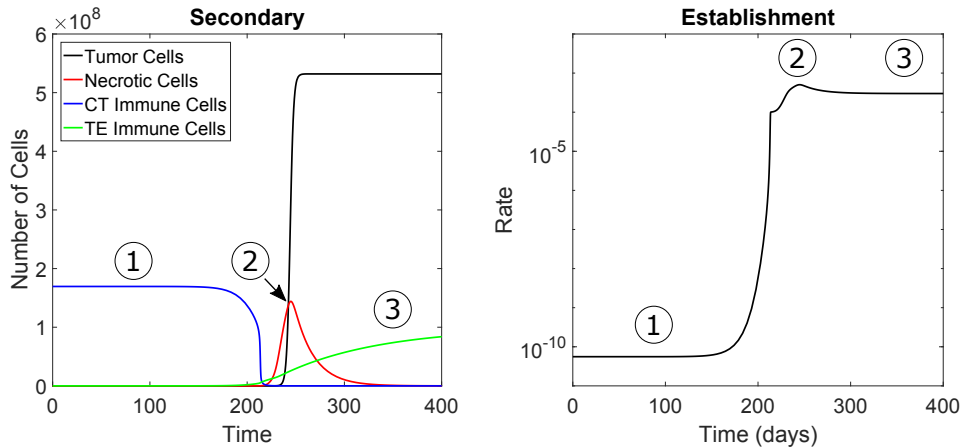


Figure 3.3: Left: Secondary site dynamics with parameters in Table 3.1. Right: The establishment rate at the secondary site as a function of time using the solutions from the left plot. Region (1) is characterized by a strong population of CT immune cells, resulting in a low rate of establishment. As the CT immune cell population falls around $t = 200$, so does the establishment rate. A peak of necrotic cells occurs at time (2), in which we can see a corresponding peak in the establishment rate. Finally, in region (3), the CT immune cells have been ‘replaced’ with TE immune cells, and we see a much higher rate of establishment.

necrotic cells at the secondary site peaks in region 2, we see a corresponding peak in the establishment rate. Finally, the higher level of TE immune cells in region 3 explains the corresponding plateau in the establishment rate.

We have now introduced the full model as presented in the simulations in Section 3.4. Parameter values used for the simulations can be found in Table 3.1. A discussion of the quality of these choices is presented in Section 3.5.

3.2 Analytical Results

In this section we present basic analysis of the model (3.6). We find the model has three steady states: a disease-free steady state (DFSS), a metastasis only steady state (MOSS), and a full disease steady state (FDSS). We discuss the existence of the steady states, and determine conditions guaranteeing the stability of the MOSS and the DFSS.

3.2.1 Steady States

Setting the eight equations above (Equation 3.6) to zero, we find that our model has three potential steady states. The first two arise from first assuming that $u_1 = 0$, followed by considering the cases when $u_2 = 0$ and $u_2 \neq 0$. The third steady state comes from assuming that $u_1 \neq 0$.

1. A disease-free steady state (DFSS), given by

$$(u_1, v_1, x_1, y_1, u_2, v_2, x_2, y_2) = \left(0, 0, \frac{\alpha_1}{\omega_1}, 0, 0, 0, \frac{\alpha_2}{\omega_2}, 0\right). \quad (3.12)$$

This state corresponds to a healthy individual. Both primary and secondary sites are cancer-free, and there is a non-zero immune presence throughout the body. For the purposes of informing treatment decisions, conditions for stability of this steady state are of interest, and are presented in the following section. Figure 3.4 shows the model solution when the DFSS is stable.

2. A metastatic-only steady state (MOSS), given by

$$(u_1, v_1, x_1, y_1, u_2, v_2, x_2, y_2) = \left(0, 0, \frac{\alpha_1}{\omega_1}, 0, \bar{u}_2, \bar{v}_2, \bar{x}_2, \bar{y}_2\right), \quad (3.13)$$

where the barred values (when they exist) are defined by the following equations:

$$\begin{aligned} g_2(\bar{u}_2) &= \frac{\sigma_2(\bar{x}_2, \bar{y}_2)}{\gamma_2(\bar{y}_2)} \\ \bar{v}_2 &= \frac{\theta_2}{\mu_2} \sigma_2(\bar{x}_2, \bar{y}_2) \bar{u}_2 \\ \bar{x}_2 &= \frac{-\alpha_2}{\lambda_2(\bar{u}_2, \bar{v}_2) - \rho_2 \bar{u}_2 - \omega_2 - ed_2(\bar{u}_2)} \\ \bar{y}_2 &= \frac{ed_2(\bar{u}_2) \bar{x}_2}{\tau_2 - f_2(\bar{u}_2)}. \end{aligned} \quad (3.14)$$

Observe that $\gamma_1(y_1) \geq 1 \forall y_1 \geq 0$, so the RHS of the first expression is always well-defined. However, we note that the expressions for \bar{x}_2 and \bar{y}_2 do not necessarily give non-negative values. In order for the model to

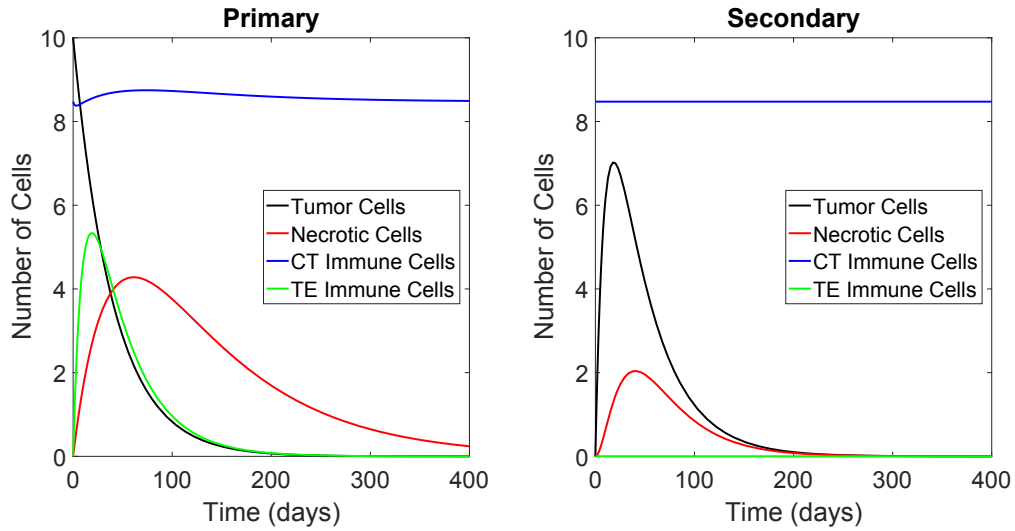


Figure 3.4: Simulation of the model 3.6 with parameters in Table 3.1, with the exception of $s_1 = 0.2$, $r_1 = 0.475$, and $r_2 = 0.2$ chosen in order to have FDSS stable. Initial conditions were $(10, 0, \frac{\alpha_1}{\omega_1}, 0, 0, 0, \frac{\alpha_2}{\omega_2}, 0)$. The dynamics at the primary site are on the left, and the dynamics at the secondary site are on the right. Quantities scaled in order to observe dynamics. Shown are: $u_1(t)$, $v_1(t) \times 10^{-3}$, $x_1(t) \cdot 5 \times 10^{-6}$, $y_1(t) \times 10^{-3}$, $u_2(t) \times 10^{10}$, $v_2(t) \times 10^7$, $x_2(t) \cdot 5 \times 10^{-6}$, $y_2(t) \times 10^{-3}$.

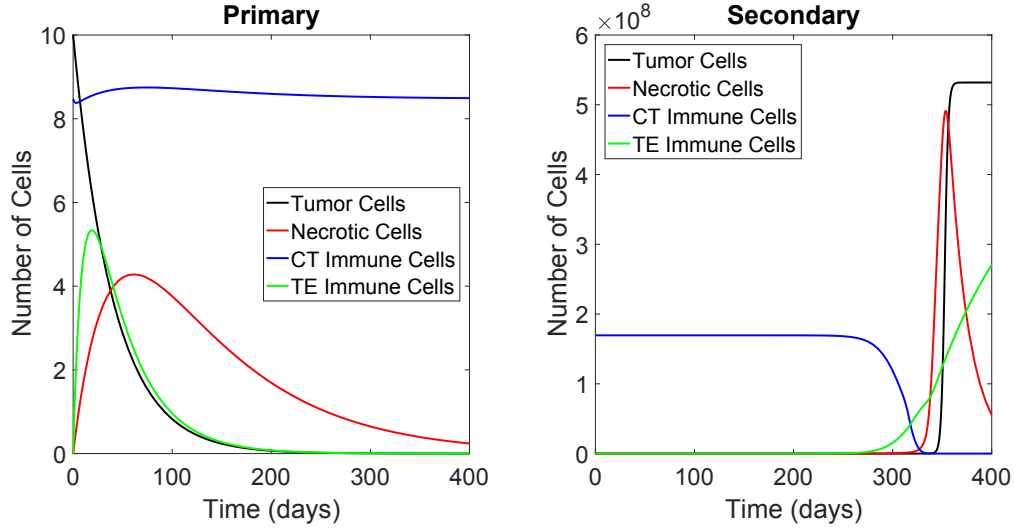


Figure 3.5: Simulation of the model 3.6 with parameters in Table 3.1, with the exception of $s_1 = 0.2$, and $r_1 = 0.475$, chosen in order to have MOSS stable. Initial conditions were $(10, 0, \frac{\alpha_1}{\omega_1}, 0, 0, 0, \frac{\alpha_2}{\omega_2}, 0)$. The dynamics at the primary site are on the left, and the dynamics at the secondary site are on the right. Quantities scaled in order to observe dynamics. Shown are: $u_1(t)$, $v_1(t) \times 10^{-3}$, $x_1(t) \cdot 5 \times 10^{-6}$, $y_1(t) \times 10^{-3}$, $u_2(t)$, $v_2(t) \times 10^2$, $x_2(t) \times 10^2$, $y_2(t) \times 10^3$. Note the difference in scales between the two sites.

remain biologically realistic, we must insist on non-negativity. Further, assuming that our growth function, g_2 , is non-negative and decreasing implies that for a solution to exist to the first equation in 3.14, we need the RHS to lie in the range of g_2 . Both of these observations give rise to assumptions which we discuss in greater detail below. Figure 3.5 shows the model dynamics when the MOSS is stable.

3. A full-disease steady state (FDSS) given by

$$(u_1, v_1, x_1, y_1, u_2, v_2, x_2, y_2) = (\tilde{u}_1, \tilde{v}_1, \tilde{x}_1, \tilde{y}_1, \tilde{u}_2, \tilde{v}_2, \tilde{x}_2, \tilde{y}_2) \quad (3.15)$$

where the values on the RHS are defined by the following equations,

$$\begin{aligned}
g_1(\tilde{u}_1) &= \frac{\sigma_1(\tilde{x}_1, \tilde{y}_1) + s_1}{\gamma_1(\tilde{y}_1)} \\
\tilde{v}_1 &= \frac{\theta_1}{\mu_1} \sigma_1(\tilde{x}_1, \tilde{y}_1) \tilde{u}_1 \\
\tilde{x}_1 &= \frac{-\alpha_1}{\lambda_1(\tilde{u}_1, \tilde{v}_1) - \rho_1 \tilde{u}_1 - \omega_1 - ed_1(\tilde{u}_1)} \\
\tilde{y}_1 &= \frac{ed_1(\tilde{u}_1) \tilde{x}_1}{\tau_1 + \tilde{s}_1 - f_1(\tilde{u}_1)} \\
\tilde{u}_2 &= \frac{est(\tilde{v}_2, \tilde{y}_2, \tilde{x}_2) s \tilde{u}_1}{\sigma_2(\tilde{x}_2, \tilde{y}_2) - \gamma_2(\tilde{y}_2) g_2(\tilde{u}_2)} \\
\tilde{v}_2 &= \frac{\theta_2}{\mu_2} \sigma_2(\tilde{x}_2, \tilde{y}_2) \tilde{u}_2 \\
\tilde{x}_2 &= \frac{-\alpha_2}{\lambda_2(\tilde{u}_2, \tilde{v}_2) - \rho_2 \tilde{u}_2 - \omega_2 - ed_2(\tilde{u}_2)} \\
\tilde{y}_2 &= \frac{ed_2(\tilde{u}_2) \tilde{x}_2 + p \tilde{s}_1 \tilde{y}_1}{\tau_2 - f_2(\tilde{u}_2)}.
\end{aligned} \tag{3.16}$$

As in the case of the MOSS, in order for biologically relevant FDSS to exist, a number of assumptions will need to be met. Non-negativity of the immune steady states is again a concern, as are solutions to the \tilde{u}_1 equation and the implicit \tilde{u}_2 equation. Figure 3.6 shows the model dynamics when the FDSS is stable. In contrast to the two previous figures, Figure 3.6 is presented with a log scale in order to capture the model dynamics with small values.

Before we proceed any further, we make a brief note on the *existence* of these steady states. It is unclear *a priori* that solutions to the expressions above exist. Of particular relevance for the coming results is the question of *boundedness* of the solutions to the immune cell populations. Indeed, because the steady state expressions for each of $x_{1,2}$ and $y_{1,2}$ involves a denominator that may change signs (have a root) in our domain of interest, we must be careful to ensure that such a root does not occur, as that would result in unbounded solutions. Based on the parameter estimates that we obtain in Section 3.3, the denominator cannot be zero and unboundedness of solutions

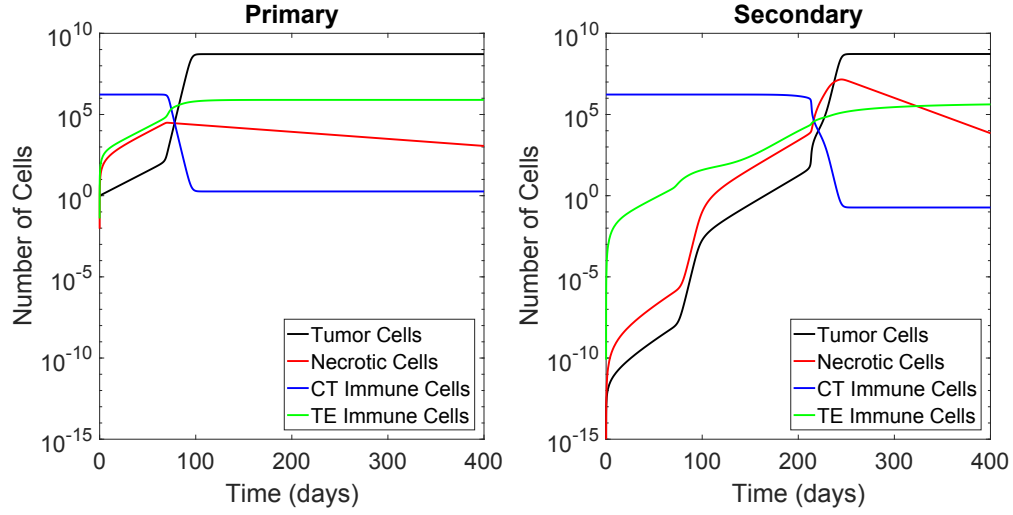


Figure 3.6: Simulation of the model 3.6 with parameters in Table 3.1. Initial conditions were $\left(1, 0, \frac{\alpha_1}{\omega_1}, 0, 0, 0, \frac{\alpha_2}{\omega_2}, 0\right)$. The dynamics at the primary site are on the left, and the dynamics at the secondary site are on the right.

is not an issue.

3.2.2 Stability Analysis

Because of its relevance to treatment, we now investigate the stability of the DFSS as well as the MOSS. We find an explicit condition required for disease eradication at both the primary and secondary sites.

Theorem 4. *The DFSS, when it exists, is stable if and only if both*

$$g_1(0) < s_1 + \sigma_1 \left(\frac{\alpha_1}{\omega_1}, 0 \right)$$

and

$$g_2(0) < \sigma_2 \left(\frac{\alpha_2}{\omega_2}, 0 \right)$$

are satisfied.

Proof. Let $J = (J_{i,j}) \in \mathbb{R}^{8 \times 8}$ denote the Jacobian matrix of the ODE system

(3.6). Simple computations show us that

$$J = \begin{pmatrix} J_{1,1} & 0 & J_{1,3} & J_{1,4} & 0 & 0 & 0 & 0 \\ J_{2,1} & J_{2,2} & J_{2,3} & J_{2,4} & 0 & 0 & 0 & 0 \\ J_{3,1} & J_{3,2} & J_{3,3} & 0 & 0 & 0 & 0 & 0 \\ J_{4,1} & 0 & J_{4,3} & J_{4,4} & 0 & 0 & 0 & 0 \\ J_{5,1} & 0 & 0 & 0 & J_{5,5} & J_{5,6} & J_{5,7} & J_{5,8} \\ 0 & 0 & 0 & 0 & J_{6,5} & J_{6,6} & J_{6,7} & J_{6,8} \\ 0 & 0 & 0 & 0 & J_{7,5} & J_{7,6} & J_{7,7} & 0 \\ 0 & 0 & 0 & J_{8,4} & J_{8,5} & 0 & J_{8,7} & J_{8,8} \end{pmatrix}, \quad (3.17)$$

where

- $J_{1,1} = \gamma_1(y_1)g_1(u_1) + \gamma_1(y_1)g_1'(u_1)u_1 - \sigma_1(x_1, y_1) - s_1,$
- $J_{1,3} = -u_1\partial_{x_1}\sigma_1(x_1, y_1),$
- $J_{1,4} = \gamma_1'(y_1)g_1(u_1)u_1 - u_1\partial_{y_1}\sigma_1(x_1, y_1),$
- $J_{2,1} = \theta_1\sigma_1(x_1, y_1),$
- $J_{2,2} = -\mu_1,$
- $J_{2,3} = \theta_1u_1\partial_{x_1}\sigma_1(x_1, y_1),$
- $J_{2,4} = \theta_1u_1\partial_{y_1}\sigma_1(x_1, y_1),$
- $J_{3,1} = (\partial_{u_1}\lambda_1(u_1, v_1) - \rho_1 - ed_1'(u_1))x_1,$
- $J_{3,2} = \partial_{v_1}\lambda_1(u_1, v_1)x_1,$
- $J_{3,3} = \lambda_1(u_1, v_1) - \rho_1u_1 - \omega_1 - ed_1(u_1),$
- $J_{4,1} = ed_1'(u_1)x_1 + f_1'(u_1)y_1,$
- $J_{4,3} = ed_1(u_1),$
- $J_{4,4} = -\tau_1 - \tilde{s}_1 + f_1(u_1),$
- $J_{5,1} = s_1est(v_2, x_2, y_2),$

- $J_{5,5} = \gamma_2(y_2)g_2(u_2) + \gamma_2(y_2)g_2'(u_2)u_2 - \sigma_2(x_2, y_2),$
- $J_{5,6} = s_1u_1\partial_{v_2}est(v_2, x_2, y_2),$
- $J_{5,7} = s_1u_1\partial_{x_2}est(v_2, x_2, y_2) - u_2\partial_{x_2}\sigma_2(x_2, y_2),$
- $J_{5,8} = \gamma_2'(y_2)g_2(u_2)u_2 + s_1u_1\partial_{y_2}est(v_2, x_2, y_2) - u_2\partial_{y_2}\sigma_2(x_2, y_2),$
- $J_{6,5} = \theta_2\sigma_2(x_2, y_2),$
- $J_{6,6} = -\mu_2,$
- $J_{6,7} = \theta_2u_2\partial_{x_2}\sigma_2(x_2, y_2),$
- $J_{6,8} = \theta_2u_2\partial_{y_2}\sigma_2(x_2, y_2),$
- $J_{7,5} = (\partial_{u_2}\lambda_2(u_2, v_2) - \rho_2 - ed_2'(u_2))x_2,$
- $J_{7,6} = \partial_{v_2}\lambda_2(u_2, v_2)x_2,$
- $J_{7,7} = \lambda_2(u_2, v_2) - \rho_2u_2 - \omega_2 - ed_2(u_2),$
- $J_{8,4} = p\tilde{s}_1,$
- $J_{8,5} = x_2ed_2'(u_2) + y_2f_2'(u_2),$
- $J_{8,7} = ed_2(u_2),$ and
- $J_{8,8} = -\tau_2 + f_2(u_2).$

We can also write J from (3.17) as a 2×2 lower-triangular block matrix with 4×4 blocks,

$$J = \left[\begin{array}{c|c} J^l & 0 \\ \hline J_l & J_r \end{array} \right],$$

meaning that the eigenvalues of J are simply the eigenvalues of the diagonal blocks, J^l and J_r . In order to determine the stability of the DFSS (3.12), we note that, evaluated at the DFSS, the following entries are 0:

- $J_{1,3} = -0 \cdot \partial_{x_1}\sigma_1\left(\frac{\alpha_1}{\omega_1}, 0\right) = 0,$

- $J_{1,4} = 0 \cdot \left(\gamma_1'(0)g_1(0) - \partial_{y_1}\sigma_1 \left(\frac{\alpha_1}{\omega_1}, 0 \right) \right) = 0,$
- $J_{2,3} = 0 \cdot \theta_1 \partial_{x_1}\sigma_1 \left(\frac{\alpha_1}{\omega_1}, 0 \right) = 0,$
- $J_{2,4} = 0 \cdot \theta_1 \partial_{y_1}\sigma_1 \left(\frac{\alpha_1}{\omega_1}, 0 \right) = 0,$
- $J_{5,6} = 0 \cdot s_1 \partial_{v_2} est \left(0, \frac{\alpha_2}{\omega_2}, 0 \right) = 0,$
- $J_{5,7} = 0 \cdot s_1 \partial_{x_2} est \left(0, \frac{\alpha_2}{\omega_2}, 0 \right) - 0 \cdot \partial_{x_2}\sigma_2 \left(\frac{\alpha_2}{\omega_2}, 0 \right) = 0,$
- $J_{5,8} = \gamma_2'(0)g_2(0) \cdot 0 + 0 \cdot s_1 \partial_{y_2} est \left(0, \frac{\alpha_2}{\omega_2}, 0 \right) - 0 \cdot \partial_{y_2}\sigma_2 \left(\frac{\alpha_2}{\omega_2}, 0 \right) = 0,$
- $J_{6,7} = 0 \cdot \theta_2 \partial_{x_2}\sigma_2 \left(\frac{\alpha_2}{\omega_2}, 0 \right) = 0,$ and
- $J_{6,8} = 0 \cdot \theta_2 \partial_{y_2}\sigma_2 \left(\frac{\alpha_2}{\omega_2}, 0 \right) = 0.$

Therefore, both J^l and J_r are lower triangular, and thus their eigenvalues (and so the eigenvalues of J) are the diagonal entries. Again, simple substitution and recall of the model assumptions ($\gamma_i(0) = 1$, $f_i(0) = 0$, $\lambda_i(0, 0) = 0$, $ed_i(0) = 0$) show that

- $J_{1,1} = \gamma_1(0)g_1(0) - \sigma_1 \left(\frac{\alpha_1}{\omega_1}, 0 \right) - s_1 = g_1(0) - \sigma_1 \left(\frac{\alpha_1}{\omega_1}, 0 \right) - s_1,$
- $J_{2,2} = -\mu_1 < 0,$
- $J_{3,3} = \lambda_1(0, 0) - \omega_1 - ed_1(0) = -\omega_1 < 0,$
- $J_{4,4} = -\tau_1 - \tilde{s}_1 + f_1(0) = -(\tau_1 + \tilde{s}_1) < 0,$
- $J_{5,5} = \gamma_2(0)g_2(0) - \sigma_2 \left(\frac{\alpha_2}{\omega_2}, 0 \right) = g_2(0) - \sigma_2 \left(\frac{\alpha_2}{\omega_2}, 0 \right),$
- $J_{6,6} = -\mu_2 < 0,$
- $J_{7,7} = \lambda_2(0, 0) - \omega_2 - ed_2(0) = -\omega_2 < 0,$ and
- $J_{8,8} = -\tau_2 + f_2(0) = -\tau_2 < 0.$

It is clear from above that the only eigenvalues that are not necessarily negative are $J_{1,1}$ and $J_{5,5}$. The result follows immediately. \square

We also note that the de-coupling of the primary and secondary sites — in particular the fact that the secondary site does not influence the primary site in any way — allows us to reach a (partial) conclusion concerning the stability of the MOSS.

Corollary 2. *If*

$$g_1(0) < s_1 + \sigma_1 \left(\frac{\alpha_1}{\omega_1}, 0 \right),$$

then extinction of the primary tumor is stable.

These results lead to an interesting question concerning possible *bi-stability*. Indeed, while we have presented conditions that guarantee the *stability* of the extinction steady states, we have not shown extinction is the *only* possibility under these conditions. We investigate possible bistability numerically in this chapter, but provide a more detailed analysis on a simplified version of the model 3.6 in Chapter 4.

3.3 Parameter Estimation

In order to parameterize the model, we searched both experimental and theoretical literature. While estimates were obtained for several of the model parameters, many parameters have not previously been investigated in the literature. When this was the case, educated guesses were made, or parameters were tuned in order to achieve a desired outcome. As an example of the former, many of the threshold values presented in Table 3.1 are reported without a reference. When a CT immune cell threshold was required, we chose the thresholds relative to the DFSS value of $\frac{\alpha_i}{\omega_i}$ for $i = 1, 2$ (15% and 65% for lower and upper, respectively, was a common choice). TE immune thresholds were chosen to be one order of magnitude smaller than for CT immune cells. Necrotic cell thresholds were 5% and 55% of the tumor carrying capacity, $K_{1,2}$. As an example of tuning parameters to achieve a desired model outcome, the CT immune cell influx rate, $\alpha_{1,2}$, was tuned so that the DFSS CT immune cell population would be of the order 10^6 [34, 106, 130]. When educated guesses were impossible, we simply chose values that *seemed* reasonable in some sense.

Parameter	Description	Value	Units	References
$r_{1,2}$	tumor growth rate	0.38	1/day	[115]
$K_{1,2}$	tumor carrying capacity	5.3196×10^8	cells	[115]
$\theta_{1,2}$	CSC scaling constant	65.67	—	[46, 118]
$\mu_{1,2}$	dead cell lysis rate	0.01, 0.05	1/day	[45, 120]
$\alpha_{1,2}$	CT immune influx rate	1×10^6	1/day	[45]
$\rho_{1,2}$	fatal immune-tumor interaction rate	0.001, 0.01	1/day	[45]
$\omega_{1,2}$	CT decay rate	0.59	1/day	[115]
$\chi_{1,2}$	immune education rate	5×10^{-5}	1/day	[34, 86]
$\tau_{1,2}$	TE decay rate	0.05	1/day	[45]
s_1	tumor shedding rate	0.01	1/day	[57, 83]
\tilde{s}	TE shedding rate	0.05	1/day	[45]
p	proportion successful TE	1×10^{-4}	—	—
$min_{1,2}$	min TE growth	1	—	—
$max_{1,2}$	max (increase) TE growth	0.5	—	—
$low_{1,2}$	growth activation	25424	cells	—
$up_{1,2}$	growth saturation	110169	cells	—
$lowD_{1,2}$	death activation: TE	25424	cells	—
$upD_{1,2}$	death saturation: TE	110169	cells	—
$minC_{1,2}$	min death rate	0.2	1/day	[109, 121]
$maxC_{1,2}$	max increase death	0.1	1/day	—
$lowC_{1,2}$	death activation: CT	254237	cells	—
$upC_{1,2}$	death saturation: CT	1101695	cells	—
$a_{11,12}$	CT expansion: tumor	0.524	1/day	[90]
$a_{21,22}$	CT expansion: dead	0.786	1/day	—
$b_{11,12,21,22}$	immune damping (dead;tumor)	1.61×10^5	cells	[90]
$ht_{1,2}$	TE expansion rate	0.04	1/day	[90, 115]
$hb_{1,2}$	TE expansion damping	1.6×10^5	cells	[90, 115]
MER	max (increase) establish rate	100	—	[56]
$lowEst_{CT,TE}$	activation level: establish	254237, 25424	cells	—
$upEst_{CT,TE}$	saturation level: establish	1101695, 110169	cells	—
$minEst_{TE,V}$	min establish rate	0.001	1/day	[15, 19, 83, 100]
$maxEst$	max establish rate (increase)	0.002	1/day	—
$lowV$	activation: dead cells	2.66×10^7	cells	—
upV	saturation: dead cells	2.93×10^8	cells	—
$minV$	min establish rate	0.001	1/day	—
$maxV$	max establish rate (increase)	0.999	1/day	—

Table 3.1: Model Parameters and the values used in presented simulations.

For instance, we assumed that TE immune cell effects could increase the tumor growth rate by 50% because this seems both reasonable and conservative. We also note that, while the model allows for different parameter values between the distant tumor sites, we have followed the example of the Enderling group [115] and, without any strong evidence to suggest otherwise, used the same parameters at both the primary and the secondary site.

3.4 Numerical Results

In this section we present results of numerical simulations of the model using MATLAB and the built-in ODE solver ‘ode15s’. The results of Theorem 4 were demonstrated in Figures 3.4, 3.5, and 3.6. Below, we perform a number of numerical experiments in order to gain an understanding of the model predictions. We use the parameterized model to conduct numerical investigations into the effects of primary tumor resection, immune therapies, and injury.

3.4.1 Primary Resection

We begin this section by considering the model-predicted effects of primary tumor resection. The gold-standard treatment for many tumors is surgical removal (resection). In perfect conditions, this would mean removal of 100% of the cells making up the tumor. However, surgery is rarely this efficient, and the surgeons can only remove what they can see. Consequently, there is always a risk that a small number of cancer cells — invisible to the naked eye and medical imaging techniques — may be left within the tumor environment after surgery, leading to recurrence. In an attempt to remove the remaining cells that cannot be removed by surgery and hopefully prevent local recurrence, surgery is often paired with other treatments, such as radiation, chemotherapy, or immune therapies.

Potential metastatic tumors only complicate the situation. Indeed, surgery to remove a primary tumor does little to *directly* address any potential distant metastatic tumors. While there have been reports of *indirect* effects of primary resection on secondary tumor growth, through an *abscopal effect*, these effects

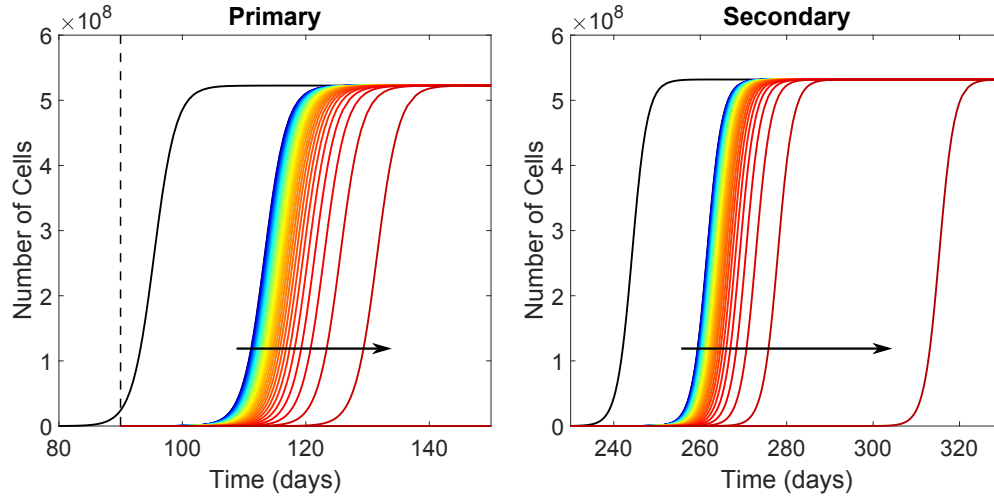


Figure 3.7: Effects of primary resection on tumor population dynamics at the primary (left) and secondary (right) sites. Primary tumor was removed at time $t = 90$ days (vertical dashed line in left plot) with efficiency ranging from 99.99% to 100% (blue to red). Arrow indicates the direction of increasing resection efficiency. The black curves represent control dynamics.

and their underlying causes remain poorly understood.

In order to investigate the predictions of our model on the effects of primary tumor resection, we perform a series of numerical investigations simulating the effects of surgery at the primary site. Our simulations begin with a single cancer cell at the primary site and DFSS CT immune levels at both sites. The primary tumor is allowed to grow until it reaches a size that may be considered *clinically detectable*. In our simulations we have assumed that this level is achieved at a primary tumor composed of approximately 10^7 cells, which occurs at $t = 90$ days after tumor initiation. At day 90, resection of the primary tumor is performed with a prescribed efficiency. A resection of $rEff\%$ efficiency is achieved by stopping the simulation, removing $rEff\%$ of *each* of the quantities at the primary site, and restarting the simulation with these reduced quantities as initial conditions. While more intricate simulations could be performed — and are discussed further in Section 3.5 — we have chosen to use this simple procedure to coincide more closely with the simulations presented in [115].

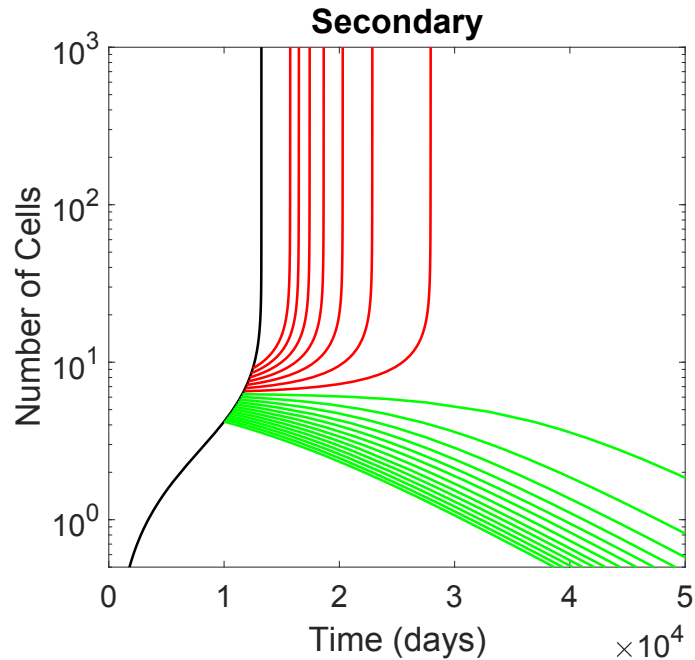


Figure 3.8: Effect of primary resection on secondary tumor dynamics for various times of primary resection, ranging between $t = 10000$ and $t = 12500$ days. Primary resection was assumed to be 100% effective, meaning there was no influence on secondary site from the primary site following resection. Secondary tumor growth rate was $r_2 = 0.2999$ so that extinction of metastases was stable. The black trajectory shows secondary tumor growth without primary resection and acts as a control curve. Green trajectories are destined for extinction, while red trajectories are destined for full secondary tumor.

The results of these primary resection simulations for removal efficiency varying between 99.99% and 100% are presented in Figure 3.7. This range was chosen in order to observe any noticeable effect from surgical intervention — smaller removal efficiencies had little effect. Primary and secondary dynamics are presented on the left and right hand sides of Figure 3.7, respectively. The delay in tumor regrowth at both sites is increased as we increase the removal efficiency (blue to red). If our surgery is anything less than 100% efficient, primary recurrence is expected. Even with successful removal of the primary tumor, we still expect to see a secondary tumor develop after a significant delay.

Based on the observation of secondary persistence even upon primary ex-

tion, we investigate the possibility of bi-stability in the model by way of resection simulations. In Figure 3.8 we show secondary tumor cell dynamics in response to 100% primary resection at varying times. Parameters were chosen so that extinction at the secondary site was stable (Theorem 4). If the primary is removed sufficiently early, the secondary tumor may go extinct (green curves). However, if the primary is removed later than a threshold time, thereby allowing the secondary tumor to grow large enough to support itself, primary resection only delays metastatic growth, with a full secondary tumor expected to develop. We note that the choices of parameters used to produce Figure 3.8 may not be realistic, given the long timescale that results.

3.4.2 Immune Therapy

As mentioned in the previous section, primary tumor resections are often coupled with other therapeutic approaches. Of particular interest to us are immunotherapies. The term ‘immunotherapy’ is general, and can refer to many different therapeutic approaches, all with the goal of taking advantage of the ability of the immune system to effectively kill foreign invaders. Approaches range from tumor ‘vaccines’, which serve to identify the cancer cells to CT immune cells (by various methods) in order to illicit a response, to stimulation of the production of CT immune cells (such as $CD8^+$ or NK cells) through the use of cytokines or chemokines, to the simple injection of additional CT immune cells.

While the concept of using a patient’s own immune response to destroy a tumor has inspired significant experimental and theoretical research into immunotherapies, their effectiveness has proven somewhat disappointing. One possible explanation for this unexpected result is the complex interplay between the anti- and pro-tumor effects of the immune system. We use our model to investigate the effect of these contradictory roles on immunotherapies. For simplicity, ‘immunotherapy’ in the context of our model is any intervention that results in an increased influx of CT immune cells. This is a sufficiently general modeling choice to approximate each of the previously mentioned immunotherapeutic approaches. Indeed, the goal of vaccines, cytokine therapies,

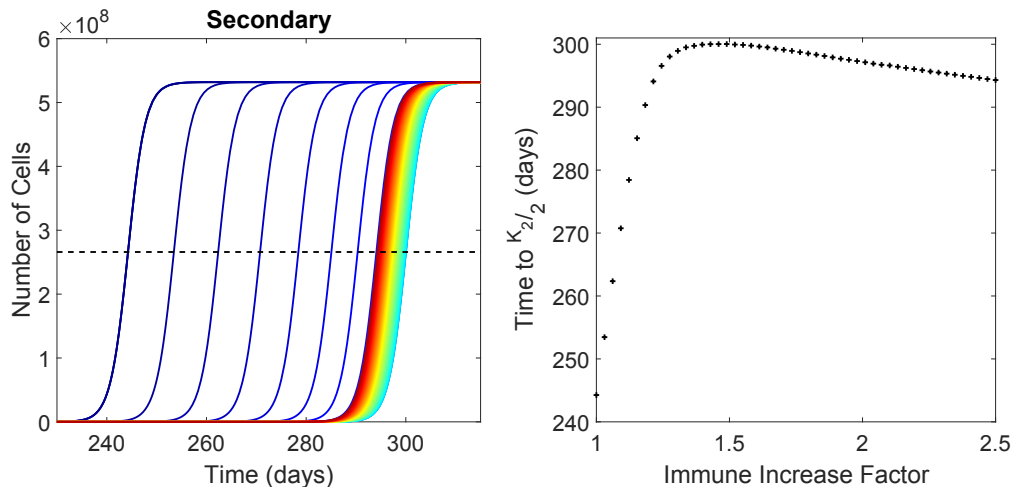


Figure 3.9: Effect of immune therapy on growth of the metastatic tumor. Left: Tumor cell dynamics at the secondary site for increasing CT immune cell influx rates, α_1 and α_2 . Therapy administered at time $t = 90$ days. Values are increasing from blue to red. Dash line represents half the carrying capacity, $K_2/2$. Right: Time secondary tumor reaches half its carrying capacity as a function of the factor the CT immune cell influx rate increased.

and immune supplementation is an increased number of effective CT immune cells present at the tumor site. We simulate this increased population of effective CT immune cells by increasing the CT immune cell influx rates, $\alpha_{1,2}$, by a scaling factor ≥ 1 . As in the case of primary resection, such an intervention requires the identification of a primary tumor, so we begin therapy on day 90 and, for simplicity, assume that this therapy is continuously applied until the end of the simulation. Our model predicts that immunotherapy has little to no effect on the primary tumor if we wait for it to grow to a *clinically detectable* size. Therefore, we have presented only the dynamics at the secondary site.

Figure 3.9 shows the effect of immunotherapy on the growth dynamics of the secondary tumor for a range of increases to the immune influx rates, $\alpha_{1,2}$. On the left are the time dynamics of the tumor, with $\alpha_{1,2}$ increasing as we go from blue to red, with the leftmost curve acting as the control curve. The dashed line denotes a population size of *half* the carrying capacity at the secondary site ($K_2/2$). On the right we have the time to $K_2/2$ as a function of the increase to $\alpha_{1,2}$ which are simply the intersection points of dashed line and

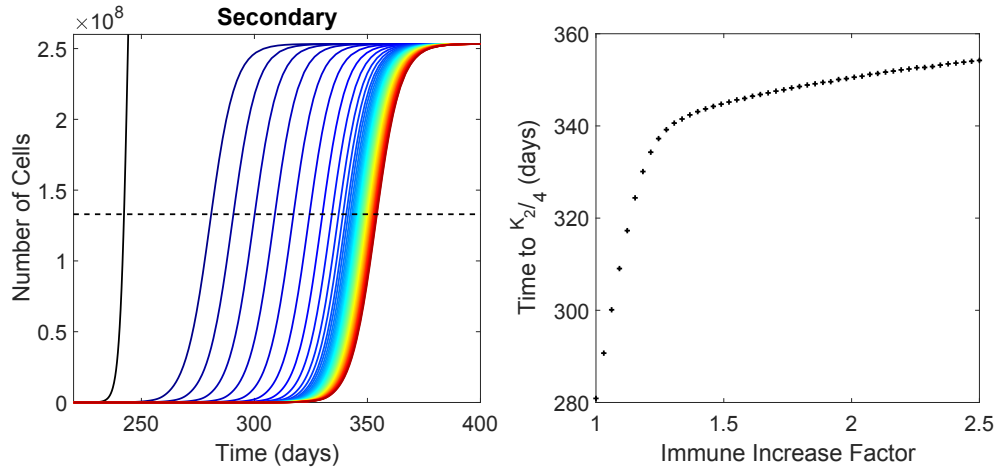


Figure 3.10: Effect of two-pronged immune therapy on growth of the metastatic tumor. Left: Tumor cell dynamics at the secondary site for increasing CT immune cell influx rates, α_1 and α_2 , and prevention of immune education, $\chi_{1,2} = 0$. Therapy administered at time $t = 90$ days. Values are increasing from blue to red. Leftmost curve represents control dynamics. Dash line represents one quarter the carrying capacity, $K_2/4$. Right: Time secondary tumor reaches a quarter its carrying capacity as a function of the factor the CT immune cell influx rate increased.

solution curves in left plot. For small increases in $\alpha_{1,2}$ we see a marked delay in tumor growth. However, this effect not only saturates, but actually becomes *detrimental* for larger increases. This is a result of the tumor’s ‘education’ of CT immune cells into pro-tumor TE immune cells. Indeed, this can be seen by comparing the results of Figure 3.9 with those in Figure 3.10.

Figure 3.10 was produced assuming that immunotherapy also prevented the direct tumor education of CT immune cells ($\chi_{1,2} = 0$). First, we note that this assumption results in a final tumor of approximately *half* the size observed in Figure 3.9. Consequently, the endpoint considered here is $K_2/4$ (dashed line). Second, the tumor delay is also appreciably longer when compared to those presented in Figure 3.9. Third, while the time-to-endpoint slows dramatically (right), it monotonically increases over the entire range of values tested. These results suggest that tumor education of immune cells is responsible for the non-monotonicity observed in Figure 3.9.

Figure 3.11 shows the effects of combination resection-immunotherapy on

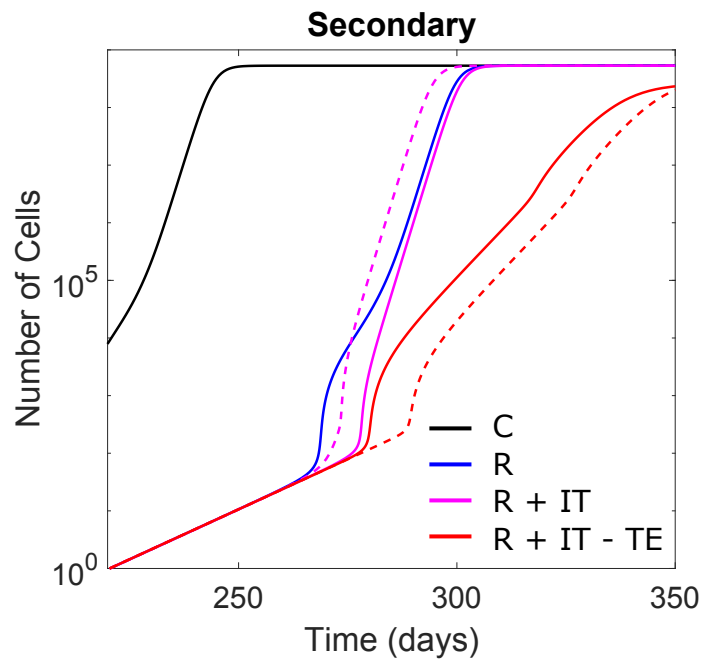


Figure 3.11: Effects of different combination therapies on the dynamics of the secondary tumor. Black is control, blue is resection only, magenta is resection and increased immune cell influx rate, and blue is resection, increased immune cell influx rate, and decrease in tumor education rate. Resection was done with 99.999999% efficiency, education rates decreased by factors of 10, and CT influx rates increased by factors of 1.5 (solid) and 2.5 (dashed). Control parameters as in Table 3.1. All treatments initiated at time $t = 90$ days.

the dynamics of the secondary tumor. Primary resection alone (blue curve) offers significant growth delay compared to the control dynamics (black curve), but combination with immunotherapy does not necessarily result in improved outcome. Indeed, if we increase $\alpha_{1,2}$ by a factor of 1.5 we see a modest improvement over resection alone (magenta solid). However, increasing the CT influx rate further results in a *worse* outcome than resection alone (magenta dashed). Immunotherapy that includes *both* an increase to the CT immune cell influx rate *and* a decrease in the education rate of CT immune cells (red curves) is more effective than immunotherapy that includes only one of these approaches. Moreover, in agreement with the results in Figure 3.10, increasing the factor by which we increase the CT immune cell influx rate from 1.5 (solid) to 2.5 (dashed) results in a marked improvement in tumor growth delay.

3.4.3 Injury at Secondary Site

The theory of immune-mediated metastasis proposed by Shahriyari [124] provided a potential explanation for the observation that metastases appear at the sites of injury via immune-assisted trafficking of cancer cells to the growth-supporting injury site (See Section 1.1.2 for full details). We use our model to explore the implications of an injury incurred at a distant secondary site.

To simulate an injury at the secondary site, we introduce an ‘injury’ consisting of 1×10^7 necrotic cells to the secondary population of necrotic cells at the time of injury. In order to evaluate the effect of the injury on metastatic growth, we determine the time required for the secondary tumor to reach a population of $K_2/2 = 2.6595 \times 10^8$ cells. Figure 3.12 shows how the *timing* of the injury influences secondary tumor growth. Our model predicts *early* and *late* responses: if the injury occurs relatively *early* in the progression of the primary tumor it will have beneficial effects on secondary tumor growth delay (green), whereas *late* injuries have the opposite effect (red). *Early* and *late* effects are distinguished by the dashed line, denoting the control results.

To gain insight into the underlying dynamics responsible for this biphasic behavior, we have chosen the injury times corresponding to the best ($t = 74.1$ — slightly *before* clinical detectability) and worst ($t = 102.5$ — slightly *after*

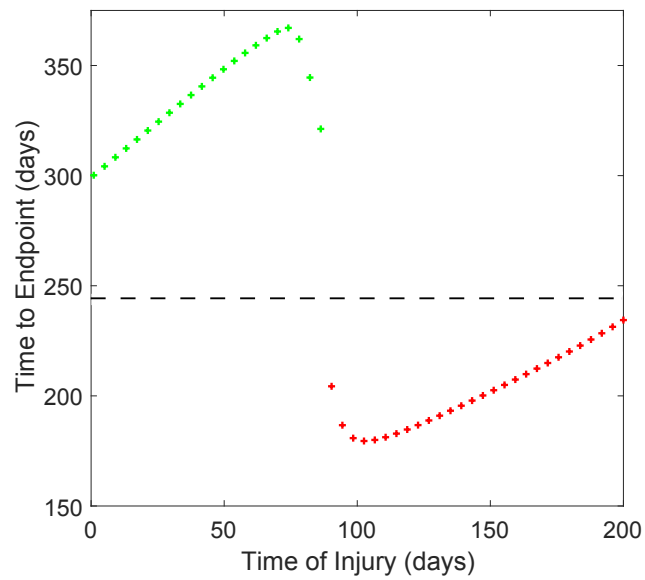


Figure 3.12: Time required for secondary tumor to reach $K_2/2 = 2.6595 \times 10^8$ cells as a function of the time an injury of 1×10^7 necrotic cells was incurred. Dashed line represents the control value. Green indicates a desirable outcome, while red indicates an undesirable outcome. Parameters as in Table 3.1.

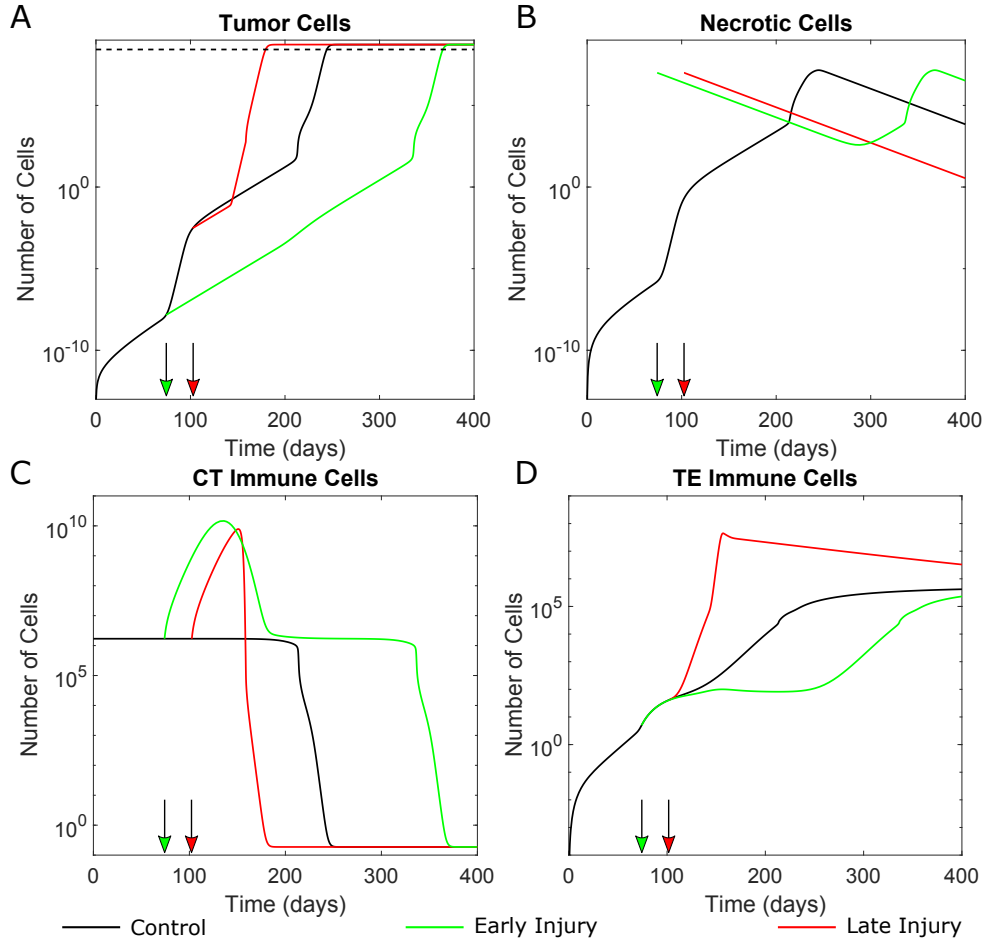


Figure 3.13: Dynamics of the tumor cells, (A), necrotic cells (B), CT immune cells (C), and TE immune cells (D) at the secondary tumor site upon the simulation of an injury. Two injury times are presented (arrows): an *early* injury at $t = 74.1$ days (green) and a *late* injury at $t = 102.5$ days (red). Injury was 1×10^7 necrotic cells. Dashed line in (A) represents endpoint value of $K_2/2$. Parameters as in Table 3.1.

clinical detectability) outcomes presented in Figure 3.12 and investigated the resulting dynamics at the secondary site. These results are summarized in Figure 3.13. Control (black), *early* injury (red), and *late* injury dynamics are presented for the secondary tumor cells (A), necrotic cells (B), CT immune cells (C), and TE immune cells (D). The times of injury are reported as arrows along the horizontal axis, and the endpoint tumor size $K_2/2$ is marked by the dashed line in (A).

An immediate and significant CT immune response is observed after both injuries (Figure 3.13, (C)). In the *early* injury case, this response is slightly larger and is maintained for a much longer period of time relative to the case of a *late* injury, where an abrupt, precipitous decline is observed after having reached a maximum. In concert with this decline in CT immune cells is a rapid increase in the TE immune population (Figure 3.13 (D), red). The combined effect of a decreased CT immune population and increased TE immune population results in the rapid growth of the tumor (Figure 3.13 (A), red), whereas the relatively large CT immune population and small TE immune population in the *early* injury case allows for the prolonged suppression of tumor growth (Figure 3.13 (A), green).

Note that the injuries occur on either side of a period of significant tumor growth (Figure 3.13 (A), black). At the time of the *early* injury, the tumor is sufficiently small that tumor education of CT immune cells is negligible, meaning that the CT immune response to the injury remains largely anti-tumor. At the time of the *late* injury, however, the tumor has grown to such a size that tumor education of CT immune cells is no longer negligible, and the CT immune response to injury is quickly educated by the tumor to become tumor-promoting.

Even with a large injection of necrotic cells at the secondary site, the resulting spike in CT immune cells ensures that the establishment rate remains low for a period after the injury in both simulations (Figure 3.14). Once the CT immune cells have been cleared from the secondary site, we see the establishment rate increase. This spike in the establishment rate occurs at approximately the same time as the final increase in tumor growth rate in all three curves in Figure 3.13 (A).

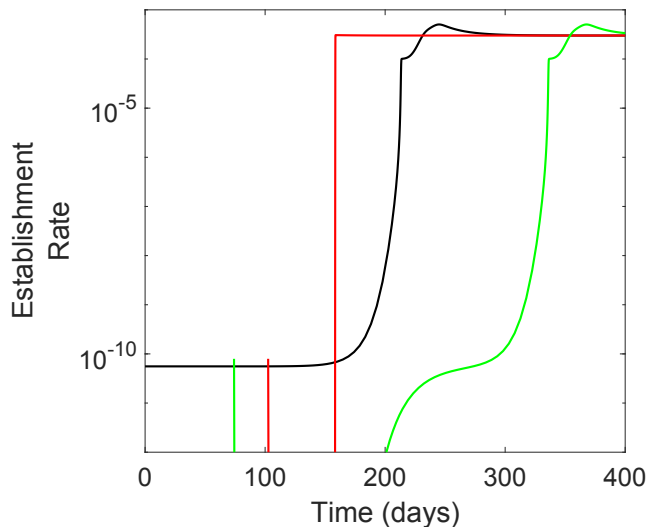


Figure 3.14: Establishment rate as a function of time for the injury simulations presented in Figure 3.13. Two injury times are presented: an *early* injury at $t = 74.1$ days (green) and a *late* injury at $t = 102.5$ days (red). Injury was 1×10^7 necrotic cells. Parameters as in Table 3.1.

3.5 Discussion

In this chapter, we developed an ODE model to interrogate the validity of the ‘immune-mediated’ theory of cancer metastasis [124]. Our model consisted of a system of 8 coupled ODEs describing the dynamics of tumor cells, necrotic cells, anti-tumor CT immune cells, and pro-tumor TE immune cells at the sites of both a primary tumor and a distant metastatic tumor. We performed steady state analysis and derived conditions required for disease extinction. After parameterizing the model based on estimates in the literature (where available), the parameterized model was used to conduct several numerical experiments.

The results presented herein should be taken with a degree of caution. We have chosen to model metastasis — an inherently *spatial* process — with spatially homogenous ODEs. This is certainly a simplification and a spatially explicit model should be developed and analyzed further. As is the case with other models for tumor-immune interactions including pro-tumor effects

[34, 138], parameter estimation in the current work was difficult given the dearth of available data. Consequently, many parameters were chosen without a specific reference from the literature, and the resulting predictions may be inappropriate. For example, the number of CT immune cells recruited to the injury site — on the order of 10^{10} cells — is potentially unrealistically large given the human body is estimated to be composed of $\sim 10^{13}$ cells [12]. We also observed that the efficiency of primary tumor resection must be very near 100% in order to see any appreciable effect on the system dynamics (Figure 3.7) which is likely too restrictive. Moreover, for simplicity we assumed equal parameters at both the primary and secondary site, which is almost certainly not the case. We also note that the model itself may have unnecessary dependencies — such as TE immune cells playing a role in *both* the tumor cell birth rate *and* the death rate — which may serve only to complicate the model and obscure the results. A simplified version of the model is presented and analyzed in Chapter 4.

The model presented above considers only two tumor sites — a primary site and a secondary, metastatic site — but could easily be modified to include $N > 2$ sites by borrowing network modeling ideas from [85, 115, 134]. We provide a brief sketch of such a model now. Let u_i , v_i , x_i , and y_i denote the number of cancer, necrotic, CT, and TE cells at tumor site i , where $i = 1, 2, \dots, N$. Let $\phi_{i,j}$, $\psi_{i,j}$, and $\zeta_{i,j}$ denote the number of tumor cells, TE immune cells, and CT immune cells respectively, leaving site j and arriving at site i . We assume that necrotic cells do not travel between sites. Under the above assumptions, we arrive at the following N site model for tumor-immune interactions including both pro- and anti-tumor immune effects

$$\begin{aligned}
\frac{du_i}{dt} &= \gamma_i(y_i)g_i(u_i)u_i - \sigma_i(x_i, y_i)u_i - s_iu_i + est_i(v_i, x_i, y_i) \left(\sum_{j=1}^N \phi_{i,j} \right) \\
\frac{dv_i}{dt} &= \theta_i\sigma_i(x_i, y_i)u_i - \mu_iv_i \\
\frac{dx_i}{dt} &= \alpha_i - \rho_iu_ix_i - \omega_ix_i - ed_i(u_i)x_i + \left(\sum_{j=1}^N \zeta_{i,j}\lambda_j(u_j, v_j)x_j \right) \\
\frac{dy_i}{dt} &= ed_i(u_i)x_i - \tau_iy_i - \tilde{s}_iy_i + \left(\sum_{j=1}^N \psi_{i,j}f_j(u_j)y_j \right).
\end{aligned} \tag{3.18}$$

Modeling of the connection terms, $\phi_{i,j}$, $\psi_{i,j}$, and $\zeta_{i,j}$, is a complicated problem (see [115, 134, 135] for discussion on the $\zeta_{i,j}$ term) and left as future research.

A final note of caution concerning the model itself is the choice of death functions. We have chosen to have the tumor death rates decrease to zero as the TE immune pool saturates. It is for this reason that we see the gradual extinction of necrotic cells in our model dynamics (Figure 3.6), instead of a stable population of necrotic cells that may be observed at the core of a sufficiently large solid tumor. However, if we recall our assumption that the ‘tumor’ cells modeled are CSCs, immortality is not necessarily unfounded [73], in which case a slightly different formulation of the necrotic cell dynamics may be necessary. In a related note, the model predicts the CSC population to reach the carrying capacity of the entire tumor. Based on the theoretical results in [73], this may also be more reasonable than it first appears. Indeed, the CSC fraction within a solid tumor is a highly debated area of active research [46].

In contrast to many of the previous models for tumor-immune interactions, the model developed here includes pro-tumor effects of the immune system in addition to the well-known anti-tumor effects. With inflammation recently named as a ‘hallmark of cancer’ [60], this inclusion is of the utmost importance, and its use in mathematical models for tumor-immune interactions is beginning to gain traction. den Breems and Eftimie [34] developed an ODE model for tumor-macrophage interactions in which a transition between anti-

and pro-tumor macrophages was included. Upon data-assisted parameterization of the model, the authors found that the transition rates between the macrophage types played an important role in the final outcome and suggested that future study was warranted. Our model included a similar ‘transition’ between immune types, which we termed ‘tumor education’. Similarly to den Breems, we found that the transition/education rate plays an important role in the system dynamics (See Figure 3.13), especially in the context of immunotherapies. Indeed, the education terms allow for non-monotonic behavior with immunotherapies, and provides a potential explanation for the poor performance of immunotherapies in the clinical setting (Figures 3.9, 3.10, and 3.11). It should also be noted that we explicitly model the process of metastatic dissemination and establishment, which was absent in the papers by the Enderling group [115, 134].

Theorem 4 gave us an explicit condition necessary to have complete disease extinction. In simple terms, if the growth rate is less than the death rate, extinction is stable. This is intuitive and allows us to conclude that primary resection alone — assuming some level of inefficiency — will not likely be curative, with local recurrence and distant metastasis the most likely outcomes. We did, however, show that complete removal of the primary tumor can, in some instances, lead to metastatic extinction or persistent metastatic disease, sometimes after a period of *dormancy* (Figure 3.8). In Chapter 4 we explore the phenomena of bistability and dormancy further using a simplified version of the model developed above. In general, however, our model predicts that resection should be coupled with a treatment that decreases tumor growth rate or increases its death rate.

Immunotherapies are aimed at increasing tumor cell death with the help of CT immune cells. Our model predicts that the desired effect may not always be achieved by simply increasing the influx rate of CT immune cells if ‘tumor education’ [107] is possible. If, however, there is a method to inhibit tumor education of CT immune cells, our model predicts much improved outcomes (Figure 3.11). While our model — with general anti- or pro-tumor immune cells — may be too general to provide clinical treatment insight, the results presented herein suggest that more detailed studies involving immune pheno-

typic plasticity may be warranted as the dynamics are relevant to treatment outcomes.

Preferential metastatic dissemination to sites of injury has been used as evidence to support the immune-mediated theory of metastasis [124]. Our model predicts that injury at a secondary site can have very different effects depending on the time of injury relative to disease progression. The influx of CT immune cells in response to a wound can be tumor-suppressing, if the local tumor is sufficiently small to make ‘education’ negligible, or tumor-promoting, if the tumor has grown to such a point that it can effectively ‘educate’ the infiltrating CT immune cells causing them to become tumor-promoting. Therefore, our model can successfully reproduce instances of rapid metastasis to the sites of injury.

The tumor-suppressing effects of immune activation upon injury are reminiscent of hypothesized mechanisms for the *abscopal effect* [37]. In the context of a combination radiation and immunotherapy, Dewan and collaborators suggested that a single large dose of radiation provided enough signals from dead cancer cells to ‘awaken’ the immune system to the cancer’s presence, both at the site of radiation and distant metastatic sites. Once ‘awakened’ to the presence of the cancer, the host immune system was able to induce an effective defence, resulting in decreased tumor burden at metastatic sites. Our model suggests that a similar ‘immune activation’ occurs upon injury, and that this effect is beneficial assuming the response can remain tumor-inhibitory, which may be the case in a combination treatment scenario.

The resection simulations presented in Figure 3.8 modeled the effects of primary resection on the secondary site by simply ‘turning off’ the sources of cancer and TE immune cells from the primary site. It has been shown, however, that a strong, short-lived, systemic immune response is observed upon primary resection [113]. Therefore, the inclusion of an immune response in addition to the switching off of the source terms at the secondary site will provide a more accurate model of the effects of primary resection on growth at the secondary site. An initial simulation including an inflammatory response is presented in Figure 3.15 (magenta), in which the immune influx rate was increased 500 times at the same time the source terms were ‘turned off’. For

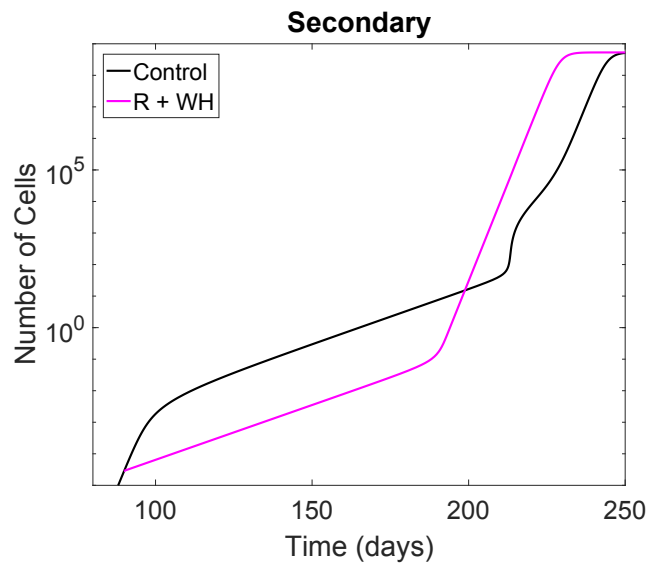


Figure 3.15: Secondary tumor cell dynamics upon primary resection that induces a sustained inflammatory response. The black curve is the control tumor growth at the secondary site (no intervention), while the magenta curve describes secondary tumor growth after primary resection and a wound-healing response ($\alpha_{1,2}$ increased by a factor of 500). All other parameters as in Table 3.1.

nearly 100 days, the abscopal effects felt by the secondary tumor in response to primary resection kept its size below that of the control tumor (black). In the case that the primary tumor was surgically removed, positive abscopal effects give way to negative abscopal effects slightly before day 200 of the simulation, at which time the model predicts metastatic ‘blow-up’, with the ‘treated’ metastatic tumor outgrowing the control tumor. Therefore, our model suggests that ‘metastatic blow-up’ is a phenomenon of the *pro*-tumor effects of the immune system. In contrast, Eikenberry et al. [45] suggest that (local) metastatic blow-up is the result of a weakened *anti*-tumor immune response. Many other theories explaining metastatic blow-up rely on the assumption that the primary tumor actively suppresses secondary growth through the production and dissemination of anti-angiogenic factors or other cytokines (see [45] and references therein). While further research must be done in order to elucidate the exact mechanism responsible for metastatic blow-up, our model gives us reason to suspect that the immune system plays a critical role, and that the inflammatory response to primary resection surgery should not be discounted.

We note that the model of primary resection inducing an inflammatory response described above is the same as the model used for combination resection and immunotherapy (Figures 3.9, 3.10, and 3.11). Consequently, we see that the effects of tumor-education can not only *reduce* the effectiveness of immunotherapies (as in Figure 3.9), but can also render their effects *harmful* by causing metastatic blow-up (as in Figure 3.15). The role of tumor-education is critical in these results, as Figure 3.10 demonstrates, and is the key factor preventing a monotonic increase in immunotherapy effectiveness. The results of immune phenotypic plasticity is, therefore, of utmost importance in terms of treatment planning, and further study is needed.

Whereas the importance of the contradictory anti- and pro-tumor roles of the immune system has long been appreciated, the implications of this dichotomy have only recently become the subject of rigorous investigation. The model of immune-mediated metastasis presented in this chapter has shown — by successfully reproducing well-known metastatic phenomena such as dormancy, blow-up, and metastasis to sites of injury, as well as providing a potential explanation for the poor performance of immunotherapies — that both

the tumor *inhibiting* and tumor *promoting* roles of the immune system are important to consider when designing models of cancer progression and treatment. Based on our results, further investigations into the precise nature of this dichotomy are warranted.

Chapter 4

A Deterministic Model for Cancer Metastasis: Secondary Site

In Chapter 4, we present and analyze a simplified version of the model for *immune-mediated* metastasis developed in Chapter 3. Model simplifications are carried out in Section 4.1, reducing the system of 8 ODEs from Chapter 3 to a system of 3 ODEs, thereby allowing for further analysis in Section 4.2. Analytical results include proofs for the positivity and boundedness of model solutions; together with a quasi-steady state analysis showing that the system of 3 ODEs is governed by a single ODE in certain parameter regimes. Explicit conditions for metastatic extinction are derived and bifurcation analysis reveals the possibility of metastatic dormancy. Numerical simulations of the model are presented in Section 4.3, beginning with parameter estimation and a sensitivity analysis, followed by simulations of treatments, including primary tumor resection and immunotherapy. A discussion of our results and concluding remarks are made in Section 4.4.

4.1 The Model

This section reduces the 8 ODE model (Equations (3.6)) from Chapter 3 to allow for more rigorous mathematical analysis. We begin by making a number of observations concerning the model that was the focus of the previous chapter:

1. The two sites are nearly decoupled from each other: the primary site is unaffected by the dynamics at the secondary site, and the only effects of the primary site on the secondary site are through the arrival of shed cancer cells or TE immune cells.
2. When the FDSS is stable (Figure 3.6), the tumor population at the primary site reaches steady state before a single tumor cell is established at the secondary site.
3. The effects of the necrotic cells are on CT immune cell recruitment and secondary establishment. CT immune cells are also recruited by the tumor cells, and secondary establishment is also promoted by TE immune cells.
4. TE immune cells act to both promote tumor establishment and growth, and prevent tumor cell death.

Observations 1 and 2 allow us to consider only the secondary site and view the primary site as a source of cancer and TE immune cells, thereby reducing the number of equations in our model from 8 to 4. We can reduce the model by one more equation by virtue of observation 3 — because the two roles played by necrotic cells are also played by other cell types. These reductions leave us with a 3 ODE model consisting of equations for tumor cells, u , CT immune cells, x , and TE immune cells, y , at a secondary tumor site. Finally, as noted in observation 4, pro-tumor effects of the TE immune cells are two-fold. In order to better distinguish between the anti-tumor effects of CT immune cells and pro-tumor effects of TE immune cells, the TE immune dependence is dropped from the tumor cell death rate function, $\sigma(x, y) = \sigma(x)$. The inhibitory effect of TE immune cells on the tumor cell death rate is still

indirectly included in the model thanks to the education term: education increases the TE population at the detriment of the CT population resulting in an overall decrease in the tumor cell death rate. For the purposes of this model, the explicit dependence of σ on x is sufficient.

Observation 4 suggests that dropping the tumor death rate dependency on TE immune cells is reasonable, as the education of CT immune cells will deplete the CT immune population thereby decreasing the death rate — additional, explicit dependence on TE immune cells is therefore unnecessary. Under these simplifying assumptions, we arrive at the following *reduced* model for tumor-immune interactions at a metastatic site:

$$\begin{aligned}
\frac{du}{dt} &= \underbrace{\gamma(y)\phi(t)}_{\text{arrival}} + \underbrace{\gamma(y)g(u)u}_{\text{growth}} - \underbrace{\sigma(x)u}_{\text{death}} \\
\frac{dx}{dt} &= \underbrace{\alpha}_{\text{influx}} + \underbrace{\lambda(u)x}_{\text{growth}} - \underbrace{\rho ux}_{\text{tumor interaction}} - \underbrace{\omega x}_{\text{death}} - \underbrace{ed(u)x}_{\text{tumor education}} \\
\frac{dy}{dt} &= \underbrace{q\psi(t)}_{\text{arrival}} + \underbrace{ed(u)x}_{\text{tumor education}} + \underbrace{f(u)y}_{\text{growth}} - \underbrace{\tau y}_{\text{death}}
\end{aligned} \tag{4.1}$$

where $u(t)$, $x(t)$, and $y(t)$ denote the tumor, CT immune, and TE immune populations at the secondary site at time t . Those coefficients that are in both the simplified and the original model are as described in Section 3.1. The parameters $\phi(t)$, $\psi(t)$, and q are new for this model, and so will be described in further detail.

The function $\phi(t)$ denotes the rate of successful arrival and establishment of CTCs at the secondary site. $\phi(t)$ replaces the term s_1u_1 from the previous model (3.6). We allow the establishment rate to depend on time to reflect the theory that metastatic shedding is proportional to primary tumor size [62] which is highly dependent on time. For ease, we assume that $\phi(t)$ is constant in the analysis and numerical results presented below. To model the PMN, which provides CTCs with a supportive environment in which to settle and grow, we have scaled the establishment rate, $\phi(t)$, by an increasing

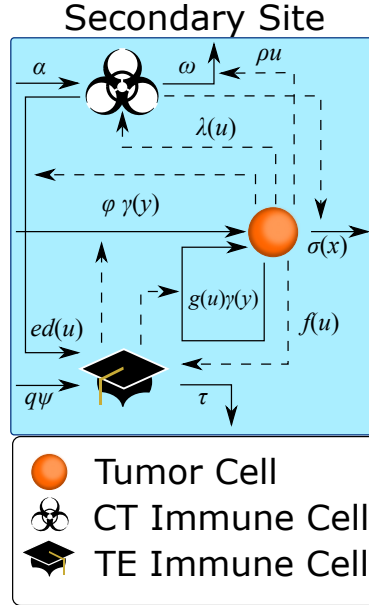


Figure 4.1: Cartoon model of the 3 ODE model of metastasis (4.1). Arrows indicate *positive* effects, and flat ends indicate *inhibitory* effects. Solid lines represent *direct* effects and dashed lines denote *indirect* influence. See text for details.

enhancement function, $\gamma(y)$. For simplicity, we have assumed the same TE *enhancement* effect for both settlement of CTCs as well as growth of the established tumor. The function $\psi(t)$ plays much the same role as $\phi(t)$, but in relation to the arrival of TE immune cells that have been disseminated from the primary tumor. TE immune cells successfully make the journey from primary to metastatic sites with probability q .

In contrast to the previous model 3.6, we have assumed that tumor cell death depends only on CT immune cells. This choice was made in order to prevent over-accounting for the effects of TE immune cells. Moreover, we no longer assume that ‘tumor cells’ are CSCs, rather that $u(t)$ denotes a general tumor cell population. Based on this assumption, we choose the tumor cell death rate, $\sigma(x)$, to be a strictly positive, decreasing function of the CT immune population, x .

All parameters are assumed to be positive, and the functional coefficients are assumed to have the following behavior:

Assumptions (A4.1):

- $\gamma(y)$: increasing from $\gamma(0) = 1$ to a finite, maximum value as $y \rightarrow \infty$.
- $g(u)$: decreasing, non-negative function with a value, $K > 0$, such that $\forall u \geq K$ we have $g(u) = 0$.
- $\sigma(x)$: decreasing, strictly positive function.
- $\lambda(u)$ and $f(u)$: increasing, bounded functions which evaluate to 0 when $u = 0$.
- $ed(u)$: increasing function with $ed(0) = 0$.
- $\phi(t)$ and $\psi(t)$: non-negative and bounded.

For full biological motivation of the above choices, consult the detailed discussion in Section 3.1.

In the following analysis, we often consider two cases: the case when a primary tumor exists at some distant location ($\phi > 0$ and $\psi > 0$), and the case when the primary tumor no longer exists ($\phi = 0$ and $\psi = 0$) to model therapy applied to the primary tumor.

4.2 Analytical Results

The goal of this section is to determine if treatment of the primary tumor can result in abscopal effects at the secondary site, and of what these effects might consist. We use ideas from geometric singular perturbation theory [69] to perform quasi-steady state approximation of the model. Stability and bifurcation analysis are then performed on the approximate model, providing threshold tumor densities that predict disease extinction or persistence in the case that the source term, ϕ , is zero. We begin with some preliminary results.

4.2.1 Positivity and Boundedness

Non-negative, bounded solutions to our model are required in order that they be biologically realistic. The following lemmas guarantee positivity and bound-

edness of our model solutions.

Lemma 5. *Given non-negative initial data, (u_0, x_0, y_0) , the solutions to 4.1 remain non-negative. In other words, the domain $\Omega = [0, \infty)^3$ is positively invariant.*

Proof. We show that along the coordinate axes the solutions flow *into* Ω . Once this is shown, it follows that if solutions approach the boundary, $\partial\Omega$, they will not *pass through* the boundary. The result follows.

Along the u -axis:

In this case, $u \geq 0$ but we have zero immune presence. Substituting $(u, x, y) = (u, 0, 0)$ into the equations 4.1 and using the assumptions (A4.1) we arrive at

$$\begin{aligned}\frac{du}{dt} &= \phi(t) + u(g(u) - \sigma_{max}) \\ \frac{dx}{dt} &= \alpha > 0 \\ \frac{dy}{dt} &= q\psi(t) > 0.\end{aligned}$$

In particular, the final two equations guarantee that the vector field is pointed toward the interior of Ω .

Along the x -axis:

In this case, we have $x \geq 0$ and $u = 0 = y$. The governing equations in this case read

$$\begin{aligned}\frac{du}{dt} &= \phi(t)\gamma(y) > 0 \\ \frac{dx}{dt} &= \alpha - \omega x \\ \frac{dy}{dt} &= q\psi(t) > 0.\end{aligned}$$

Here again, because the tumor and TE immune populations are increasing along the x -axis, we see solutions that start along the x -axis flow into Ω .

Along the y -axis:

In this case, we have $y \geq 0$ and $u = 0 = x$. The governing equations in this

case read

$$\begin{aligned}\frac{du}{dt} &= \phi(t) > 0 \\ \frac{dx}{dt} &= \alpha > 0 \\ \frac{dy}{dt} &= q\psi(t) - \tau y.\end{aligned}$$

Because the tumor and CT immune populations are increasing along the x -axis, we see solutions that start along the x -axis flow into Ω . \square

For boundedness, we require a few assumptions. In preparation, set

$$\begin{aligned}\sigma_{max} &= \max_{x \geq 0} \sigma(x) \\ \gamma_{max} &= \max_{y \geq 0} \gamma(y) \\ \lambda_{max} &= \max_{u \geq 0} \lambda(u) \\ \phi_{max} &= \max_{t \geq 0} \phi(t) \\ \psi_{max} &= \max_{t \geq 0} \psi(t).\end{aligned}$$

All of the above extrema exist under the assumptions (A4.1).

Lemma 6. *Assume that both $\lambda_{max} < \omega$ and $f_{max} < \tau$. Then the solutions to equations 4.1 are bounded for all times.*

Proof. We first consider the u equation. Suppose that $u \geq K$. Then, from (A4.1), $g(u) = 0$, and so the equation governing the evolution of u reads

$$\frac{du}{dt} = \phi\gamma(y) - \sigma(x)u.$$

It follows that u will be decreasing whenever

$$\phi\gamma(y) < \sigma(x)u.$$

By the positivity of $\sigma(x)$ (A4.1), we can isolate

$$u > \phi \frac{\gamma(y)}{\sigma(x)}.$$

By the boundedness of our functional coefficients, we see that

$$\phi(t) \frac{\gamma(y)}{\sigma(x)} < \phi_{max} \frac{\gamma_{max}}{\sigma_{min}} < \infty.$$

Then, for

$$u > \max \left\{ \phi_{max} \frac{\gamma_{max}}{\sigma_{min}}, K \right\},$$

u will be decreasing, and hence u is bounded.

Next, we consider the x equation. By the first step, we know that u is bounded,

$$0 \leq u \leq u_{max} < \infty.$$

This implies that

1. $0 \leq \lambda(u_{max}) \leq \lambda_{max}$,
2. $0 \leq \rho u \leq \rho u_{max}$, and
3. $0 \leq ed(u) \leq ed(u_{max})$.

Multiplying 2 and 3 by -1 , adding the resulting inequalities to 1, and subtracting $\omega > 0$ gives us

$$A := -\rho u_{max} - ed(u_{max}) - \omega \leq \lambda(u) - \rho u - \omega - ed(u) \leq \lambda_{max} - \omega =: B < 0,$$

where the final inequality is by the assumption of the lemma. Therefore, we have an upperbound on the ODE governing the x dynamics,

$$\alpha + Ax \leq \frac{dx}{dt} \leq \alpha + Bx$$

where $B < 0$. It is easy to see that the ODE

$$\frac{d\tilde{x}}{dt} = \alpha + B\tilde{x}$$

has a single, positive (as $B < 0$) steady state, $\tilde{x}^* > 0$, and that $\frac{d\tilde{x}}{dt} > 0$ whenever $\tilde{x} < \tilde{x}^*$ and $\frac{d\tilde{x}}{dt} < 0$ whenever $\tilde{x} > \tilde{x}^*$. Therefore, \tilde{x} is bounded, and as $\frac{dx}{dt} \leq \frac{d\tilde{x}}{dt}$, we conclude that x is also bounded.

Using the boundedness of both u and x allows us to reduce the y equation to a similar ODE as in the x case, yielding

$$\frac{dy}{dt} \leq (q\psi_{max} + ed(u_{max})x_{max}) + (f(u_{max}) - \tau)y =: C + Dy,$$

where $C > 0$ and $D < 0$ by the assumption of the lemma. Arguing similarly, we conclude that y is also bounded. □

From this point forward, we will make the **assumption** (A4.2) that both

$$\lambda_{max} < \omega \text{ and } f_{max} < \tau$$

in order to assure that our dynamics are bounded. We also note that these assumptions guarantee that both $\lambda(u) - \rho u - \omega - ed(u) < 0$ and $f(u) - \tau < 0$ for all values of u . We now proceed to determine the steady states of the model 4.1.

4.2.2 Steady States

For simplicity, assume that the source terms, $\phi(t)$ and $\psi(t)$, are simply constants, ϕ and ψ , respectively. Setting the model equations to zero gives us

$$\begin{aligned} 0 &= \gamma(y)\phi + \gamma(y)g(u)u - \sigma(x)u \\ 0 &= \alpha + \lambda(u)x - \rho ux - \omega x - ed(u)x \\ 0 &= q\psi + ed(u)x + f(u)y - \tau y. \end{aligned} \tag{4.2}$$

Two cases are considered.

Case: $\phi \neq 0$ and $\psi \neq 0$

First, note that if $\gamma(y)g(u) = \sigma(x)$, then the first equation in 4.2 reads

$$0 = \gamma(y)\phi > 0,$$

which is impossible. Therefore, we cannot have $\gamma(y)g(u) = \sigma(x)$ hold at the same time as the first equality in 4.2. This allows us to solve for the u nullcline,

$$u = \frac{\phi\gamma(y)}{\sigma(x) - \gamma(y)g(u)}.$$

Note that in order for this surface to remain non-negative, we require that the denominator satisfy $\sigma(x) - \gamma(y)g(u) > 0$. Similarly, the assumption (A4.2) allows us to solve the x and y equations in 4.2 explicitly, giving the nullclines

$$x = \frac{\alpha}{-(\lambda(u) - \rho u - \omega - ed(u))} > 0$$

and

$$y = \frac{q\psi + ed(u)x}{f(u) - \tau} > 0.$$

Steady states will be points, $(\bar{u}, \bar{x}, \bar{y})$, which lie on all three of the above nullclines. The number of such solutions is not immediately obvious, and depends on the choice of functional parameters. Note that tumor extinction is impossible in this case — assuming that a source of tumor cells exists, the model predicts the persistence of metastatic disease.

Case: $\phi = 0$ and $\psi = 0$

In this case, the first equation in 4.2 reduces to

$$0 = (\gamma(y)g(u) - \sigma(x))u,$$

which has two potential solutions: the trivial solution, $u = 0$, and the non-trivial solution defined by the equation $\gamma(y)g(u) = \sigma(x)$. As before, the number of solutions to this equation is not immediately obvious, but further exploration of this question is done at a later point. While the x nullcline does

not change from the previous case, the y nullcline decreases in magnitude to

$$y = \frac{ed(u)x}{f(u) - \tau} > 0.$$

Subcase: $u = 0$

Based on the assumptions (A4.1), we see that the x nullcline evaluated at $u = 0$ reduces to

$$x = \frac{\alpha}{\omega},$$

and the y nullcline evaluated at these two points gives $y = 0$. Consequently, we have found an *extinction* steady state,

$$(u_{ext}, x_{ext}, y_{ext}) = (0, \frac{\alpha}{\omega}, 0).$$

Note that this steady state is similar to the DFSS 3.12 from Chapter 3.

Subcase: $u \neq 0$

Then our steady state value(s) , $(\tilde{u}, \tilde{x}, \tilde{y})$, satisfy

$$\begin{aligned} \gamma(\tilde{y})g(\tilde{u}) &= \sigma(\tilde{x}) \\ \tilde{x} &= \frac{\alpha}{-(\lambda(\tilde{u}) - \rho\tilde{u} - \omega - ed(\tilde{u}))} \\ \tilde{y} &= \frac{ed(\tilde{u})\tilde{x}}{f(\tilde{u}) - \tau}. \end{aligned} \tag{4.3}$$

In summary, we have three potential defining equations for steady states, depending on the value of the source terms ϕ and ψ : a full-disease state, $(\bar{u}, \bar{x}, \bar{y})$, a disease-free state, $(u_{ext}, x_{ext}, y_{ext})$, and a *persistent* disease state, $(\tilde{u}, \tilde{x}, \tilde{y})$. As in Chapter 3, we now consider the stability of the disease-free state.

Proposition 2. *Assume that $\phi = 0 = \psi$ and that $g(0) = g_0 < \sigma(\frac{\alpha}{\omega})$. Then the disease-free state, $(0, \frac{\alpha}{\omega}, 0)$, is stable.*

Proof. We compute the Jacobian for the system 4.1 as

$$J = \begin{pmatrix} J_{1,1} & J_{1,2} & J_{1,3} \\ J_{2,1} & J_{2,2} & 0 \\ J_{3,1} & J_{3,2} & J_{3,3} \end{pmatrix}, \tag{4.4}$$

where

- $J_{1,1} = \gamma(y)g(u) + \gamma(y)g'(u)u - \sigma(x)$,
- $J_{1,2} = -\sigma'(x)u$,
- $J_{1,3} = \gamma'(y)(g(u)u + \phi)$,
- $J_{2,1} = \lambda'(u)x - \rho x - ed'(u)x$,
- $J_{2,2} = \lambda(u) - \rho u - \omega - ed(u)$,
- $J_{3,1} = ed'(u)x + f'(u)y$,
- $J_{3,2} = ed(u)$,
- $J_{3,3} = f(u) - \tau$.

Evaluating J at $(u, x, y) = (0, \frac{\alpha}{\omega}, 0)$ with $\phi = 0 = \psi$ gives us

$$\begin{pmatrix} g_0 - \sigma(\frac{\alpha}{\omega}) & 0 & 0 \\ \frac{\alpha}{\omega}(\lambda'(0) - \rho - ed'(0)) & -\omega & 0 \\ \frac{\alpha}{\omega}ed'(0) & 0 & -\tau \end{pmatrix},$$

whose diagonal entries are its eigenvalues. Under the assumption of the proposition, we see that all the eigenvalues are negative, and therefore the extinction state is stable. \square

The stability of the steady states $(\bar{u}, \bar{x}, \bar{y})$ and $(\tilde{u}, \tilde{x}, \tilde{y})$ are treated in greater detail in Section 4.2.4.

Remark: Role of TE Immune Cells

In the context of metastatic cancer, we might reasonably expect that metastases would die out assuming we could successfully remove the primary tumor in the very early stages of disease progression. On the other hand, removal of the primary tumor in the late stages of disease progression should not eradicate metastatic disease. Translated to the language of our model, we would like for the stability of both the extinction and the non-trivial steady states

to be possible in the case that $\phi = 0 = \psi$. In order to appreciate the effects of the TE immune cell population, assume that we have no TE immune cells. Without TE immune cells, and with $\phi = 0 = \psi$, our model then reduces to a slightly generalized version of the Kuznetsov model [91]. A non-trivial steady state will exist if a solution exists to the equation

$$g(\tilde{u}) = \sigma(\tilde{x}). \quad (4.5)$$

In particular, such a solution is only possible if $\sigma(\tilde{x}) \in [0, g_0]$. alternatively, for the extinction steady state to be stable, we require that $g_0 < \sigma(\frac{\alpha}{\omega})$. Because σ is an increasing function, if we assume that the steady state $\tilde{x} > \frac{\alpha}{\omega}$, (which is biologically reasonable, as the tumor microenvironment is highly populated with immune cells — see Chapter 1 and [42] for example) simultaneous existence of the non-trivial steady state and stability of the extinction state requires

$$g_0 < \sigma\left(\frac{\alpha}{\omega}\right) < \sigma(\tilde{x}) < g_0,$$

which is impossible. However, re-introducing the TE immune cells changes the condition (4.5) for the non-trivial steady state to

$$g(\tilde{u}) = \frac{\sigma(\tilde{x})}{\gamma(\tilde{y})}.$$

Assuming that $\tilde{y} > 0$, we have $\gamma(\tilde{y}) > 1$, thereby allowing us to choose parameters so that

$$\frac{\sigma(\tilde{x})}{\gamma(\tilde{y})} < g_0 < \sigma(\tilde{x}),$$

guaranteeing the existence of a biologically realistic, non-trivial steady state at the same time that extinction is stable.

We note that the bistability we have described here *is* possible in the Kuznetsov model (see Figure 5(d) in [91]), but requires that $\tilde{x} < \frac{\alpha}{\omega}$, which may not be biologically sound. We also note that in the TE version of the model, the CT immune cell steady state may satisfy $\tilde{x} < \frac{\alpha}{\omega}$ because of the effects of tumor education.

4.2.3 Quasi-Steady State Analysis: Fast Tumor, Slow Immune

In the following two sections, we assume relative magnitudes of the model parameters in order to perform quasi-steady state analysis of the model using methods from geometric singular perturbation theory [69]. In this section, we assume that the tumor dynamics are *fast* relative to those of the immune system, and in the following section we consider the opposite case.

In order to perform the analysis, we bring the model 4.1 into a convenient form. Let $U = u$, $V = (x, y)$, and $Z = (u, x, y)$. With this notation, our model (4.1) can be written as

$$\begin{aligned}\frac{dU}{dt} &= F(Z; \epsilon) \\ \frac{dV}{dt} &= \hat{G}(Z; \epsilon),\end{aligned}\tag{4.6}$$

where

$$\begin{aligned}F(Z; \epsilon) &= \gamma(y)(g(u)u + \phi) - \sigma(x)u \\ &= \gamma(y)(g(u)u + \hat{\phi}\epsilon) - \sigma(x)u \\ &= \frac{du}{dt}\end{aligned}$$

and

$$\begin{aligned}\hat{G}(Z; \epsilon) &= \begin{pmatrix} \alpha + \lambda(u)x - \rho ux - \omega x - ed(u)x \\ q\psi + ed(u)x + f(u)y - \tau y \end{pmatrix} \\ &= \begin{pmatrix} \hat{\alpha}\epsilon + \lambda(\hat{u})\epsilon x - \hat{\rho}\epsilon ux - \hat{\omega}\epsilon x - ed(\hat{u})\epsilon x \\ q\hat{\psi}\epsilon + ed(\hat{u})\epsilon x + f(\hat{u})\epsilon y - \hat{\tau}\epsilon y \end{pmatrix} \\ &= \begin{pmatrix} \frac{dx}{dt} \\ \frac{dy}{dt} \end{pmatrix} \\ &= \epsilon G(Z).\end{aligned}\tag{4.7}$$

Assuming that the tumor dynamics are *fast* relative to the immune dynamics, we can factor a small parameter, $0 < \epsilon \ll 1$, from the immune parameters,

resulting in the so-called ‘fast’ system [69]

$$\begin{aligned}\frac{dU}{dt} &= F(Z; \epsilon) \\ \frac{dV}{dt} &= \epsilon G(Z).\end{aligned}\tag{4.8}$$

With the change of variables $\hat{\tau} = \epsilon t$, we arrive at the associated ‘slow’ system [69]

$$\begin{aligned}\epsilon \frac{dU}{d\hat{\tau}} &= F(Z; \epsilon) \\ \frac{dV}{d\hat{\tau}} &= G(Z).\end{aligned}\tag{4.9}$$

The equations (4.8) and (4.9) are equivalent for $\epsilon > 0$, but we are most interested in studying the *reduced* systems that come from considering the limiting case $\epsilon \rightarrow 0$. Letting $\epsilon \rightarrow 0$ sees equations (4.8) and (4.9) become

$$\begin{aligned}\frac{dU}{dt} &= F(Z; 0) \\ \frac{dV}{dt} &= 0\end{aligned}\tag{4.10}$$

and

$$\begin{aligned}0 &= F(Z; 0) \\ \frac{dV}{d\hat{\tau}} &= G(Z; 0),\end{aligned}\tag{4.11}$$

respectively. Equations (4.10) and (4.11) make up the ‘reduced’ system. The object of interest in this section is the *slow manifold*,

$$\mathcal{M}_1 = \{Z \in \mathbb{R}^3 | F(Z; 0) = 0\},\tag{4.12}$$

which describes the U nullcline (when $\phi = 0$). In other words, on \mathcal{M}_1 , U is in steady state insofar that $\frac{dU}{dt} = 0$, meaning that changes in V (the immune population) result in (near) instantaneous changes in the U dynamics. Consequently, if the V dynamics are understood, then so too are the U dynamics [69, 82]. More precisely, we show that the slow manifold, \mathcal{M}_1 , can be written as a graph, $U = U(V)$. We also provide an explicit expression for \mathcal{M}_1 for

specific choices of functional parameters. Such a description of \mathcal{M}_1 allows us to reduce the system of 3 ODEs to a system of 2 ODEs, with the dynamics organized by \mathcal{M}_1 .

Theorem 5. *Assume that $\gamma(y)g_0 > \sigma(x)$. Then we can write \mathcal{M}_1 as a graph, $U = U(V)$.*

Proof. \mathcal{M}_1 is defined by the equation

$$F(Z; 0) = \gamma(y)g(u)u - \sigma(x)u = 0,$$

which can be expressed as

$$\gamma(y)g(u)u = \sigma(x)u. \quad (4.13)$$

Note that if $u = 0$, (4.13) is trivially satisfied. So, WLOG, we assume that $u > 0$ (Lemma 5). In this case, (4.13) reduces to

$$\gamma(y)g(u) = \sigma(x). \quad (4.14)$$

The RHS of (4.14) is positive and constant in u , while the LHS begins at $\gamma(y)g_0 > \sigma(x)$ and decreases to zero by $u = K$. Clearly, there is a unique solution, $u = u(x, y)$, to (4.14) for each fixed, non-negative value of x and y . The result follows. □

Next, we characterize the general behavior of the surface \mathcal{M}_1 .

Corollary 3. *The graph of \mathcal{M}_1 , $u = u(x, y)$, is such that $u_x < 0$ and $u_y > 0$.*

Proof. First, we show that $u_x < 0$. Differentiating both sides of (4.14) with respect to x gives

$$\begin{aligned} \frac{d}{dx}(\gamma(y)g(u(x, y))) &= \frac{d}{dx}(\sigma(x)) \\ \gamma(y)g'(u(x, y))u_x(x, y) &= \sigma'(x). \end{aligned}$$

By assumption, we know that $\gamma(y)g'(u(x, y)) < 0$ and $\sigma'(x) \geq 0$, so we can isolate

$$u_x(x, y) = \frac{\sigma'(x)}{\gamma(y)g'(u(x, y))} < 0 \quad (4.15)$$

as claimed. Similarly for the u_y result, we differentiate (4.14) with respect to y ,

$$\begin{aligned} \frac{d}{dy}(\gamma(y)g(u(x, y))) &= \frac{d}{dy}(\sigma(x)) \\ \gamma'(y)g(u(x, y)) + \gamma(y)g'(u(x, y))u_y(x, y) &= 0. \end{aligned}$$

Solving for u_y and using the assumptions (A4.1) gives

$$u_y(x, y) = \frac{-\gamma'(y)g(u(x, y))}{\gamma(y)g'(u(x, y))} > 0. \quad (4.16)$$

□

The final result in this section concerns the suitability of using geometric singular perturbation analysis in order to investigate the model, and relies on the following theorem due to Fenichel [69].

Theorem 6 (Fenichel). *Suppose $\mathcal{M}_0 \subseteq \mathcal{M}_1$ is compact, possibly with boundary, and normally hyperbolic, that is, the eigenvalues λ of the Jacobian $\frac{\partial F}{\partial U}$ all satisfy $\Re(\lambda) \neq 0$. Suppose F and G are smooth. Then for $\epsilon > 0$ and sufficiently small, there exists a manifold \mathcal{M}_ϵ , $\mathcal{O}(\epsilon)$ close and diffeomorphic to \mathcal{M}_0 that is locally invariant under the flow of the full problem (4.8).*

Note that by Lemma 6, our dynamics will take place over a bounded domain in \mathbb{R}^3 , and so the function $u = u(x, y)$ from Theorem 5 will be bounded and need only be considered over a bounded domain of \mathbb{R}^2 . Additionally, the continuity of $u(x, y)$ ensures that its image over a compact domain is itself compact. Therefore, $\mathcal{M}_1 \subseteq \mathbb{R}^3$ is compact.

We can also easily compute the Jacobian

$$\frac{\partial F}{\partial U} = \gamma(y)(g'(u)u + g(u)) - \sigma(x).$$

On \mathcal{M}_1 , (4.14) holds so that the above reduces to

$$\frac{\partial F}{\partial U} = \gamma(y)g'(u)u < 0$$

(assuming that $u > 0$). This means exactly that \mathcal{M}_1 is *normally hyperbolic* and so we have shown the following result:

Proposition 3. *For sufficiently small $\epsilon > 0$, the dynamics of the reduced system 4.11 on the slow manifold \mathcal{M}_1 provide a reasonable approximation (in the sense of Theorem 6) of the full system (4.9).*

The slow manifold, \mathcal{M}_1 , together with several solution trajectories is presented in Figure 4.2. The threshold functions $\gamma(y)$ and $\sigma(x)$ are responsible for the formation of 4 distinct regions of the surface. Regions I and IV correspond to a medium sized tumor when the effects of CT and TE immune cells balance each other, while TE immune effects dominate in region II, and CT immune effects dominate in region III. Biological interpretation of Figure 4.2 is provided in the discussion (Section 4.4).

We choose $g(u) = r(1 - \frac{u}{K})$. In this case, the slow manifold \mathcal{M}_1 is defined explicitly by the equation

$$u(x, y) = \frac{K(\gamma(y)r - \sigma(x))}{\gamma(y)r}. \quad (4.17)$$

4.2.4 Quasi-Steady State Analysis: Slow Tumor, Fast Immune

In this section, we assume instead that the dynamics of the tumor are slow relative to those of the immune system. This assumption is biologically reasonable, as immune dynamics — such as immune response to an injury — occur on the timescale of minutes or hours [113], whereas tumor dynamics, especially dormant metastases, can be on the timescale of years or even decades [64].

To begin, we reformulate the setting. As before, we have $U = u$, $V = (x, y)$, $Z = (u, x, y)$, and $0 < \epsilon \ll 1$, so that the model (4.1) can be written as in

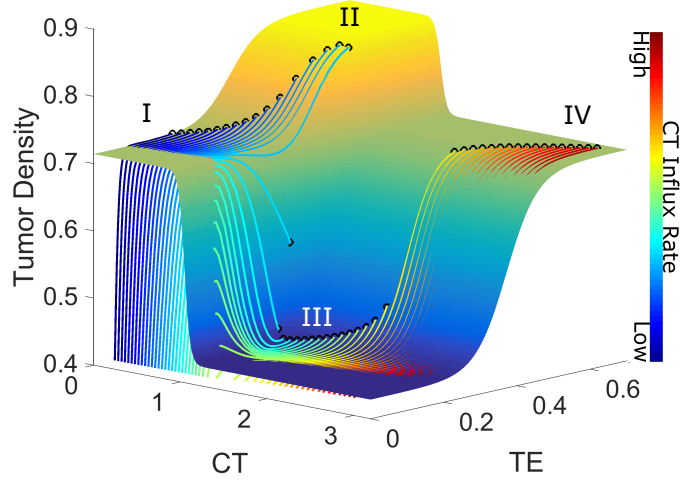


Figure 4.2: 2D slow manifold defined by equation (4.17) (surface) together with solution trajectories beginning at $(u_0, x_0, y_0) = (0, 0, 0)$ that differ only in the CT immune cell influx rate, α (increasing from blue to red). See Section 4.4 for interpretation.

(4.6). However, in this case assume that $g(u)$ and $\sigma(x)$ are of $\mathcal{O}(\epsilon)$ so that we can write

$$\begin{aligned}
 F(Z; \epsilon) &= \gamma(y)(g(u)u + \phi) - \sigma(x)u \\
 &= \gamma(y)(\epsilon\hat{g}(u)u + \hat{\phi}\epsilon) - \epsilon\hat{\sigma}(x)u \\
 &= \epsilon\hat{F}(Z) \\
 &= \frac{du}{dt}.
 \end{aligned}$$

We also assume that the coefficients in G are no longer of $\mathcal{O}(\epsilon)$, leaving us with

$$G(Z) = \begin{pmatrix} \alpha + \lambda(u)x - \rho ux - \omega x - ed(u)x \\ q\psi + ed(u)x + f(u)y - \tau y \end{pmatrix} = \begin{pmatrix} \frac{dx}{dt} \\ \frac{dy}{dt} \end{pmatrix}, \quad (4.18)$$

where G no longer depends on ϵ . Under these assumptions, we can write our model as the singular system (abusing notation and writing F for \hat{F} for simplicity)

$$\begin{aligned}\frac{dU}{dt} &= \epsilon F(Z; \epsilon) \\ \frac{dV}{dt} &= G(Z).\end{aligned}\tag{4.19}$$

As before, letting $\hat{\tau} = \epsilon t$ gives the associated ‘slow’ system

$$\begin{aligned}\frac{dU}{d\hat{\tau}} &= F(Z; \epsilon) \\ \epsilon \frac{dV}{d\hat{\tau}} &= G(Z).\end{aligned}\tag{4.20}$$

Letting $\epsilon \rightarrow 0$ gives the reduced system

$$\begin{aligned}\frac{dU}{dt} &= 0 \\ \frac{dV}{dt} &= G(z),\end{aligned}\tag{4.21}$$

and

$$\begin{aligned}\frac{dU}{d\hat{\tau}} &= F(Z) \\ 0 &= G(Z).\end{aligned}\tag{4.22}$$

The slow manifold in this case is defined by

$$\mathcal{M}_2 = \{Z \in \mathbb{R}^3 | G(Z) = 0\}.\tag{4.23}$$

Figure 4.3 shows a plot of the null surfaces defined by setting $\frac{du}{dt} = 0$ (purple), $\frac{dx}{dt} = 0$ (blue), and $\frac{dy}{dt} = 0$ (red). The intersection of the immune-related null surfaces defines the slow manifold \mathcal{M}_2 (green curve), while the intersections of all three surfaces (open circles) define the steady states of the system. We now provide a few results concerning the manifold \mathcal{M}_2 .

Lemma 7. *The manifold \mathcal{M}_2 is normally hyperbolic.*

Proof. We compute the Jacobian

$$\frac{\partial G}{\partial V}(Z) = \begin{pmatrix} \lambda(u) - \rho u - \omega - ed(u) & 0 \\ ed(u) & f(u) - \tau \end{pmatrix}\tag{4.24}$$

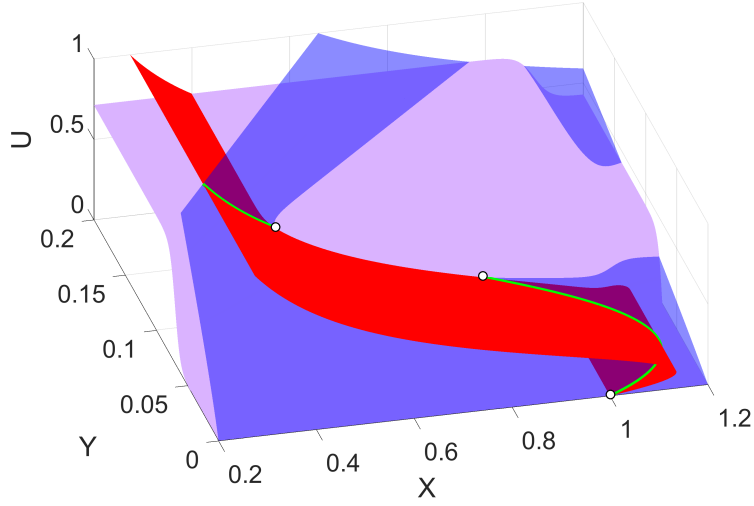


Figure 4.3: Null surfaces of the model (4.1). Blue is $\frac{dx}{dt} = 0$, red is $\frac{dy}{dt} = 0$ and purple is $\frac{du}{dt} = 0$. The slow manifold is the intersection between the x and y null surfaces, denoted by the green curve. Intersections of all three surfaces (denoted by circles) are steady states. Parameters as in Table 4.2, with the exception of $max_1 = 2.5$, $up_1 = 0.1$, $\phi = 0$, and $\psi = 0$.

and note that the diagonal entries are both negative as a consequence of assumptions (A4.2) ($\lambda_{max} < \omega$ and $f_{max} < \tau$). \square

Proposition 4. *We can write \mathcal{M}_2 as a graph, $(u, x, y) = (u, x(u), y(u))$.*

Proof. Fix $u \geq 0$. \mathcal{M}_2 is defined via $G(Z) = 0$. More explicitly, this means that both of the following equations hold:

$$\begin{aligned} 0 &= \alpha + \lambda(u)x - \rho ux - \omega x - ed(u)x \\ 0 &= q\psi + ed(u)x + f(u)y - \tau y. \end{aligned} \tag{4.25}$$

The assumptions (A4.2) allow us to solve the first expression explicitly for x , yielding

$$x = x(u) = \frac{\alpha}{-(\lambda(u) - \rho u - \omega - ed(u))} > 0, \tag{4.26}$$

which is an explicit expression for $x = x(u)$. Similarly for y , we can solve the

second equation in (4.25) in terms of u and x as

$$\begin{aligned} y &= \frac{q\psi + ed(u)x}{-(f(u) - \tau)} \\ &= \frac{q\psi + ed(u)x(u)}{-(f(u) - \tau)} > 0, \end{aligned} \tag{4.27}$$

thereby giving us an explicit expression $y = y(u)$. \square

Combining the previous proposition together with the boundedness of our system, we conclude, as in the previous section, that $\mathcal{M}_2 \subseteq \mathbb{R}^3$ is compact and we can use Fenichel to arrive at the following result.

Theorem 7. *For sufficiently small $\epsilon > 0$, the dynamics of the reduced system 4.22 on the slow manifold \mathcal{M}_2 provide a reasonable approximation (in the sense of Theorem 6) of the full system 4.20.*

Therefore, to understand the dynamics of the full system, we need only investigate the dynamics of the reduced system. In order to obtain explicit characterizations of the dynamics along \mathcal{M}_2 , we will now choose specific forms for our functional parameters.

The choices of functional coefficients in this chapter are similar to the choices made in Chapter 3. We briefly outline the choices below:

- Tumor growth,

$$g(u) = r \left(1 - \frac{u}{K} \right),$$

where r denotes an intrinsic growth rate, and K is a carrying capacity.

- TE immune cell enhancement of tumor growth,

$$\gamma(y) = \nu(y; \min_1, \max_1, \text{low}_1, \text{up}_1),$$

where ν is as defined by equation (3.8), and where $\min_1 = 1$.

- Tumor cell death rate,

$$\sigma(x) = \xi(x; \min_2, \max_2, \text{low}_2, \text{up}_2),$$

where ξ is defined by the equation (3.9).

- CT (TE) immune cell recruitment mediated by the tumor density,

$$\lambda(u) = \frac{a_1 u}{b_1 + u},$$

and

$$f(u) = \frac{a_2 u}{b_2 + u},$$

repectively.

- Tumor education of CT immune cells,

$$ed(u) = \chi u.$$

For a full explanation of all the model parameters, their meaning, and justification of the model, we refer the reader to the detailed descriptions in Section 3.1.

Having made the above choices for functional coefficients in our model, we arrive at the following description of the dynamics along the slow manifold \mathcal{M}_2 in terms of the derivatives $x_u = \frac{\partial x}{\partial u}$ and $y_u = \frac{\partial y}{\partial u}$, where $x(u)$ and $y(u)$ are as in (4.25) and (4.27), respectively.

Proposition 5. $x_u > 0$ for $u < u_+$ and $x_u < 0$ for $u > u_+$, where

$$u_+ = -b_1 + \sqrt{\frac{a_1 b_1}{\rho + \chi}}.$$

Additionally, $y_u > 0$ for all $0 \leq u \leq K$.

Proof. We compute the derivatives $x_u(u)$ and $y_u(u)$. We begin with x_u :

$$\begin{aligned} x_u(u) &= \partial_u \left(\frac{\alpha}{-(\lambda(u) - \rho u - \omega - ed(u))} \right) \\ &= \frac{\alpha (\lambda'(u) - \rho - ed'(u))}{(\lambda(u) - \rho u - \omega - ed(u))^2}. \end{aligned} \tag{4.28}$$

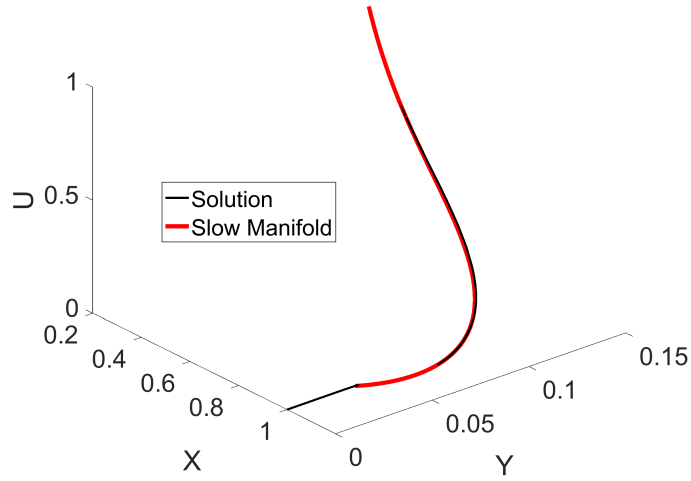


Figure 4.4: The slow manifold, \mathcal{M}_2 (red) and the solution to the system (4.1). Initial conditions $(u_0, x_0, y_0) = (0, 1, 0)$. Parameters as in Table 4.2.

The sign of x_u depends entirely on the sign of

$$\lambda'(u) - \rho - ed'(u).$$

With the choices we made for $\lambda(u)$ and $ed(u)$, we arrive at the following chain of equivalent conditions:

$$\begin{aligned} x_u(u) &> 0 \\ \lambda'(u) - \rho - ed'(u) &> 0 \\ \frac{a_1 b_1}{(b_1 + u)^2} - \rho - \chi &> 0 \\ \frac{a_1 b_1}{\rho + \chi} &> (b_1 + u)^2 \\ 0 &> u^2 + 2b_1 u + b_1^2 - \frac{a_1 b_1}{\rho + \chi}. \end{aligned} \tag{4.29}$$

The roots to the above quadratic are given by

$$u_{+,-} = -b_1 \pm \sqrt{\frac{a_1 b_1}{\rho + \chi}}. \quad (4.30)$$

This gives distinct, real roots (assuming that $a_1 b_1 \neq 0$) with at least one of them negative. If $u_+ > 0$, then we see that $x_u > 0$ for $u < u_+$ and negative otherwise. If $u_+ < 0$, then we simply have $x_u < 0$ for all non-negative u .

Next, we consider y_u . We show simply that y_u is non-negative, as

$$\begin{aligned} y_u(u) &= \partial_u \left(\frac{q\psi + ed(u)x(u)}{-(f(u) - \tau)} \right) \\ &= \frac{-(ed'(u)x(u) + ed(u)x_u(u))(f(u) - \tau) + (q\psi + ed(u)x(u))f'(u)}{(f(u) - \tau)^2} \\ &\geq \frac{-(ed'(u)x(u) + ed(u)x_u(u))(f(u) - \tau)}{(f(u) - \tau)^2}. \end{aligned} \quad (4.31)$$

The final inequality results from the fact that $(q\psi + ed(u)x(u))f'(u) \geq 0$ since f is increasing (A4.1). Now, we can use the expressions for $x(u)$ and x_u , as well as our choice of $ed(u) = \chi u$ to arrive at

$$\begin{aligned} (4.31) &= \left[\frac{\chi\alpha}{-(\lambda(u) - \rho u - \omega - ed(u))} + \frac{\chi u \alpha (\lambda'(u) - \rho - ed'(u))}{(\lambda(u) - \rho u - \omega - ed(u))^2} \right] (\tau - f(u)) \\ &= \frac{\chi\alpha}{-(\lambda(u) - \rho u - \omega - ed(u))} (\tau - f(u)) \left[1 - \frac{u(\lambda'(u) - \rho - ed'(u))}{\lambda(u) - \rho u - \omega - ed(u)} \right]. \end{aligned} \quad (4.32)$$

The sign of this expression depends only on the sign of the term

$$\left[1 - \frac{u(\lambda'(u) - \rho - ed'(u))}{\lambda(u) - \rho u - \omega - ed(u)} \right] = \frac{\lambda(u) - \omega - ed(u) - \lambda'(u)u + ed'(u)u}{\lambda(u) - \rho u - \omega - ed(u)}.$$

By assumption (A4.2), the denominator is always negative, and therefore the sign of the above expression is determined by the sign of its numerator. With the choices for $ed(u)$ and $\lambda(u)$ made above, the numerator simplifies to

$$\frac{u^2(a_1 - \omega) - 2b_1\omega u - \omega b_1^2}{(b_1 + u)^2}.$$

Using the fact that $a_1 - \omega < 0$ (A4.2) guarantees that the quadratic is negative for all $u \geq 0$, and therefore $y_u(u) \geq 0$ for all $u \geq 0$. \square

4.2.5 Number of Steady States and Bifurcation Analysis

In the situation of fast immune dynamics and slow tumor dynamics, Theorem 7 and Proposition 4 allow us to reduce the system of 3 ODEs in (4.1) to a single ODE in the tumor cell density, u ,

$$\frac{du}{dt} = \gamma(y(u))(g(u)u + \phi) - \sigma(x(u))u = H(u; \phi). \quad (4.33)$$

Consequently, the questions of number and stability of steady states reduce to the number of solutions to $H(u; \phi) = 0$ and the sign of H on either side of these solutions, respectively. In this section, we investigate the number of possible steady states as well as the possibility of bifurcations in the parameter $\phi \geq 0$, which have relevance to dynamics of metastatic disease upon treatment of the primary tumor.

While a full characterization of all possible steady states is not available at present, we provide a brief discussion of the problem itself, and observed behavior of the model.

Of interest is the number of solutions to

$$H(u; \phi) = \gamma(y(u))(g(u)u + \phi) - \sigma(x(u))u = 0.$$

We can evaluate $H(0; \phi) = \gamma(y(0))\phi > 0$. Note that the boundedness and positivity of σ and γ guarantee the existence of a sufficiently large value of u (call it u^*) such that $H(u^*; \phi) = \gamma(y(u^*))\phi - \sigma(x(u^*))u^* < 0$. Therefore, we always have at least one positive steady state, $u \in [0, u^*]$.

Furthermore, the behavior of $x(u)$ and $y(u)$ on the slow manifold \mathcal{M}_2 has been characterized (Proposition 5). Indeed, since $y(u)$ is increasing in u , and γ is an increasing function, we know that the term $\gamma(y(u))\phi$ is increasing in u . In contrast, because $g(u)$ is decreasing in u , the expression $\gamma(y(u))g(u)$

Parameter	1	2	3	4	5	6
max_1	2.5	2.5	2.5	1.5	0.2	0.2
low_1	—	—	—	0.5	—	—
up_1	0.095	0.095	—	0.95	0.095	0.095
min_2	9.085×10^{-6}	9.085×10^{-6}	—	9.085×10^{-5}	9.085×10^{-6}	9.085×10^{-6}
max_2	—	—	—	7.268×10^{-4}	—	—
low_2	0.2	0.2	—	7.268×10^{-4}	0.2	0.2
r	2.0×10^{-4}	2.0×10^{-4}	2.0×10^{-4}	8.0×10^{-4}	2.0×10^{-4}	2.0×10^{-4}
ϕ	1.25×10^{-6}	0	6.25×10^{-6}	0	5.0505×10^{-7}	0

Table 4.1: Model parameters used in Figure 4.5 that *differ* from those in Table 4.2.

may not be monotonic. We have determined that it begins at a positive value no smaller than g_0 and evaluates to zero for $u \geq K$. The exact behavior is rather complicated. Instead of a full analysis, we present a few cases in Figure 4.5 to show the richness of the possibilities. The parameter values used to generate the plots in Figure 4.5 are in Table 4.1, but we note that the presented parameter values are by no means the only ones capable of producing the number of steady states shown in Figure 4.5 (see Figure 4.7 for example). The final expression included in H is the death term, $\sigma(x(u))u$. While it is assumed that σ is decreasing, we know that x_u changes from positive to negative at the value u_+ . The exact dynamics of the term $\sigma(x(u))u$ therefore depend on the value of u_+ and the choice of σ . The details are left for future study.

For the specific choices of functional parameters we have made here, however, it is possible to see anywhere from 1 to 6 solutions to $H(u; \phi) = 0$ (as highlighted in Figure 4.5). These results are similar to those presented in [91], where they found that their model had at most 5 steady states. We also note that, based on the approximation results in Theorem 7, we can view the plots in Figure 4.5 as phase line diagrams. Consequently, the stability of the steady states are simply determined by the sign of $H(u; \phi)$ on either side of the root, u_* : if $H(u; \phi) > 0$ as $u \rightarrow u_*$ from the left, and $H(u; \phi) < 0$ as $u \rightarrow u_*$ from the right, then u_* is stable, otherwise it's unstable. These results are highlighted in Figures 4.5 and 4.6 using solid dots to denote stable steady states, and open dots to denote unstable steady states.

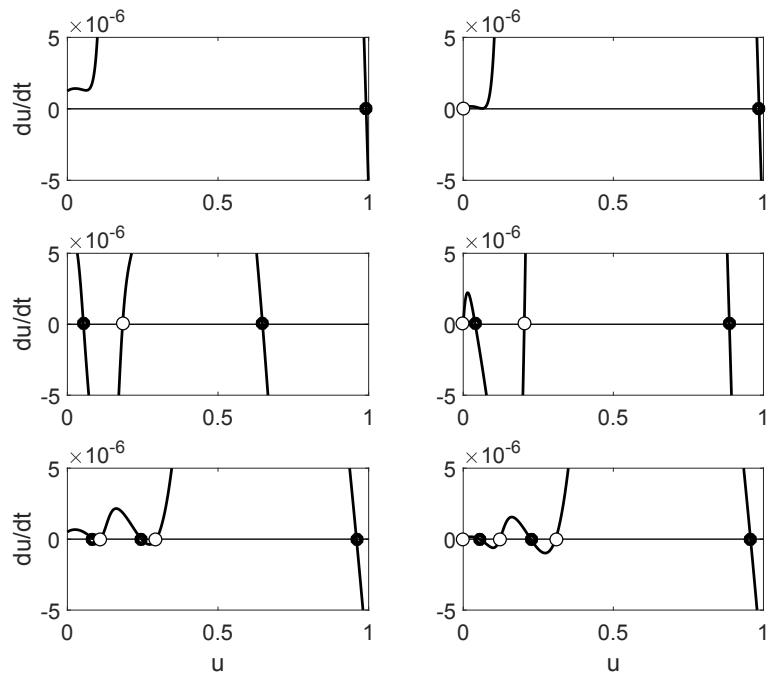


Figure 4.5: Phase line diagrams for the 1D system (4.33) showing possibilities for the number of steady states. Plots of $\frac{du}{dt} = H(u; \phi)$ resulting in 1, 2, 3, 4, 5, or 6 steady states — indicated by circles. Solid circles denote stable states and open circles denote unstable states. Parameters adjusted from those in Table 4.2 as indicated in Table 4.1.

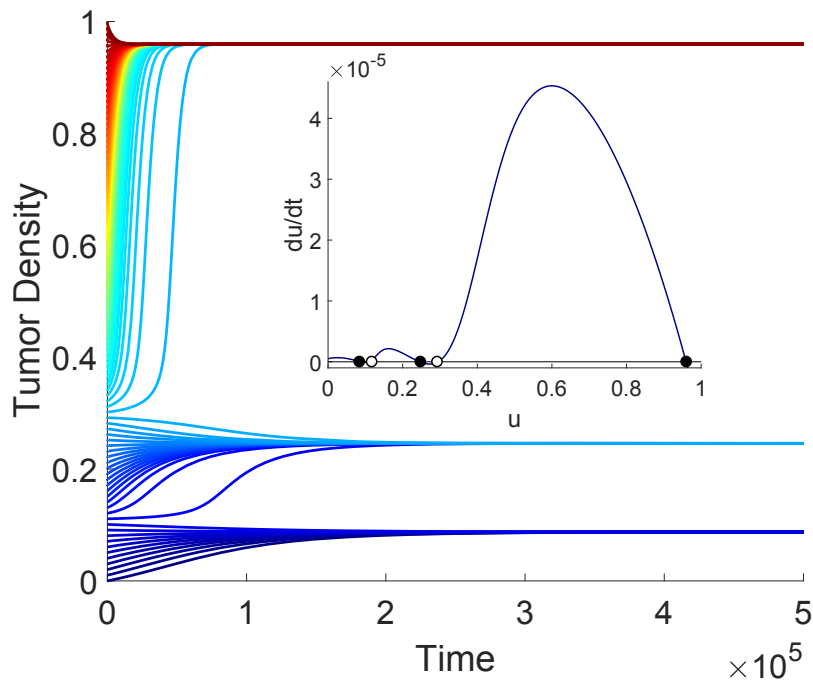


Figure 4.6: Solution trajectories for u for the system (4.1), with initial conditions varying between 0 and 1 (increasing from blue to red). Inset: the corresponding plot for $\frac{du}{dt}$ on the slow manifold \mathcal{M}_2 . Steady states are where $\frac{du}{dt} = 0$ and are denoted by circles. Open circles indicate unstable, while solid circles represent stable. Parameters as in Table 4.1 (5).

Confirmation of these approximation results are presented in Figure 4.6, where, in addition to the phase line diagram, we also plot solution trajectories for u for the full model (4.1) with varying initial conditions between 0 and 1 (increasing from blue to red). In the solution plots, the locations of stable and unstable steady states is clear, and the alignment with the phase line diagram is good, suggesting that our slow-manifold approximation is a reasonably accurate approximation of the dynamics of the full system (4.1).

Next, we consider bifurcations in the tumor cell source term, ϕ . With ϕ representing the rate of establishment at the secondary site, the role it plays in the dynamics is of great interest to treatment outcomes. Here we investigate the role of ϕ on the number of steady states in the model by varying ϕ around the base value reported in Table 4.2. Figure 4.7 shows the results of this

analysis for two values of the parameter max_1 , with the plot on the left made using the smaller value of max_1 . In both plots we see that for larger values of ϕ the model predicts a single stable steady state, corresponding to full metastatic disease. However, as we decrease ϕ , a new branch of steady states emerges. This emergence corresponds to the $\frac{du}{dt}$ curve hitting and then passing the origin (see, for example, Figure 4.10), creating one, then a pair of new solutions to $\frac{du}{dt} = 0$. Following the creation a new branch of steady states, there exists a range of values for ϕ in which bistability is possible (marked in blue). Although bistability is not continued to the origin in the case of a smaller max_1 (left), increasing the maximum value of the TE growth enhancement function allows us to extend this period of bistability to the origin, $\phi = 0$.

Relevant to treatment is the case $\phi = 0$. In the left plot, only the tumor-free state is stable (bottom branch), meaning that removal of the source ϕ will *always* result in disease extinction. In comparison, the right plot allows for bistability in the case $\phi = 0$, with the final outcome — disease extinction or persistence — governed by the location of the unstable steady state (saddle). The implications of this in the context of treatment are explored further in the following section (see Figure 4.10).

Finally, we note that we have only presented numerical results for a specific parameter regime, but given explicit choices for functional the functional coefficients — $\sigma(u)$, $ed(u)$, $f(u)$, $g(u)$, $\gamma(y)$, and $\sigma(x)$ — the analysis of the phase-line diagrams provides insight into the general behavior. Indeed, the process of appearing/disappearing steady states described above can be applied to the cases in which we have more than 3 steady states, as illustrated in Figure 4.5. The explanation of these bifurcations by way of the phase-line diagrams resulting from the quasi-steady state approximation of our full system demonstrates the effectiveness of this approach.

4.3 Numerical Results

In this section we perform numerical simulations of the model. We begin by obtaining a baseline set of parameters informed by the currently available

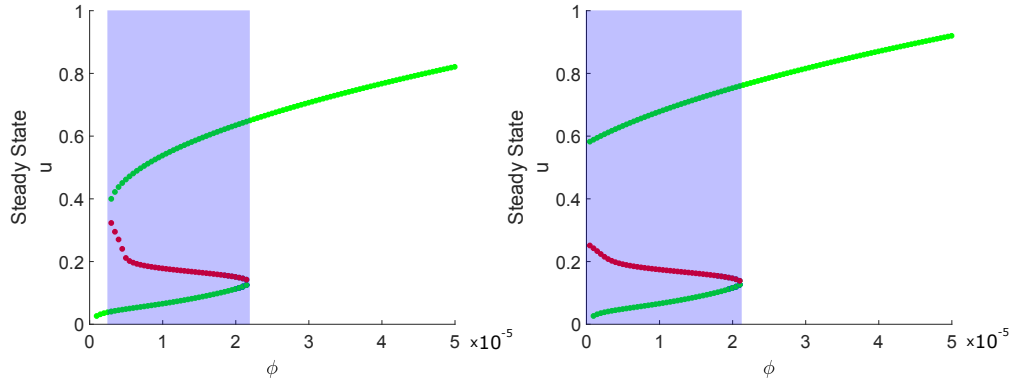


Figure 4.7: Steady state solutions to $H(u; \phi) = 0$ for varying values of ϕ . Green denotes stable and red denotes unstable. Left: parameters as in Table 4.2. Right: The value of max_1 increased to 2.5. Regions of bistability are in blue/violet. There are regions in both plots with 1, 2, or 3 steady states, demonstrating that the choices in Figure 4.5 and Table 4.1 are by no means unique.

literature where possible. Once we have obtained a set of baseline parameters, we perform a parameter sensitivity analysis in order to investigate the relative importance of the various model parameters on tumor density. We follow this analysis with the numerical simulation of various treatments, and explain the results in terms of the quasi-steady state analysis performed in the previous section.

4.3.1 Parameter Estimation

The choices of functional coefficients in this chapter are similar to the choices made in Chapter 3, and were outlined in the previous section. As in Chapter 3, parameter estimates were obtained from the literature when available, and informed choices were made when no such estimation was possible. For the baseline parameters presented in Table 4.2, the following assumptions have been made. We have chosen $K = 1$ for simplicity. The growth rate, r , was estimated by fitting a logistic growth curve to normalized tumor growth data from [112]. The parameters that our model shared with the Kuzntesov model [91] were estimated by using the dimensional parameters presented in [91] and non-dimensionalizing by assuming that the baseline CT immune and tumor

cell densities are 10^7 and 5×10^8 , respectively. The CT immune cell influx rate, α , was assumed as $\alpha = \omega$ in order to normalize the disease-free density of CT immune cells (this differs from Kuznetsov’s choice for α). In order for the slow manifold approximation to hold, we have increased the value of the immune parameters, and decreased the value of the tumor parameters — each by a factor of 10.

Threshold parameters have been estimated in the following way. Assuming that a tumor population initiates a CT immune response, and that the immune system can effectively activate and destroy sufficiently small tumors, we have chosen $low_2 = \frac{\alpha}{\omega} = 1$, and min_2 to be chosen such that upon primary tumor removal, the disease-free steady state is stable (i.e. $r < \sigma(\frac{\alpha}{\omega})$: see also Figure 4.7 (left)). The values of $up_{1,2}$, $max_{1,2}$, and low_1 were chosen in order to have the rates change in time (i.e. the thresholds were passed at least once).

Finally, the TE immune related parameters. The rate of tumor education of immune cells was informed by [34, 86], but also chosen so that the tumor density u_+ (see Proposition 5) was approximately 0.1. The growth and death parameters a_2 , b_2 , and τ were tuned from the Kuznetsov values to achieve a total immune population near the end of the simulation of approximately 1. The results of this estimation process are summarized in Table 4.2.

Using the parameters in Table 4.2 as our baseline parameters, we performed a basic parameter sensitivity analysis in order to determine the relative importance of the model parameters on the system outcome. A baseline solution for our tumor density, u , was obtained using the parameters in Table 4.2. For each model parameter, solutions were obtained for 30 different choices of the parameter value taken from the range $\pm 70\%$ of the baseline value. The value of 70% was chosen in order that the solutions to our system remained bounded. Among the solutions obtained for the various parameter values, the ones that differed *most* significantly from the baseline solution were reported. We reported the maximum differences because they show the most extreme results among the values tested and allows for meaningful comparisons between parameters. This process was done at three time points in Figure 4.8 — one *early* in disease progression, one in the *late-middle* stage of the disease, and a final time point when all solutions have reached steady state value — and at

Parameter	Description	Value	Units	References
r	tumor growth rate	1.82×10^{-4}	1/time	[91, 112]
K	tumor carrying capacity	1	density	—
min_1	min TE growth	1	—	—
max_1	max (increase) TE growth	1.48	—	—
low_1	growth activation	5×10^{-2}	density	—
up_1	growth saturation	0.2	density	—
ϕ	CTC arrival	2.5×10^{-5}	density/time	[137]
min_2	min death	1.82×10^{-4}	1/time	—
max_2	max (increase) death	1.82×10^{-4}	1/time	—
low_2	death activation	1	density	—
up_2	death saturation	1.2	density	—
α	CT immune influx rate	7.5×10^{-3}	density/time	[91]
a_1	CT expansion rate	2.26×10^{-2}	1/time	[91]
b_1	CT expansion damping	0.404	density	[91]
ρ	fatal immune-tumor interaction rate	3.11×10^{-2}	1/time	[91]
ω	CT decay rate	7.5×10^{-3}	1/time	[91]
χ	immune education rate	4.9×10^{-3}	1/time	[34, 86]
q	proportion successful TE	0.8	—	[19]
ψ	TE shedding	1×10^{-3}	density/time	[137]
a_2	TE expansion rate	1×10^{-2}	1/time	[91]
b_2	TE expansion damping	0.485	density	[91]
τ	TE decay rate	2.27×10^{-2}	1/time	[91]

Table 4.2: Model Parameters and the values used in presented simulations.

54 time points with time increments of two weeks in Figure 4.9 to highlight the effect of the different parameters in time.

In Figure 4.8 we present the maximum percentage change in tumor density at times $T = 14$ days (A), $T = 560$ days (B), and $T = 1484$ days (C). Red bars indicate that the observed change occurred as a result of *decreasing* the parameter of interest, while green bars indicate that an *increase* in that parameter was responsible for the observed change. There are two parameters that play a major role in tumor density at early times (A): the TE immune cell decay rate, τ , and the establishment rate of CTCs, ϕ . Decreasing τ results in a significant increase in the tumor density by allowing for a larger TE immune population at the metastatic site, thereby allowing for successful establishment and growth early in disease progression. On the other hand, increasing τ has little effect on the model dynamics. Not surprisingly when considering the biological context, ϕ is the most sensitive parameter at 14 days. Indeed, early growth of the metastatic tumor depends almost entirely on the source of cells from the primary site. Increasing (decreasing) the source of cells arriving at the secondary site can markedly increase (decrease) the early growth of the secondary tumor. At this early stage in the disease, the remaining parameters have a limited effect.

In contrast to the early effects, (B) shows that all the parameters have a noticeable sensitivity at the later time point. Although ϕ remains the most sensitive to cause a *decrease* in tumor density, it is no longer alone in having a significant effect. Indeed, the tumor growth rate, r , together with the minimum and maximum tumor cell death rates, min_2 and max_2 can also significantly decrease the tumor density at later times compared to baseline. Moreover, min_2 is the parameter responsible for the largest *increase* in tumor density compared to baseline. We also observe that TE immune parameters are better able to *increase* tumor density compared to CT immune parameters, while the opposite is true with respect to affecting a *decrease* in tumor density, where CT immune parameters are more sensitive than their TE immune counterparts.

By time $T = 1484$ days, the system has now settled at a steady state, and so (C) allows us to compare the effects of different parameters on steady

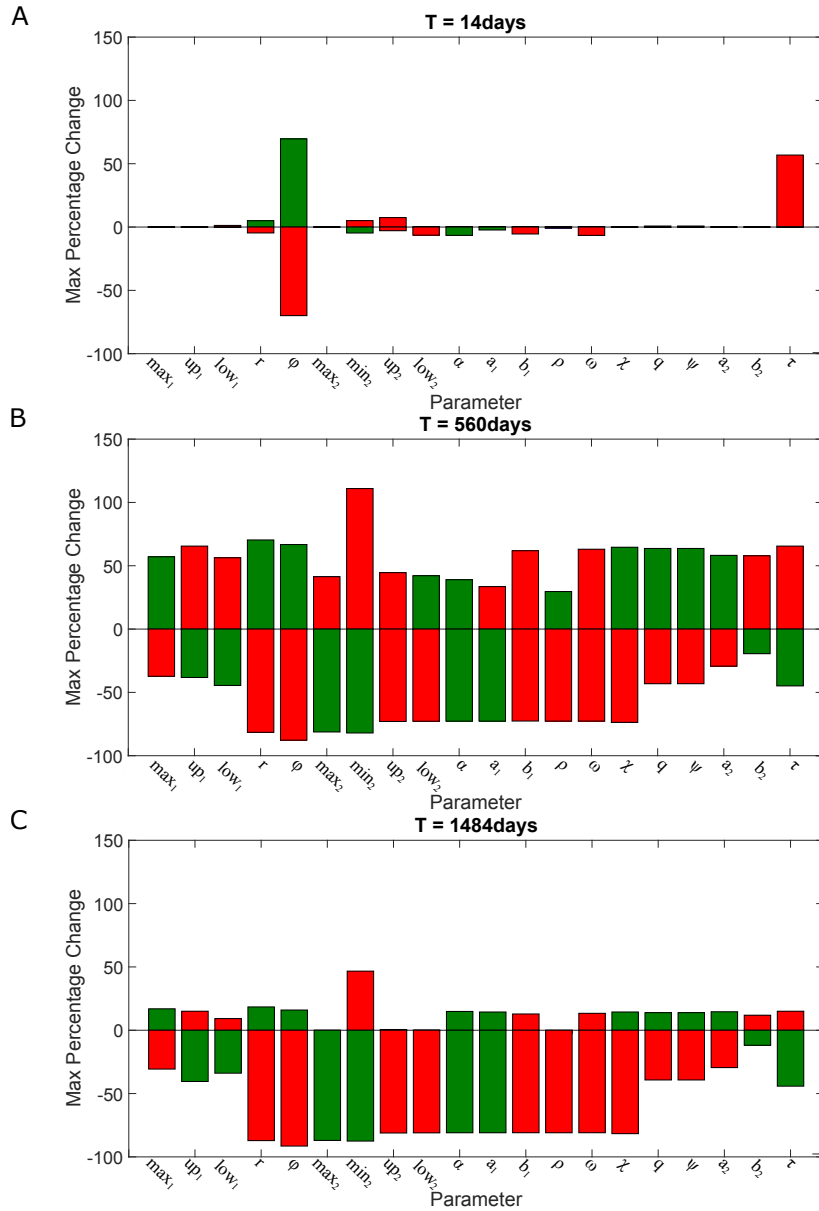


Figure 4.8: Maximum percentage change in tumor density compared to baseline at time $T = 14$ days, $T = 560$ days, and $T = 1484$ days. Red bars indicate that the resulting change in tumor density resulted from a *decreased* parameter value, while increased parameters are indicated by the green bars. Further details in the text.

state values. Decreasing the minimum tumor death rate, min_2 , results in the largest increase in steady state tumor size. Close behind are the growth parameters, r and max_1 , and the source term ϕ . We also note that increases in the CT immune influx rate or tumor-mediated recruitment rate result in larger tumors, but different increases to these same values also result in some of the smallest tumors. As was the case at time $T = 560$ days, the parameters capable of affecting the largest decrease in tumor size are the source term ϕ and the tumor growth rate, r .

Based on the stark difference between sensitivities at different time points, we performed the same sensitivity analysis at intervals of 2 weeks for 54 total observations (we also performed the same analysis for 107 2 week increments, but the plots looked similar to those presented here, and so are left out). Figure 4.9 shows the percentage increase (top) and decrease (bottom) for each of our model parameters (horizontal axis) over the course of 108 weeks (vertical axis). Percentages are indicated by the color bars. Consider first the top plot. Most of the parameters have similar effects progressing through time: increasing until a point of maximal influence, followed by a period of decreasing influence. What this pattern tells us is *when*, relative to the baseline solution, the growth is most influenced by the parameter of interest. Take the most sensitive parameter at large times, min_2 , as an example. For small times, we see little change from baseline. However, around the $t = 15$ (2 week increments) mark, we see the difference between baseline increase to a maximum of nearly 500% by $t = 25$. This period of increase reflects the fact that the baseline solution remains relatively unchanged over this period, whereas the perturbed solution is in a phase of rapid growth. The period of decreased effect compared to baseline (beginning at $t = 25$) is indicative of the perturbed system arriving at steady state, and the control system ‘catching up’. Finally, at long times when both solutions are in steady state, we see the effect of the parameter perturbation on the steady state (Figure 4.8 can be interpreted in this way). With this view, we can see that the effects of min_2 are relatively late in disease progression compared to τ or up_1 , but changes in min_2 result in the largest change in steady state value. We also note that ϕ is most sensitive for early times, and only results in a (relatively) modest increase in steady state value.

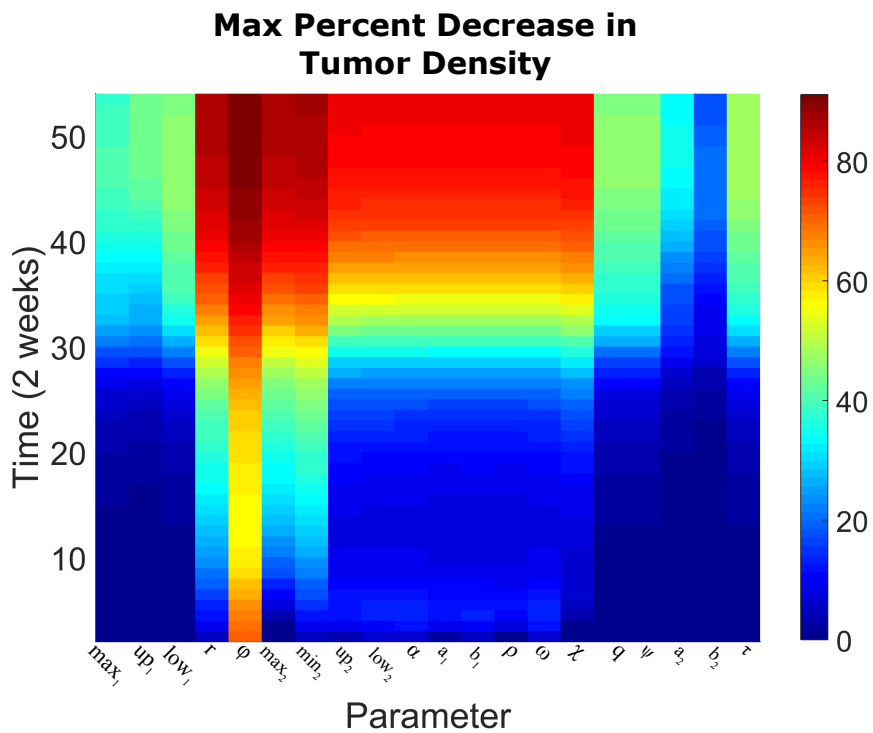
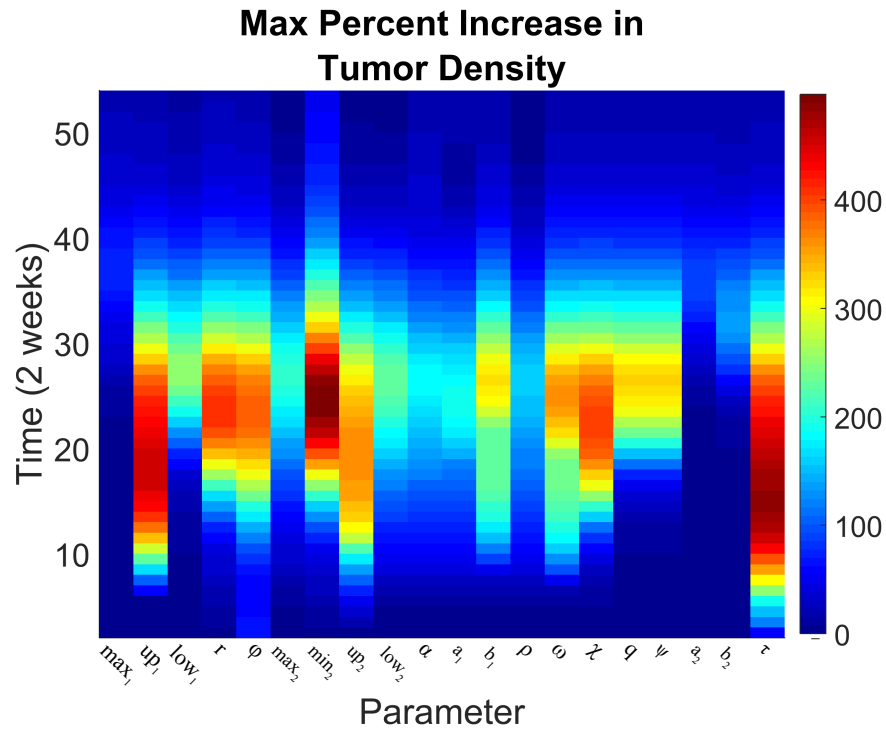


Figure 4.9: Maximum percentage change in tumor density compared to baseline at various times. Top is *increase* in tumor density compared to baseline, and bottom is *decrease*. Time is measured in units of 2 weeks. The first two plots from Figure 4.8 are taken at times 1 and 40.

The second plot in Figure 4.9 can be viewed similarly and interpretation can be aided by consulting the plots in Figure 4.7. Indeed, ϕ has a significant impact on tumor size from the beginning, as expected. By the end of the test period, we can see that the solution perturbed in ϕ is a very small fraction of the baseline solution. Such a difference at the end of the time period suggests settlement at a significantly different steady state. We can see that this is in fact the case by consulting the left hand side of Figure 4.7, wherein the value of ϕ for our baseline solution ($\phi = 2.5 \times 10^{-5}$) is to the right of the region of bistability, and the value of ϕ responsible for the greatest decrease in tumor density relative to baseline is within the region of bistability. Because all solutions begin with $u = 0$ initially, the solution will approach the lower of the two stable states. A similar phenomenon is also likely for the parameters that see a difference from baseline of $\geq 60\%$ (tumor growth, death, and the CT immune dynamics). The parameters that do not see such large changes from baseline likely do not induce similar bifurcations. As a final note, the source term ϕ is always the most sensitive in the case of decrease.

Even with parameters estimated from the literature when possible, Figures 4.8 and 4.9 reveal the importance of accurate parameter estimation in order to inform novel biological investigations. In particular, if the baseline parameters are close to a bifurcation value, caution must be exercised. We note, however, that the parameters estimated in Kuznetsov [91] also resulted in their system being relatively close to a separatrix.

4.3.2 Simulations: Primary Resection

We now use our parameterized model to investigate the possible implications of the immune-mediated theory of metastasis. In this section we consider the effects of primary resection on the metastatic tumor. Figure 4.10 demonstrates the effect of bistability discussed in Section 4.2.5 on the results of primary resection. Figure 4.10 (A) shows the tumor density as a function of time. The black curve is the control, while the red and green curves are the dynamics at the secondary site upon primary resection — simulated by setting the source terms $\phi = \psi = 0$ — at various times. If primary resection is performed

sufficiently early in the progression of the metastatic tumor, we can see disease extinction (green curves). If, however, primary resection is done at a later time, we see persistent metastatic disease (red curves).

To confirm the suitability of using the slow-manifold approximation 4.33 to analyze the model dynamics, we compare our solution trajectories in (u, x, y) space to the slow manifold(s) \mathcal{M}_2 . Figure 4.10 (B) shows the model dynamics and the slow manifolds projected onto the $x - y$ plane. The manifolds are monotonically increasing in u beginning at $(u, x, y) = (0, 1, 0)$ (blue, dashed line) and $(u, x, y) = (0, 1, \frac{q\psi}{r})$ (black). All solutions begin at $(u_0, x_0, y_0) = (0, \alpha/\omega, 0) = (0, 1, 0)$ and quickly travel to the slow manifold (black, dashed line). The control dynamics travel along \mathcal{M}_2 until the full-disease steady state (marked as a black circle) is reached. The remaining trajectories travel along \mathcal{M}_2 until primary resection occurs and the source terms ϕ and ψ are set to zero. Not only does removing the source terms change the dynamics, it also shifts \mathcal{M}_2 down along the y -axis to the blue dashed line.

Upon resection, solutions quickly jump between the $\phi \neq 0, \psi \neq 0$ manifold (black) to the $\phi = \psi = 0$ manifold (blue). Solutions landing on the blue \mathcal{M}_2 *below* the open circle are destined for extinction (blue solid circle at $(0, 1, 0)$), while those that land *above* the open circle result in persistent metastatic disease (left blue solid circle). The close agreement of the model dynamics and the slow manifold(s) \mathcal{M}_2 allow us to use the slow-manifold approximation 4.33 to determine the number, location, and stability of steady states in the model.

Plot (C) shows the dynamics of $\frac{du}{dt}$ as determined by (4.33) for the case when ϕ and ψ are non-zero (black), and for the resection case, $\phi = \psi = 0$ (blue). The control dynamics show a single, stable steady state that corresponds well with the observed behavior in plots (A) and (B). The post-resection case shows the existence of 3 steady states: a stable, persistent metastatic disease state, a stable disease-free state (solid blue circles), and an unstable saddle node between them. Note that the location of the saddle node coincides with the ‘threshold’ tumor density that determines whether or not primary resection will be successful at disease eradication. Therefore, the success of primary resection is determined entirely by the location of the saddle node in the post-

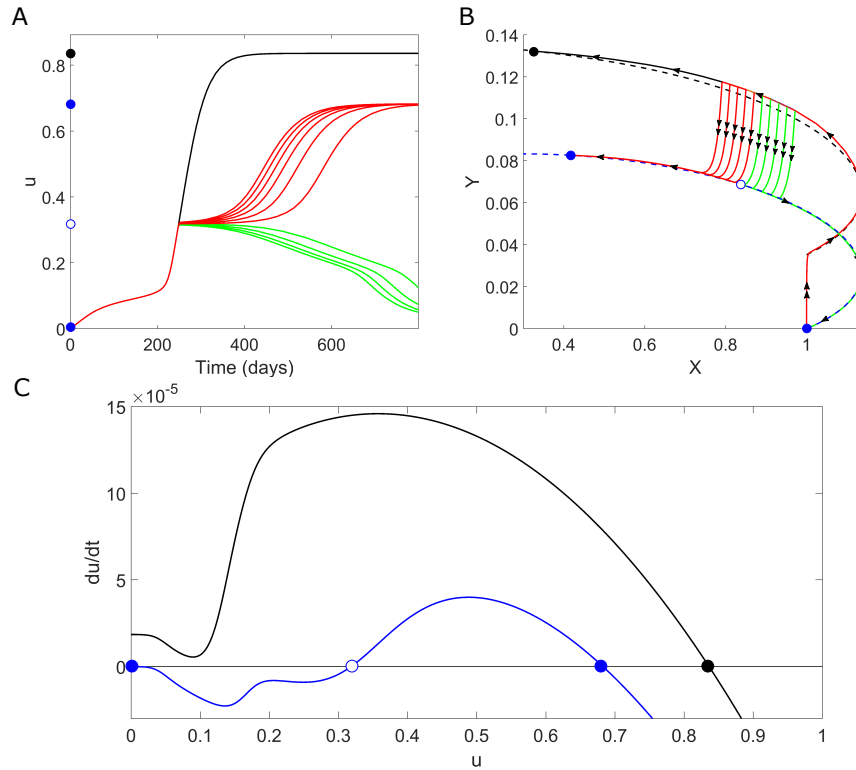


Figure 4.10: Results of simulated primary resection. Primary resection was simulated by setting the source terms, $\phi = 0$ and $\psi = 0$ at different times. (A) The effect of primary resection on secondary tumor growth. Early interventions result in disease extinction (green) and late interventions result in disease persistence (red). (B) Model dynamics in 3-space, with the slow manifold for $\phi, \psi \neq 0$ is the dashed black curve, and the dashed blue curve denotes the slow manifold when $\phi = 0 = \psi$. (C) Phase line diagrams for the cases when the source is on (black) and off (blue). Steady states are indicated by circles, solid representing stable and hollow representing unstable. The steady states are also marked in plots (A) and (B) for illustration. Parameters as in Table 4.2, with the exception of $max_1 = 2.5$, $up_1 = 0.1$, and $\phi = 1.8519 \times 10^{-5}$.

resection dynamics.

In contrast to the simple ‘turning off’ of the source terms ϕ and ψ used to model primary resection in Figure 4.10, Figure 4.11 shows the effects of simulating primary resection by including a transient, systematic inflammation response after resection [113]. At day 365, approximately when the tumor reaches its steady state value (A), we simulate primary resection by setting the source of tumor cells ϕ , to zero. We assume that for 7 days there will be an inflammatory response to the surgery at the primary site. The inflammatory response is modeled by increasing the CT immune cell influx rate, α , by anywhere between 2 and 500 times. As a control, we include one trajectory in showing the effects of not changing the CT immune response, as well as one in which we halve the influx rate for the 7 day period of transient inflammation. We also keep $\psi \neq 0$ over this week in order to model the pro-growth aspect of the immune response. A week after the primary tumor has been removed, the CT influx rate is returned to its original value, and increase the education rate of CT immune cells by the tumor by a factor of 2.42. After these final adjustments we allow the system to evolve without further interaction.

The results of these simulations are presented in Figure 4.11 (top). The control dynamics are in black, and we see a small, persistent tumor that reaches its maximum density after approximately one year. For low inflammatory responses to the primary resection, we see slow secondary tumor decay (green curves), whereas larger inflammatory responses can result in rapid metastatic growth after a varying period of little to no growth. As in the previous simulations, these dynamics can be explained by the slow manifold approximation (4.33), which is presented in the bottom half of Figure 4.11. The black curve denotes the control dynamics and the blue curve denotes the post-resection dynamics.

The control dynamics have three steady states: stable large and small tumors separated by an unstable saddle. Of note is the close proximity of the saddle to the smaller stable steady state — a small increase in the tumor density here can result in the development of a much larger tumor. Because $\phi = 0$ post-resection, the extinction state an unstable saddle and the blue curve has 4 roots, with 3 of them distributed similarly to the control case. In

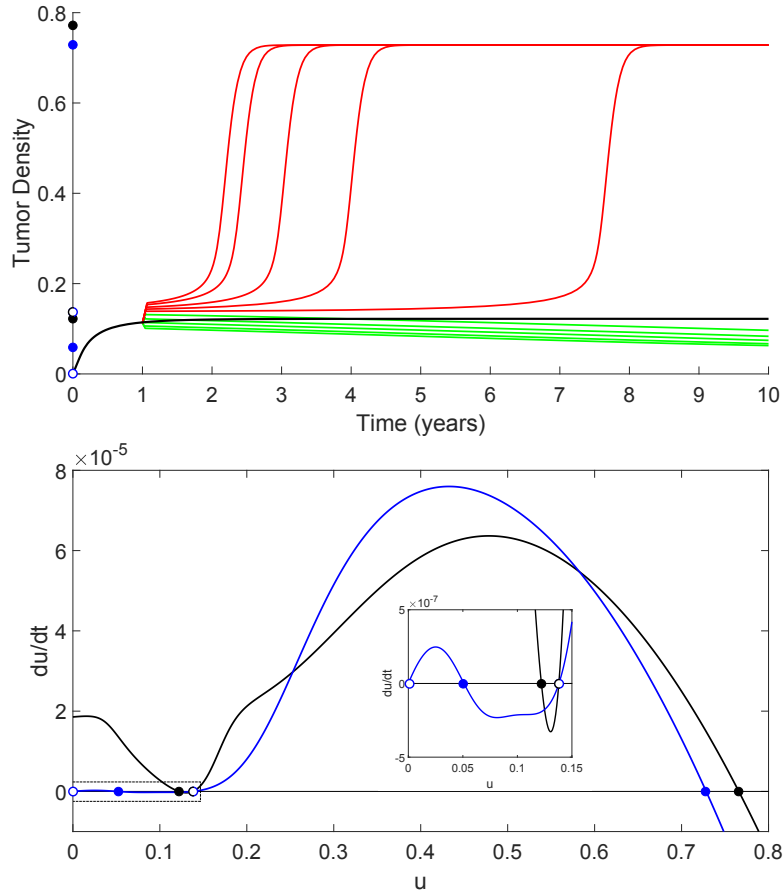


Figure 4.11: Results of simulated primary resection. Primary resection was simulated by setting the source term $\phi = 0$. A transient immune response of 7 days was simulated by changing the value of α for those seven days. Green curves had α change by factors of 0.5, 1, 2, 5, and 10 (from bottom to top). Red curves had α change by factors of 25, 50, 100, 250, and 500 (from right to left). After the inflammatory response, we also set $\psi = 0$ and increased the education rate, χ , by a factor of 2.42. Inset is an expanded depiction of the boxed region. Parameters as in Table 4.2, with the exception of $max_1 = 2.5$, $r = 0.0002$, and $\phi = 1.8519 \times 10^{-5}$.

particular, the education increase factor of 2.42 was chosen to have the post-resection saddle approximately equal to that of the control dynamics (see inset detail).

The proximity of the small steady state in the control dynamics to the saddle in the post-resection dynamics explains the different outcomes possible in the top plot. Indeed, the transient, systematic inflammation response to primary resection can result in a brief period of tumor growth at the secondary site. If this growth is sufficient to pass the saddle node in the post-resection dynamics, then our model predicts the development of a large metastatic tumor (rightmost solid blue circle). Otherwise, the secondary tumor will decay to the smaller, persistent tumor (leftmost solid blue circle).

4.3.3 Simulations: Immune Therapy

The final simulations we present in Figure 4.12 are of primary resection coupled with an immune response in the case that the disease-free steady state is stable in the post-resection dynamics. Primary resection occurs at time $t = 243.85$ days (indicated by arrow) and is simulated by setting both source terms, ϕ and ψ , to zero. We also include a transient inflammatory response where the CT immune cell influx rate is increased over the course of 7 days (marked as a pink vertical band), and then returned to its original value on the seventh day after primary removal. The effect of primary resection and an inflammatory response of strength 50 (α increased by a factor of 50) is shown in the red curve, where we see metastatic growth after a sustained period of little to no growth (blue region). Decreasing the strength of the inflammatory response to 49 gives us the magenta curve, and tumor extinction after a similar period of little to no growth. With no inflammatory response (of strength 1), we see rapid extinction of the metastatic tumor (green). Similar extinction results can be observed with an inflammatory response of strength 50 if the tumor education rate is decreased to 95% its original value (blue). As before, these bistable dynamics are governed by the emergence of a saddle node between two stable steady states in the post-resection dynamics (see Figure 4.10)

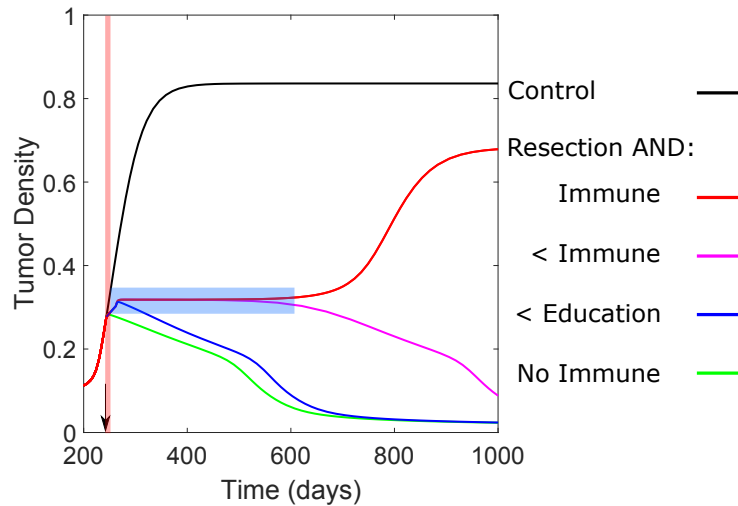


Figure 4.12: Results of simulated primary resection with an induced immune response. Primary resection was simulated by setting the source term $\phi = 0$ and $\psi = 0$ at time $t = 243.85$ days. A transient immune response of 7 days was simulated by changing the value of α for those seven days (increased by factor of 50 in red and blue, 49 in magenta, and no increase in green). The effect of decreasing the education rate was tested (blue - decreased to 95% its original value starting at time of resection until end of simulation). Time of primary resection indicated by arrow. Transient period of inflammation indicated by the region in red. Region in blue highlights delayed tumor growth or death. Parameters as in Table 4.2, with the exception of $max_1 = 2.5$, $up_1 = 0.1$, and $\phi = 1.8519 \times 10^{-5}$.

4.4 Discussion

In Chapter 4 we have introduced, analyzed, and simulated a model of tumor-immune dynamics at a secondary site that includes both anti- and pro-tumor effects of the immune system. By assuming tumor dynamics and immune dynamics occur on different time scales and using techniques from geometric singular perturbation theory and quasi-steady state analysis, we were able to reduce the original system of 3 ODEs, making the model more amenable to analysis.

In the case that tumor dynamics are *fast* relative to the immune dynamics, our 3 ODE system reduces to a 2 ODE system and the dynamics take place along the 2 dimensional slow manifold. Figure 4.2 shows the slow manifold and solution trajectories for increasing (blue to red) values of α , the rate of CT immune cell influx. A simple model of immunotherapy is to increase the value of α , thereby supplying the tumor environment with more CT immune cells to destroy the tumor cells. In this case, our model predicts 4 distinct outcomes for tumor density. For small values of α , there will be a low immune presence, resulting in a medium sized tumor (region I). As we increase the value of α , the steady state tumor density (marked as black circles) is increasing and moving towards the high plateau of region II, corresponding to a tumor in which the pro-tumor effects of the immune system dominate. Increasing α further, however, sees the CT immune cell population pass a critical threshold where the anti-tumor effects of the immune system dominate, resulting in a markedly lower final tumor density in region III. Increasing α further results in a paradoxically larger tumor in region IV. Tumor education of CT immune cells into pro-tumor TE immune cells is responsible for this climb between regions III and IV.

Therefore, in the case of fast tumor and slow immune dynamics, our model provides a possible explanation for the poor performance of some immunotherapeutic strategies. Indeed, if the tumor is able to educate infiltrating CT immune cells, then increasing the source of these cells has the effect of increasing the number of TE immune cells. This increase in TE immune cells allows the tumor to grow larger, rather than die away. These results suggest that more

careful study of the contradictory effects of the immune system may be needed in order to increase the efficacy of immunotherapeutic strategies. We do note, however, that these results have assumed fast tumor and slow immune dynamics, which is most likely not the case, with tumor growth occurring on the scale of months or years, and immune responses on the scale of minutes (a wound healing response for example).

Consequently, it is of more interest biologically to study the case when tumor dynamics are assumed to be *slow* relative to the immune dynamics, which was the focus beginning at Section 4.2.4. Under the assumption of slow tumor and fast immune dynamics, we showed that the model dynamics are well approximated by the slow manifold approximation. Using the slow manifold approximation allowed us to determine the steady states and their stability by considering simple phase line diagrams. Upon parameterization of the model, our analytical results gave a full explanation of observed dynamics, providing insights that would not be possible otherwise. We now discuss the biological interpretations of these analytic results.

Where possible, estimates were obtained from the literature, with the tumor growth rate being fit to experimental data from Park [112] and a large number of the CT immune parameters taken from Kuznetsov [91] which were themselves fit to experimental data from Siu et al. [128]. Values for the source terms, ϕ and ψ , were informed by the data presented by Weiss [137]. The education rate of CT immune cells by the tumor, u , was based on the results of den Breem and Eftimie [34], which were parameterized to data from Chen et al [23]. Literature estimates for the parameters associated with TE immune cells could not be found, and were assumed to be similar to the analogous CT immune cell parameters. Only the threshold parameters in the functional coefficients $\sigma(x)$ and $\gamma(y)$ could not be justified in some way by the literature, which was not unexpected given the relative novelty of the approach taken herein. Therefore, we can be relatively confident that the simulations presented above are somewhat representative of reality, but caution is always prudent when estimating parameters from the literature (see the discussion in [138] for example).

In order to address the potential uncertainty in our results arising from

our parameter estimates, we have presented the results of a parameter sensitivity analysis in Figures 4.8 and 4.9. While increases in tumor steady state values were modest for most parameters, with the notable exception of the minimum tumor cell death rate, min_2 , changes in many parameter values could result in significantly smaller steady state tumor densities. In the case of the tumor source term, ϕ , using numerical bifurcation analysis we found that the creation of new steady states explained this phenomenon. Similarly, Kuznetsov [91] found that their parameterized model was highly sensitive to initial conditions because of the proximity of experimental initial conditions to a separatrix. These bifurcations may provide insight into treatment strategies, and is discussed in further detail below. Assuming that the parameter estimates in Table 4.2 are accurate, the result that several parameters are quite sensitive and result in bifurcation suggest that treatment options may not need to be very strong, but must be appropriately targeted to effect one of the most sensitive parameters.

We also found that the relative sensitivities of the model parameters varied greatly in time. As intuitively expected, parameters that had early effects on the tumor density were the source rate, ϕ , and the TE immune parameters, up_1 (saturation level) and τ (decay rate). Indeed, when our metastatic site begins devoid of any cancer cells, it is clear that a source of cells to colonize the site will have a great effect on the early dynamics. Moreover, the sensitivity of the parameters associated with the TE immune population demonstrates the importance of the PMN [84] on metastatic establishment and provides support for the theory of immune-mediated metastasis [124]. The final parameter we discuss here is the minimum tumor cell death rate, min_2 , which plays a significant role in both increasing and decreasing the final tumor density. Again, this result is fairly intuitive: increasing the death rate results in a smaller tumor, and decreasing the death rate allows for the development of a larger tumor. Unfortunately, this is one of the parameters for which no reasonable estimate could be found in the literature. Our results suggest that studies to determine the value of these death rates should be done in order to increase the reliability of our model predictions and because they may be important to inform treatment planning.

Of particular relevancy to cancer treatment is the model dependency on the source parameter ϕ . Although we have previously interpreted the decrease in ϕ as a removal of the primary tumor, it may also be interpreted as interference with successful establishment at a secondary site. As discussed in Chapter 1, the use of anti-inflammatory medications that can inhibit tumor-platelet clump formation has been shown to effectively decrease the incidence of metastasis. Such an intervention could be interpreted in our model as a decrease to the source/establishment term ϕ . In this case, the bifurcation plot in Figure 4.7 (left) becomes of particular interest. Indeed, if we begin with a high value of ϕ , the model predicts a single stable steady state corresponding to full metastatic disease. As we decrease ϕ — through the use of NSAIDs for example — we may see decreased establishment of CTCs at the secondary site, resulting in a decreased value of ϕ . As ϕ decreases, we move into the region of bistability. If this intervention occurs sufficiently early in the progression of the disease, the secondary tumor density may lie *below* the saddle threshold value, and we would then expect a small metastatic tumor. Otherwise, a large metastatic tumor is expected, but its size decreases as we decrease the value of ϕ . Finally, if we decrease ϕ enough, the region of bistability is exited and a small metastatic tumor will persist. These results reflect the experimental observations of decreased incidence of metastasis with the use of NSAIDs [83, 98] and lend further credibility to the results presented herein.

Recent theoretical studies by Hanin and collaborators [62] have suggested that metastatic dormancy is a ‘natural law’ in the progression of cancer. Metastatic, and more generally tumor dormancy, has been of interest in theoretical investigations of cancer progression for years [32, 33]. In many instances, dormancy is characterized by the smallest population among a number of steady states (see [91] for example). However, a recent paper by Wilkie and Hahnfeldt [138] characterizes dormancy as a transient state of little to no growth. Our model is capable of describing dormancy in both definitions. The control dynamics in Figure 4.11 have two stable steady states; one large, ‘full disease’ state, and a smaller, ‘dormant’ state, thereby providing the steady state interpretation of dormancy. The transient explanation can be seen in the treatment curves of Figure 4.11 and in the red and magenta curves of Figure

4.12. Solutions in these plots remain nearly constant for extended periods of time (between 1 and 6.5 years) before eventually either growing or decaying. We have shown that these transient dynamics are governed by an unstable saddle node which acts as a threshold for tumor fate.

In [56], Gorelik summarizes the effects of primary resection on metastatic tumor growth dynamics based on the size of the primary tumor: removal of a *small* primary tumor results in decreased metastatic disease; if the primary tumor is *medium*-sized, primary resection has little effect on metastatic progression; and allowing the primary tumor to grow to a *large* size before removal results in explosive post-resection metastatic growth. Our model successfully captures these observed dynamics. In Figure 4.10 there is a threshold (secondary) tumor density, below which primary removal results in metastatic decay and eventual disease clearance (green curves), and above which primary removal delays and slightly stunts metastatic growth, but the disease persists (red curves), thereby accounting for the Gorelik observations of removing *small* and *medium* sized (primary) tumors. In order to capture the explosive metastatic growth observed after removing a *large* primary tumor, we re-introduce the concept of metastatic ‘blow-up’.

Metastatic ‘blow-up’ — rapid metastatic growth upon removal of the primary tumor [62] — can also be reproduced with our model (Figure 4.11). Treating primary resection not only as a removal of the source of CTCs, but also as a wound that illicit a wound-healing response (source of both CT and TE immune cells) results in a small jump in tumor density after the resection event due to the increased immune presence, with the CT cells being educated by the tumor to play a pro-tumor role. Importantly, in order to observe blow-up in our model, the TE immune population must be maintained. In our model this can be done by either keeping a positive source term, or by increasing the education rate. The simulations presented have assumed that the education rate increases, and the source of TE immune cells vanishes at the end of the inflammatory period. However it is accomplished, if the secondary tumor is capable of maintaining a sufficiently large population of TE immune cells, we see rapid metastatic growth after a period of dormancy.

Eikenberry and colleagues considered local metastatic spread in a spatially

explicit PDE model [45] and included immune cells that could kill tumor cells, as well as provide pro-angiogenic factors to the tumor microenvironment. The angiogenic factors allowed for the growth of blood vessels to supply the local tumor environment with oxygen, thereby supporting tumor growth. Upon manual seeding of local metastases, the authors simulated primary resection by removing all cell types within the resection area, including immune cells. With certain parameter values, their model showed metastatic blow-up. The authors argued that the removal of the immune population in the resection allowed the previously controlled micrometastases to grow rapidly after primary removal. In contrast, our blow-up phenomenon is induced by an inflammatory response not included in Eikenberry’s simulations, and is well characterized mathematically, whereas the explanation provided in [45] is based on the authors’ intuition because the complexity of their model precludes rigorous analysis.

In our model, blowup is (as we have seen before) due to the emergence of a saddle node acting as a threshold tumor density governing disease outcome. So, the phenomenon is understood mathematically, but the biology is not as clear. Very little is known about the dynamics of tumor education of CT immune cells, but our results suggest a couple of new avenues for experimental studies. First, is there an increase in pro-tumor inflammatory cells at metastatic sites upon primary resection? Second, if such an increase is observed, how is it mediated; through recruitment or education? Third, if TE expansion is through education, what precisely is meant by ‘education’? Many investigators have suggested an active role for the primary tumor in the suppression of metastatic growth [62]. Based on the results of our model, we suggest that one way in which this active suppression could be mediated is by maintaining a *limited* population of pro-tumor TE immune cells at the secondary site. Such control of distant sites may be best accomplished by larger primary tumors, in which case our results coincide with the effects of primary resection summarized by Gorelik [56] and introduced above. Assuming that the primary tumor *can* regulate the TE immune population size at the secondary site, removal of the primary would result in an increased population of TE immune cells at the secondary site, possibly resulting in metastatic

blow-up as seen in Figure 4.11. Further theoretical and experimental investigations are needed in order to fully elucidate the validity of this addition to the immune-mediated theory of metastasis [124], especially considering these results are in stark contrast to the concerns presented in [119], suggesting that delayed metastatic growth argues *against* the concept of a PMN and related concepts including primary tumor intervention at secondary sites.

Experimental results by Park and colleagues [112] provide another validation of our model predictions. In [112] the authors demonstrated that perioperative implantation of a gel scaffold containing immunotherapeutic agents that prevent a pro-tumor inflammatory response and bolster an anti-tumor immune response to the wound incurred during primary resection surgery can effectively eliminate distant metastases. Figure 4.12 presents the results of simulating primary resection that induces an inflammatory immune response. In the presence of an inflammatory response to the primary resection surgery, the growth of the secondary tumor arrests for an extended period of time, until eventually growing into a large metastatic tumor (red curve), although smaller than the control tumor (black curve). If we are able to prevent the inflammatory response, we can see curative responses like in [112] (magenta and green curves). On the other hand, the same inflammatory response can be felt, but prevention of the tumor education of CT immune cells can result in relatively rapid metastatic extinction (blue curve). Therefore, our model predictions are supported by the experimental evidence in [112] in so far that prevention of a pro-tumor inflammatory response and stimulation of an anti-tumor response upon primary resection can result in metastatic extinction.

The effects felt by the secondary tumor in response to treatment of the primary tumor are known as *abscopal* effects. The Enderling group has recently developed a model for immune trafficking between distant metastatic sites and have presented simulations with biologically realistic connections between organs in order to investigate the potential role of immune trafficking on *abscopal* effects [115, 135, 134]. While their presented results cannot capture the *development* of metastatic disease, they do provide insight on the dynamics of treatment under the assumption of pre-existing metastatic tumors. Their model is able to reproduce both positive (lower tumor burden at

secondary site) and negative (blow-up) abscopal effects upon resection of one of the tumors. Similarly to Eikenberry [45], the authors suggest that this is a result of the re-distribution of CT immune cells and depends on the immune cell trafficking between the disparate sites. Their explanation of the observed effects differ slightly from ours as they do not account for the pro-tumor effects of the immune system in their model.

However, the Enderling group’s framework does allow for biologically realistic trafficking between distant anatomical sites — something that our simple two-site model cannot do. Future refinement of our model may include such considerations and may follow the Enderling group’s lead, incorporating ideas from disease transmission models [85]. Because of the importance of the source/establishment term ϕ , it would be valuable to consider the case of a time-dependent source, $\phi(t)$, instead of assuming a constant source. Choices for $\phi(t)$ could include increasing functions in t — assuming that the primary tumor is growing and shedding more cells into the circulation thus allowing for increased settlement — or even a source that turns ‘on’ and ‘off’ according to a stochastic process to incorporate the stochastic nature of metastasis into the model [92]. In any case, further study into the dynamics of metastatic establishment are warranted as the process is poorly understood and critical to disease outcome. A similar concern arises with the modeling of tumor education of CT immune cells. We have assumed simple mass-action kinetics here [34], but the precise dynamics are likely much more complicated and warrant further study in their own right. As metastasis is an inherently spatial process, the explicit inclusion of space would be a valuable addition to the model, especially to investigate potential roles of the PMN on establishment patterns (for example).

As a final remark, we note that our model is just that — a *model*. Without better data informing parameter estimates and choices of functional coefficients, caution must be taken when interpreting our results, especially when discussing potential implications for therapeutic strategies [31]. Having made the appropriate disclaimer, we believe that the work presented here provides strong theoretical evidence for further research into the competing roles of the immune system in cancer progression. A number of direct biological ques-

tions have been put forth, and additions to the immune-mediated theory of metastasis have been made.

Chapter 5

Conclusion

What *should* a successful model of metastatic cancer look like? What properties should it have? What observed phenomena should it be able to reproduce? At the end of Chapter 1 we suggested a list of 10 desirable properties that we suggested a *successful* model of metastasis would include. In this final chapter we re-visit that list and discuss the *success* of the models investigated in Chapters 2 – 4, and possible modifications to address shortcomings. We maintain the same numbering as the original list in Chapter 1.

1. Can the model reproduce the establishment and development of a secondary tumor at a site distant from the primary tumor?
 - Yes, all three of the models investigated herein are capable of producing secondary tumors at sites distant from the primary. The stochastic model from Chapter 2 interprets the settlement of a mobile particle as the establishment of a tumor at a secondary site, thereby allowing us to investigate the spatial dynamics of metastatic spread. Growth dynamics at the secondary site were not explicitly modeled, and we demonstrated that, as a result, our model could not accurately reproduce the results of the experimental metastasis assay from [15], suggesting that modeling growth at the secondary site would be an important addition to the model. The deterministic models from Chapters 3 and 4 include explicit models of tumor-immune dynamics at a secondary site, allowing for the establish-

ment of CTCs released from the primary tumor and the growth of these micrometastases into macrometastases and eventually full metastatic tumors.

- Although a positive answer to question (1) may seem like the very *least* required of a model of metastasis, many previously investigated models that report results relevant to metastasis are incapable of answering ‘yes’. Whether metastasis is assumed to have occurred upon sufficient local invasion [5, 127], or metastases are manually seeded, sometimes even of a magnitude similar to that of the primary tumor [45, 134], many of the previous models investigating metastasis cannot (or do not) describe metastatic establishment or early metastatic growth. Based on our results, these processes should be important in the dynamics of metastatic cancer, and should be included in models desiring to accurately represent the metastatic process.

2. Can the model reproduce immune-mediated help in metastatic establishment? [84, 124]

- Without including immune cells of any type, the stochastic model of Chapter 2 cannot reproduce any immune-related phenomena. However, based on the results of Chapters 3 and 4, extensions of the model to include immune effects may be warranted.
- Yes, both deterministic models developed in Chapters 3 and 4 include immune-mediated help in metastatic establishment. Figures 3.9 and 3.10 demonstrate that tumor-education of immune cells can result in a significantly larger tumor developing much faster than when no such phenotypic transition is possible. Similarly, the injury simulations in Figure 3.13 show that a wound healing response can be corrupted by a sufficiently large secondary tumor, causing immune-mediated metastatic blow-up.

3. Can the model reproduce metastatic dormancy? [62, 138]

- Because the stochastic model of Chapter 2 does not include any growth dynamics, it is incapable of reproducing metastatic dormancy. We have already noted that this shortcoming is likely responsible for the poor fitting of the model to the experimental metastasis data from Cameron et al. [15] (Figure 2.6); the inclusion of sub-models for tumor growth dynamics of settled cells may address this deficiency in the model.
 - Yes, metastatic dormancy can be observed in both of the deterministic models investigated in Chapters 3 and 4. Mathematically, dormancy was characterized as either a small steady state value, or dynamics slowed by the proximity to a saddle node (both shown in Figure 4.11). The transient nature of dormancy observed in our model is in agreement with other recent theoretical investigations that have found similar results in the context of general tumor dormancy [138].
4. Can the model reproduce metastatic blow-up upon primary resection? [56, 62]
- Although not specifically tested using the stochastic model from Chapter 2, the independence of the individual particles assumed in the model does not allow for an appreciable effect to be felt by removing the primary tumor. The assumption of independence between particles may be relaxed, but such a modification would significantly alter the model and is left as future research.
 - Yes. While both deterministic models from Chapters 3 and 4 *could* produce results that were interpreted as metastatic blow-up (Figures 3.15 and 4.11), the simplicity of the 3 ODE model from Chapter 4 allowed us to explore the phenomenon more carefully, resulting in the discovery of a more realistic scenario leading to blow-up.
5. Can the model reproduce abscopal effects? [37, 112, 134]
- As in the previous case, the independence of the stationary particles

in the stochastic model of Chapter 2 precludes any abscopal effects in the model.

- Yes. Abscopal effects were considered in several contexts with the deterministic models from Chapters 3 and 4. Primary resection was considered in both chapters and could result in either positive (tumor delay or extinction in Figures 3.8 and 4.10) or negative (metastatic blow-up in Figures 3.15 and 4.11) abscopal effects, depending on the method of modeling the intervention and the resulting immune response. Similar theoretical results have been reported by Walker et al. in [134], where the authors also considered the effects of localized radiotherapy applied to the primary tumor. Although not considered in this work, the effects of radiotherapy could easily be included in the modeling framework we have developed, and is left as future work.
- The results presented in Figure 4.12 are in qualitative agreement with the experimental results of Park et al. [112], thereby providing the concept of immune phenotype plasticity (tumor education of CT immune cells) as a possible explanation of their observations.

6. Can the model reproduce metastasis to sites of injury? [124]

- Yes. The full 8 ODE, 2 site model investigated in Chapter 3 was successful in replicating observations of metastatic spread to sites of injury (Figure 3.13). If the injury occurs when the tumor population at the secondary site is sufficiently small, the wound healing immune response remains largely anti-tumor, and dramatically slows metastatic development. If, on the other hand, the injury occurs after a sufficient tumor population has established at the site, the wound healing immune response is educated/corrupted by the tumor, resulting in a large pool of pro-tumor immune cells in the metastatic environment, which triggers metastatic blow-up.

7. Can the model provide prescriptions for more effective therapies?

- Yes. The metastatic reproduction number, R_0 , derived from the stochastic model in Chapter 2, provides a simple, easily understandable condition for metastatic extinction: reduce the shedding and establishment rates of CTCs, or increase cancer cell death rates. While decreases to the rates of shedding and establishment may require more advanced approaches (such as disrupting the PMN for instance), increases to the death rates may be accomplished much more simply by way of cytotoxic therapies such as radiotherapy or chemotherapy. Of particular interest, the use of NSAIDs to disrupt the formation of platelet-cancer clusters, which has been shown to decrease the instances of metastasis [26, 119, 124], may be interpreted as increasing the death rate of mobile particles thereby decreasing the value of R_0 .
- A similar appeal to NSAIDs can be made based on the results from both Chapters 3 and 4. Although the ‘switching off’ of the source term was often suggested to model primary resection therapies, it could be viewed as a model for any therapy that *reduces* the number of CTCs arriving and establishing at a secondary site. In particular, reduction of the source of CTCs could be accomplished by way of NSAID therapy.
- The models in Chapters 3 and 4 also provided a potential explanation for the disappointing effects of some immunotherapies: tumor-education of CT immune cells. Figures 3.9 and 3.10 show that education is responsible for the non-monotonic response to immunotherapy predicted by the model, and that preventing education can markedly increase the effectiveness of immunotherapy. Similarly, metastatic extinction as a consequence of decreasing the education rate (Figure 4.12) — a theoretical result supported by the experimental results of Park et al. [112] — illustrates the potential power of preventing tumor education on treatment outcomes.
- Explicit conditions necessary for the stability of disease-free states

in the two deterministic models were also obtained (Theorem 4 and Proposition 2). These conditions suggest that increasing tumor death rate or decreasing tumor growth rate must be done in order to see disease extinction.

8. Can the model provide testable biological predictions?

- Yes. All three of the considered models have produced biological predictions. Highlights include:
 - The metastatic reproduction number, R_0 , and its predictive power within our model suggest that estimation of the four component parameters — rates of shedding, establishment, mobile and stationary death — should be estimated using data from human cancer to determine the relevancy of R_0 in predicting the metastatic potency of different cancers.
 - The biphasic response to injury at the secondary site ca (Figure 3.12) could be explored experimentally in order to confirm or deny the theoretical results presented herein.
 - In order to observe metastatic blowup in Figure 4.11 the secondary site must maintain a substantial population of pro-tumor TE immune cells. We assumed that an increase to the education rate of CT immune cells by the secondary tumor occurred upon primary tumor resection, suggesting that the primary tumor may inhibit the TE immune population growth at the secondary site. Experiments to confirm or deny such a mechanism would provide further insights into the phenomenon of metastatic blow-up.
 - The inclusion of tumor education (tumor-induced immune phenotypic plasticity) provided a potential explanation for the disappointing performance of some immunotherapies. Based on the results presented here, further research into the mechanisms of such education are warranted.

9. Can the model reproduce local recurrence?

- Without including the primary site explicitly, the 3 ODE model in Chapter 4 cannot reproduce local recurrence.
- Even though simulations of primary resection were not presented in Chapter 2, if primary resection took place after the establishment of metastatic tumors, the model would allow for the ‘re-seeding’ of the primary site by the mobile cells shed by the metastatic tumors. No specific, targeted re-seeding at the primary site would take place, however, due to the spatial homogeneity of the establishment rate.
- Primary resections that were less than 100% efficient did result in local recurrence in the full 8 ODE model from Chapter 4.1. Recurrence in this case was a function of the tumor cells that were left by the incomplete resection, and the secondary tumor had no effect on this re-growth.
- Local recurrence may be better incorporated into these models, either by considering multiple sites as in the proposed system (3.18), or by introducing a spatially-dependent rate of establishment. Both of these modifications are left as future research.

10. Can the model reproduce tumor specific patterns of spread?

- None of the models investigated in this thesis are capable of reproducing tumor-specific patterns of metastatic spread. However, extensions to each of them could be considered that may address this shortcoming, for example:
 - More biologically realistic models of cell movement and spatially-dependent settlement rates may be introduced to the stochastic model from Chapter 2.
 - An extension of the 2-site models from Chapters 3 and 4 to an N -site model (as in equations (3.18)) incorporating biologically realistic travel between anatomical sites using ideas from [85, 134].

Overall, the models investigated in this thesis have been remarkably successful as models of metastatic cancer. Although there are shortfalls, modifi-

cations have been proposed to address them. Our results provide new insights into the metastatic process and introduce new biological questions for future research.

Bibliography

- [1] B.A. Aguado, G.G. Bushnell, S.S. Rao, et al. Engineering the pre-metastatic niche. *Nature Biomedical Engineering*, 1(0077), 2017.
- [2] S.R. Amith, J.M. Wilkinson, S. Baksh, and L. Fliegel. The Na⁺/H⁺ exchanger (NHE1) as a novel co-adjuvant target in paclitaxel therapy of triple-negative breast cancer cells. *Oncotarget*, 6(2):1262–75, 2015.
- [3] S.R. Amith, J.M. Wilkinson, and L. Fliegel. Na⁺/H⁺ exchanger NHE1 regulation modulates metastatic potential and epithelial-mesenchymal transition of triple-negative breast cancer cells. *Oncotarget*, 2016.
- [4] A.R.A. Anderson. A hybrid mathematical model of solid tumour invasion: the importance of cell adhesion. *Mathematical Medicine and Biology*, 22:163–186, 2005. doi: 10.1093/imammb/dqi005.
- [5] A.R.A. Anderson, M.A.J. Chaplain, E.L. Newman, et al. Mathematical modelling of tumour invasion and metastasis. *Journal of Theoretical Medicine*, 2:129–154, 2000.
- [6] N.J. Armstrong, K.J. Painter, and J.A. Sherratt. A continuum approach to modelling cell-cell adhesion. *Journal of Theoretical Biology*, 243(1):98–113, 2006.
- [7] F. Balkwill and L.M. Coussens. Cancer: An inflammatory link. *Nature*, 431:405–406, 2004. doi:10.1038/431405a.
- [8] E. Baratchart, S. Benzekry, A. Bikfalvi, et al. Computational modelling of metastasis development in renal cell carcinoma. *PLoS Computational Biology*, 2015. doi:10.1371/journals.pcbi.1004626.
- [9] D. Barbolosi, A. Benabdallah, F. Hubert, and F. Vega. Mathematical and numerical analysis for a model of growing metastatic tumors. 2008. jhal-00262335v1j.

- [10] R. Bartoszynski, L. Edler, L. Hanin, et al. Modeling cancer detection: Tumor size as a source of information on unobservable stages of carcinogenesis. *Mathematical Biosciences*, 171:113–142, 2001.
- [11] S. Benzekry. Mathematical analysis of a two-dimensional population model of metastatic growth including angiogenesis. *Journal of Evolution Equations*, 11:187–213, 2011. doi:10.1007/s00028-010-0088-5.
- [12] E. Bianconi, A. Piovesan, F. Facchin, et al. An estimation of the number of cells in the human body. *Annals of Human Biology*, 40(6):463–471, 2013.
- [13] A. Bovier. *Gaussian Processes on Trees: From Spin Glasses to Branching Brownian Motion*. Cambridge University Press, 2016.
- [14] D.E. Bowler and T.G. Benton. Causes and consequences of animal dispersal strategies: Relating individual behaviour to spatial dynamics. *Biological Reviews*, 80:205–225, 2005.
- [15] M.D. Cameron et al. Temporal progression of metastasis in lung: Cell survival, dormancy, and location dependence of metastatic inefficiency. *Cancer Research*, 60(9):2541–2546, 2000.
- [16] F. Castiglione and B. Piccoli. Cancer immunotherapy, mathematical modeling and optimal control. *Journal of Theoretical Biology*, 247(4):723–732, 2007.
- [17] C.L. Chaffer, I. Brueckmann, C. Scheel, et al. Normal and neoplastic nonstem cells can spontaneously convert to a stem-like state. *Proceedings of The National Academy of Sciences*, 108(19):7950–7955, 2011.
- [18] C.L. Chaffer and R.A. Weinberg. A perspective on cancer cell metastasis. *Science*, 331(6024):1559–1564, 2011. doi: 10.1126/science.1203543.
- [19] A.F. Chambers, A.C. Groom, and I.C. MacDonald. Dissemination and growth of cancer cells in metastatic sites. *Nature Reviews Cancer*, 2(8):563–572, 2002.
- [20] M.A.J. Chaplain and G. Lolas. Mathematical modelling of cancer cell invasion of tissue: The role of the urokinase plasminogen activation system. *Mathematical Models and Methods in Applied Sciences*, 15:1685–1734, 2005.

- [21] M.A.J. Chaplain and G. Lolas. Mathematical modelling of cancer invasion of tissue: Dynamic heterogeneity. *Networks and Heterogeneous Media*, 1(3):399–439, 2006.
- [22] J. Chen, K. Sprouffske, Q. Huang, and C.C. Maley. Solving the puzzle of metastasis: The evolution of cell migration in neoplasms. *PLoS One*, 6(4):e17933, 2011. doi:10.1371/journal.pone.0017933.
- [23] P. Chen, Y. Huang, R. Bong, et al. Tumor-associated macrophages promote angiogenesis and melanoma growth via adrenomedullin in a paracrine and autocrine manner. *Clinical Cancer Research*, 17(23):7230–7239, 2011.
- [24] J. Condeelis and J.E. Segall. Intravital imaging of cell movement in tumours. *Nature Reviews Cancer*, 3:921–930, 2003.
- [25] C. Coughlin and J. Murray. Current and emerging concepts in tumour metastasis. *The Journal of Pathology*, 222(1), 2010. doi:10.1002/path.2727.
- [26] L.A. Coupland, B.H. Chong, and C.R. Parish. Platelets and p-selectin control tumor cell metastasis in an organ-specific manner and independently of NK cells. *Cancer Res*, 72(18):4662–71, 2012. doi:10.1158/0008-5472.CAN-11-4010.
- [27] A de Mingo Pulido and B. Ruffell. Immune regulation of the metastatic process: Implications for therapy. *Advances in Cancer Research*, 132:139–163, 2016.
- [28] L.G. de Pillis, W. Gu, K.R. Fister, et al. Chemotherapy for tumors: An analysis of the dynamics and a study of quadratic and linear optimal controls. *Mathematical Biosciences*, 209(1):292–315, 2007.
- [29] U. Del Monte. Does the cell number 10^9 still really fit one gram of tumor tissue? *Cell Cycle*, 8(3):505–506, 2009. doi:.
- [30] P.P. Delsanto, A. Romano, M. Scalerandi, et al. Analysis of a phase transition from tumor growth to latency. *Physical Review E*, 62(2):2547–2554, 2000.
- [31] S. Demaria and S.C. Formenti. Can abscopal effects of local radiotherapy be predicted by modeling t cell trafficking? *Journal for ImmunoTherapy of Cancer*, 4(29), 2016.

- [32] R. Demicheli. Tumour dormancy: Findings and hypotheses from clinical research on breast cancer. *Seminars in Cancer Biology*, 11:297–305, 2001.
- [33] R. Demicheli, M. Terenziani, and G. Bonadonna. Estimate of tumor growth time for breast cancer local recurrences: Rapid growth after wake-up? *Breast Cancer Research and Treatment*, 51(2):133–137, 1998.
- [34] N. den Breems and R. Eftimie. The re-polarisation of m2 and m1 macrophages and its role on cancer outcomes. *Journal of Theoretical Biology*, 390:23–39, 2016. doi:10.1016/j.jtbi.2015.10.063.
- [35] D. G. DeNardo, M. Johansson, and L.M. Coussens. Immune cells as mediators of solid tumor metastasis. *Cancer Metastasis Reviews*, 27(1):11–18, 2008.
- [36] A. Devys, T. Goudon, and P. Lafitte. A model describing the growth and size distribution of multiple metastatic tumors. *Discrete and Continuous Dynamical Systems Series B*, 12(4):731–767, 2009. doi:10.3934/dcdsb.2009.12.731.
- [37] M.Z. Dewan, A.E. Galloway, N. Kawashima, et al. Fractionated but not single-dose radiotherapy induces an immune-mediated abscopal effect when combined with anti-ctla-4 antibody. *Clinical Cancer Research*, 15(17):5379–5388, 2009. doi:10.1158/1078-0432.CCR-09-0265.
- [38] D. Diego, G.F. Calco, and V.M. Perez-Garcia. Modeling the connection between primary and metastatic tumors. *Journal of Mathematical Biology*, 67:657–692, 2013. doi:10.1007/s00285-012-0565-2.
- [39] D. Dingli, F. Michor, T. Antal, and J.M. Pacheco. The emergence of tumor metastases. *Cancer Biology and Therapy*, 6(3):383–390, 2007.
- [40] B. Dos Anjos Pultz, F. Andres Cordero da Luz, S. Socorro Faria, et al. The multifaceted role of extracellular vesicles in metastasis: Priming the soil for seeding. *International Journal of Cancer*, 140(11):2397–2407, 2017.
- [41] H. K. Dvorak. Tumors: Wounds that do not heal. *New England Journal of Medicine*, 315:1650–1659, 1986. doi:10.1056/NEJM198612253152606.
- [42] H. K. Dvorak. Tumors: Wounds that do not heal - redux. *Cancer Immunol. Res.*, 3(1):1–11, 2015. doi:10.1158/2326-6066.CIR-14-0209.

- [43] R. Eftimie, J.L. Bramson, and D.J.D. Earn. Interactions between the immune system and cancer: A brief review of non-spatial mathematical models. *Bulletin of Mathematical Biology*, 73(1):2–32, 2011.
- [44] R. Eftimie, J.J. Gillard, and D.A. Cantrell. Mathematical models for immunology: Current state of the art and future research directions. *Bulletin of Mathematical Biology*, 78(10):2091–2134, 2016.
- [45] S. Eikenberry, C. Thalhauser, and Y. Kuang. Tumor-immune interaction, surgical treatment, and cancer recurrence in a mathematical model of melanoma. *PLoS Computational Biology*, 5(4):e1000362, 2009. doi:10.1371/journal.pcbi.1000362.
- [46] H. Enderling. Cancer stem cells: small subpopulation or evolving fraction. *Integrative Biology*, 7(1):14–23, 2015.
- [47] R. Erban, J. Chapman, and P. Maini. A practical guide to stochastic simulations of reaction-diffusion processes. 2008. Technical Report, Mathematical Institute, University of Oxford, Oxford, United Kingdom.
- [48] S.E. Erdman and T. Poutahidis. Roles for inflammation and regulatory t cells in colon cancer. *Toxicol. Pathol.*, 38(1):78–87, 2010. doi:10.1177/0192623309354110.
- [49] I. J. Fidler. Metastasis: Quantitative analysis of distribution and fate of tumor emboli labeled with ^{125}I -5-iodo-2'-deoxyuridine. *Journal of the National Cancer Institute*, 45(773):773–782, 1970.
- [50] C. Frei, T. Hillen, and A. Rhodes. A stochastic model for cancer metastasis: Branching stochastic process with settlement. *Mathematical Medicine and Biology*, 2018. Submitted. BioRxiv: 10.1101/294157.
- [51] P. Friedl and R. Mayor. Tuning collective cell migration by cell-cell junction regulation. *Cold Spring Harbor Perspectives in Biology*, 9:a029199, 2017.
- [52] R.A. Gatenby and E.T. Gawlinski. A reaction-diffusion model of cancer invasion. *Cancer Research*, 56:5745–5753, 1996.
- [53] R.A. Gatenby and P. Maini. Modelling a new angle on understanding cancer. *Nature*, 420(462), 2002. doi:10.1038/420462b.
- [54] D.T. Gillespie. A general method for numerically simulating the stochastic time evolution of coupled chemical reactions. *Journal of Computational Physics*, 22:403–434, 1976.

- [55] D.T. Gillespie. Exact stochastic simulation of coupled chemical reactions. *The Journal of Physical Chemistry*, 81(25):2340–2361, 1977.
- [56] E. Gorelik. Concomitant tumor immunity and the resistance to a second tumor challenge. *Advances in Cancer Research*, 39:75–120, 1983.
- [57] G.P. Gupta and J. Massague. Cancer metastasis: Building a framework. *Cell*, 127(4):649–695, 2006.
- [58] H. Haeno, Y. Iwasa, and F. Michor. The evolution of two mutations during clonal expansion. *Genetics*, 177(4):2209–2221, 2007.
- [59] H. Haeno and F. Michor. The evolution of tumor metastases during clonal expansion. *Journal of Theoretical Biology*, 263(1):30–44, 2010.
- [60] D. Hanahan and R. A. Weinberg. Hallmarks of cancer: The next generation. *Cell*, 144(5):646–674, 2011.
- [61] L. Hanin and O. Korosteleva. Does extirpation of the primary breast tumor give boost to growing metastases? evidence revealed by mathematical modeling. *Mathematical Biosciences*, 223(2):133–141, 2010. doi:10.1016/j.mbs.2009.11.006.
- [62] L. Hanin and J. Rose. Suppression of metastasis by primary tumor and acceleration of metastasis following primary tumor resection: A natural law? *Bulletin of Mathematical Biology*, 80(3):519–539, 2018.
- [63] L. Hanin, J. Rose, and M. Zaider. A stochastic model for the sizes of detectable metastases. *Journal of Theoretical Biology*, 243:407–417, 2006.
- [64] L. Hanin, K. Seidel, and D. Stoevesandt. A universal model of metastatic cancer, its parametric forms and their identification: what can be learned from site-specific volumes of metastases. *Journal of Mathematical Biology*, 72:1633–1662, 2016. doi:10.1007/s00285-015-0928-6.
- [65] G. Hartung and C. Gomez. A stochastic framework for secondary metastatic emission. 2014. Available at hal.archives-ouvertes.fr/hal-01052961.
- [66] N. Hartung. Efficient resolution of metastatic tumour growth models by reformulation into integral equations. 2014. jhal-00935233j.

- [67] N. Hartung, S. Mollard, D. Barbolosi, A. Benabdallah, et al. Mathematical modeling of tumor growth and metastatic spreading: Validation in tumor-bearing mice. *Cancer Research*, 74(22):6397–6408, 2014. doi:10.1158/0008-5472.CAN-14-0721.
- [68] V. Haustein and U. Schumacher. A dynamic model for tumour growth and metastasis formation. *Journal of Clinical Bioinformatics*, 2(11), 2012. doi:10.1186/2043-9113-2-11.
- [69] G. Hek. Geometric singular perturbation theory in biological practice. *Journal of Mathematical Biology*, 60(3):347–386, 2010.
- [70] P. Henry-Labordere, N. Oudjane, X. Tan, et al. Branching diffusion representation of semilinear PDEs and Monte Carlo approximation. 2017. Available at arXiv:1603.01727.
- [71] P. Henry-Labordere, X. Tan, and N. Touzi. A numerical algorithm for a class of BSDE via branching process. *Stochastic Processes and their Applications*, 124(2):1112–1140, 2014.
- [72] H.W. Hethcote. The mathematics of infectious diseases. *SIAM Review*, 42(4):599–653, 2000.
- [73] T. Hillen, H. Enderling, and P. Hahnfeld. The tumor growth paradox and immune system-mediated selection for cancer stem cells. *Bulletin for Math Biology*, 75(1):161–184, 2013.
- [74] T. Hillen, K.J. Painter, and W. Winkler. Convergence of a cancer invasion model to a logistic chemotaxis model. *Mathematical Models and Methods in Applied Sciences*, 23(1):165–198, 2013. doi:10.1142/S0218202512500480.
- [75] S. Hiratsuka, A. Watanabe, H. Aburatani, et al. Tumor-mediated up-regulation of chemoattractants and recruitment of myeloid cells pre-determines lung metastases. *Nature Cell Biology*, 8(12):1369–1375, 2006.
- [76] N. Ikeda, M. Nagasawa, and S. Watanabe. Markov branching processes I. *Journal of Mathematics of Kyoto University*, 8:233–278, 1968.
- [77] K. Iwata, K. Kawasaki, and N. Shigesada. A dynamical model for the growth and size distribution of multiple metastatic tumors. *Journal of Theoretical Biology*, 203(2):177–186, 2000. doi:10.1006/jtbi.2000.1075.

- [78] L.M.E. Janssen, E.E. Ramsay, C.D. Logsdon, et al. The immune system in cancer metastasis: Friend or foe? *Journal for ImmunoTherapy of Cancer*, 5(79), 2017.
- [79] T. Jessy. Immunity over inability: The spontaneous regression of cancer. *Journal of Natural Science, Biology and Medicine*, 2(1):43–49, 2011.
- [80] E. John Wherry. T cell exhaustion. *Nature Immunology*, 12:492–499, 2011.
- [81] M.K. Jolly, M. Boareto, B. Huang, et al. Implications of the hybrid epithelial/mesenchymal phenotype in metastasis. *Frontiers in Oncology*, 5:155, 2015.
- [82] C.K.R.T. Jones. Geometric singular perturbation theory. In J. Russell, editor, *Dynamical Systems*, pages 44–118, Montecatini Terme, Italy, 1995. 2nd Session of the Centro Internazionale Matematico Estivo (CIME), Berlin: Springer.
- [83] J.A. Joyce and J.W. Pollard. Microenvironmental regulation of metastasis. *Nat. Rev. Cancer*, 9(4):239–252, 2009. doi:10.1038/nrc2618.
- [84] R.N. Kaplan, R.D. Riba, S. Zacharoulis, et al. VEGFR1-positive haematopoietic bone marrow progenitors initiate the pre-metastatic niche. *Nature*, 438:820–827, 2005. doi:10.1038/nature04186.
- [85] M.R. Jr. Kelly, J.H. Tien, M.C. Eisenberg, et al. The impact of spatial arrangement on epidemic disease dynamics and intervention strategies. *Journal of Biological Dynamics*, 10:222–249, 2016.
- [86] Y. Kim, H. Jeon, and H. Othmer. The role of the tumor microenvironment in glioblastoma: A mathematical model. *IEEE Transactions on Bio-Medical Engineering*, 64(3):519–527, 2017.
- [87] T. Kitamura, B.Z. Qian, and J.W. Pollard. Immune cell promotion of metastasis. *Nature Reviews Immunology*, 15:73–86, 2015. doi:10.1038/nri3789.
- [88] H. Knutsdottir, J.S. Condeelis, and E. Palsson. 3-d individual cell based computational modeling of tumor cell-macrophage paracrine signaling mediated by egf and csf-1 gradients. *Integrative Biology*, 8(104), 2016. doi:10.1039/c5ib00201j.

- [89] G.S. Kumar and B.S. Manjunatha. Metastatic tumors to the jaws and oral cavity. *Journal of Oral and Maxillofacial Pathology*, 17(1):71–75, 2013.
- [90] V. Kuznetsov and G. Knott. Modeling tumor regrowth and immunotherapy. *Mathematical and Computer Modelling*, 33(12-13):1275–1287, 2001. doi: 10.1016/S0895-7177(00)00314-9.
- [91] V. Kuznetsov, V. Makalkin, I. Taylor, et al. Nonlinear dynamics of immunogenic tumors: Parameter estimation and global bifurcation analysis. *Bulletin of Mathematical Biology*, 50(2):295–321, 1994.
- [92] S.D. Lawley, J.C. Mattingly, and M.C. Reed. Sensitivity to switching rates in stochastically switched odes. *Communications in Mathematical Sciences*, 12(7):1343–1352, 2014.
- [93] L.A. Liotta and C. DeLisi. Method for quantitating tumor cell removal and tumor cell-invasive capacity in experimental metastases. *Cancer Research*, 37:4003–4006, 1977.
- [94] L.A. Liotta, C. Delisi, G. Saidel, and J. Kleinerman. Micrometastasis formation: A probabilistic model. *Cancer Letters*, 3:203–208, 1977.
- [95] L.A. Liotta, G.M. Saidel, and J. Kleinerman. Stochastic model of metastases formation. *Biometrics*, 32(3):535–550, 1976.
- [96] Y. Liu and X. Cao. Immunosuppressive cells in tumor immune escape and metastasis. *Journal of Molecular Medicine*, 94(5):509–522, 2016. doi:10.1007/s00109-015-1376-x.
- [97] K.J. Luzzi et al. Multistep nature of metastatic inefficiency: Dormancy of solitary cells after successful extravasation and limited survival of early micrometastases. *American Journal of Pathology*, 153(865), 1998. DOI: 10.1016/S0002-9440(10)65628-3.
- [98] J. Marx. Inflammation and cancer: The link grows stronger. *Science*, 306(5698):966–968, 2004.
- [99] H.P. McKean. Application of Brownian Motion to the equation of Kolmogorov-Petrovskii-Piskunov. *Communications on Pure and Applied Mathematics*, 28(3):323–331, 1975.
- [100] P. Mehlen and A. Puisieux. Metastasis: A question of life or death. *Nature Reviews Cancer*, 6(6):449–458, 2006.

- [101] X. Meng, J. Zhong, S. Liu, et al. A new hypothesis for the cancer mechanism. *Cancer and Metastasis Reviews*, 31(1):247–268, 2012. doi:10.1007/s10555-011-9342-8.
- [102] L.M. Merlo, J.W. Pepper, B.J. Reid, et al. Cancer as an evolutionary and ecological process. *Nature Reviews Cancer*, 6:924–935, 2006.
- [103] F. Michor and Y. Iwasa. Dynamics of metastasis suppressor gene inactivation. *Journal of Theoretical Biology*, 241(3):676–689, 2006.
- [104] F. Michor, M. Nowak, and Y. Iwasa. Stochastic dynamics of metastasis formation. *Journal of Theoretical Biology*, 240(4):521–530, 2006.
- [105] A. Muller, B. Homey, H. Soto, et al. Involvement of chemokine receptors in breast cancer metastasis. *Nature*, 410(6824):50–56, 2001.
- [106] R.P. Negus, G.W. Stamp, J. Hadley, et al. Quantitative assessment of the leukocyte infiltrate in ovarian cancer and its relationship to the expression of c-c chemokines. *American Journal of Pathology*, 150(5):1723–1734, 1997.
- [107] K. Oleinika, R.J. Nibbs, G.J. Graham, et al. Suppression, subversion and escape: The role of regulatory t cells in cancer progression. *Clinical and Experimental Immunology*, 171(1):36–45, 2013.
- [108] O. Olobatuyi, G. de Vries, and T. Hillen. A reaction-diffusion model for radiation-induced bystander effects. *Journal of Mathematical Biology*, 75(2):341–372, 2017.
- [109] P.A. Orlando, R.A. Gatenby, and J.S. Brown. Tumor evolution in space: the effects of competition colonization tradeoffs on tumor invasion dynamics. *Frontiers in Oncology*, 3(45), 2013. doi:10.3389/fonc.2013.00045.
- [110] S. Paget. The distribution of secondary growths in cancer of the breast. 1889. *Cancer Metastasis Review*, 8(2):98–101, 1989.
- [111] K.J. Painter, N.J. Armstrong, and J.A. Sherratt. The impact of adhesion on cellular invasion in cancer and development. *Journal of Theoretical Biology*, 264(3):1057–67, 2012. doi:10.1016/j.jtbi.2010.03.033.
- [112] C.G. Park, C.A. Hartl, D. Schmid, et al. Extended release of perioperative immunotherapy prevents tumor recurrence and eliminates metastases. *Science Translational Medicine*, 10(433):eaar1916, 2018.

- [113] M. Pascual, S. Alonso, D. Pares, et al. Randomized clinical trial comparing inflammatory and angiogenic response after open versus laparoscopic curative resection for colonic cancer. *British Journal of Surgery*, 98:50–59, 2010.
- [114] J. Poleszczuk and H. Enderling. Cancer stem cell plasticity as tumor growth promoter and catalyst of population collapse. *Stem Cells International*, 2015. Article ID: 713565.
- [115] J. Poleszczuk, K. Luddy, S. Prokopiou, et al. Abscopal benefits of localized radiotherapy depend on activated t-cell trafficking and distribution between metastatic lesions. *Cancer Research*, 76(5):1009–1018, 2016. doi: 10.1158/0008-5472.CAN-15-1423.
- [116] J. Poleszczuk, E.G. Moros, M. Fishman, et al. Modeling T-cell trafficking to increase the likelihood of radiation-induced abscopal effects. *Journal of Targeted Therapies in Cancer*, 06.17:36–40, 2017.
- [117] B.Z. Qian and J.W. Pollard. Macrophage diversity enhances tumor progression and metastasis. *Cell*, 141(1):39–51, 2010. doi:10.1016/j.cell.2010.03.014.
- [118] A. Rhodes and T. Hillen. Mathematical modeling of the role of survivin on dedifferentiation and radioresistance in cancer. *Bulletin of Mathematical Biology*, 78(6):1162–1188, 2016.
- [119] N. Riggi, M. Auget, and I. Stamenkovic. Cancer metastasis: A reappraisal of its underlying mechanisms and their relevance to treatment. *Annual Review of Pathology: Mechanisms of Disease*, 13:117–140, 2018.
- [120] M. Robertson-Tessi, R.J. Gillies, R.A. Gatenby, and A.R.A. Anderson. Impact of metabolic heterogeneity on tumor growth, invasion, and treatment outcomes. *Cancer Res.*, 75(8):1567–1579, 2015. doi:10.1158/0008-5472.CAN-14-1428.
- [121] G.M. Sidel, L.A. Liotta, and J. Kleinerman. System of dynamics of a metastatic process from an implanted tumor. *Journal of Theoretical Biology*, 56:417–434, 1976.
- [122] M. Scalerandi, A. Romano, G.P. Pescarmona, et al. Nutrient competition as a determinant for cancer growth. *Physical Review E*, 59(2):2206–2217, 1999.

- [123] J.G. Scott, P. Gerlee, D. Basanta, A.G. Fletcher, P.K. Maini, and A.R. Anderson. *Chapter 9: Mathematical Modeling of the Metastatic Process*. Springer, 2013.
- [124] L. Shahriyari. A new hypothesis: some metastases are the result of inflammatory processes by adapted cells, especially adapted immune cells at sites of inflammation. *F1000 Research*, 5(175), 2016. doi:10.12388/f1000research.8055.1.
- [125] A.S. Silva, J.A. Yunes, R.J. Gillies, et al. The potential role of systemic buffers in reducing intratumoral extracellular pH and acid-mediated invasion. *Cancer Research*, 69(6):2677–2684, 2009.
- [126] W.F. Sindelar et al. Electron microscopic observations on formation of pulmonary metastases. *Journal of Surgical Research*, 18(2):137–161, 1975.
- [127] J. Sing, F. Hussain, and P. Decuzzi. Role of differential adhesion in cell cluster evolution: from vasculogenesis to cancer metastasis. *Compt Methods Biomech Biomed Engin.*, 18(3):282–292, 2015. doi:10.1080/10255842.2013.792917.
- [128] H. Siu, E.S. Vitetta, R.D. May, et al. Tumor dormancy. i. regression of bcl₁ tumor and induction of a dormant tumor state in mice chimeric at the major histocompatibility complex. *Journal of Immunology*, 137:1376–1382, 1986.
- [129] A. Sottoriva, P.M.A. Slood, J.P. Medema, et al. Exploring cancer stem cell niche directed tumor growth. *Cell Cycle*, 9(8):1472–1479, 2010.
- [130] C. Steidl, T. Lee, S.P. Shah, et al. Tumor-associated macrophages and survival in classic hodgkin’s lymphoma. *New England Journal of Medicine*, 365:875–885, 2010.
- [131] D. Tarin, J.E. Price, M.G. Kettlewell, et al. Mechanisms of human tumor metastasis studied in patients with peritoneovenous shunts. *Cancer Research*, 44(8):3584–3592, 1984.
- [132] A. Uppal, S.C. Wightman, S. Ganai, et al. Investigation of the essential role of platelet-tumor cell interactions in metastasis progression using an agent-based model. *Theoretical Biology and Medical Modelling*, 11(17), 2014. doi:10.1186/1742-4682-11-17.

- [133] S. Valastyan and R.A. Weinberg. Tumor metastasis: Molecular insights and evolving paradigms. *Cell*, 147(2):275–292, 2011. doi: 10.1016/j.cell.2011.09.024.
- [134] R. Walker, J. Poleszczuk, S. Pilon-Thomas, et al. Immune interconnectivity of anatomically distant tumors as a potential mediator of systemic responses to local therapy. *Scientific Reports*, 8(9474), 2018.
- [135] R. Walker, J.D. Schoenfeld, S. Pilon-Thomas, et al. Evaluating the potential for maximized t cell redistribution entropy to improve absopal responses to radiotherapy. *Convergent Science Physical Oncology*, 3(034001), 2017.
- [136] N.D. Walter, P.L. Rice, E.F. Redente, et al. Wound healing after trauma may predispose to lung cancer metastasis: Review of potential mechanisms. *American Journal of Respiratory Cell and Molecular Biology*, 44(5):591–596, 2011. doi: 10.1165/rcmb.2010-0187RT.
- [137] L. Weiss. Metastatic inefficiency. *Advances in Cancer Research*, 54:159–211, 1990.
- [138] K. Wilkie and P. Hahnfeldt. Modeling the dichotomy of the immune response to cancer: Cytotoxic effects and tumor-promoting inflammation. *Bulletin of Mathematical Biology*, 79(6):1426–1448, 2017.
- [139] Y. Ye, S. Liu, C. Wu, et al. TGF β modulates inflammatory cytokines and growth factors to create premetastatic microenvironment and stimulate lung metastasis. *Journal of Molecular Histology*, 46:365–375, 2015.